

STIS spectroscopy of the emission line gas in the nuclei of nearby FR-I galaxies¹

Jacob Noel-Storr^{2,3}, Stefi A. Baum³, Gijs Verdoes Kleijn⁴, Roeland P. van der Marel³, Christopher P. O'Dea³, P. Tim de Zeeuw⁵, and C. Marcella Carollo⁶

ABSTRACT

We present the results of the analysis of a set of medium resolution spectra, obtained by the Space Telescope Imaging Spectrograph on board the *Hubble Space Telescope*, of the emission line gas present in the nuclei of a complete sample of 21 nearby, early-type galaxies with radio jets (the UGC FR-I Sample). For each galaxy nucleus we present spectroscopic data in the region of H α and the derived kinematics.

We find that in 67% of the nuclei the gas appears to be rotating and, with one exception, the cases where rotation is not seen are either face on or have complex central morphologies. We find that in 62% of the nuclei the fit to the central spectrum is improved by the inclusion of a broad component. The broad components have a mean velocity dispersion of 1349 ± 345 km s $^{-1}$ and are redshifted from the narrow line components (assuming an origin in H α) by 486 ± 443 km s $^{-1}$.

Subject headings: galaxies: active — galaxies: elliptical and lenticular — galaxies: individual (NGC 193, NGC 315, NGC 383, NGC 541, NGC 741, UGC 1841, NGC 2329, NGC 2892, NGC 3801, NGC 3862, UGC 7115, NGC 4261, NGC 4335, M84, M87, NGC 5127, NGC 5141, NGC 5490, NGC 7052, UGC 12064, NGC 7626) — galaxies: kinematics and dynamics — galaxies: nuclei

¹Based on observations with the NASA/ESA *Hubble Space Telescope*, obtained at the Space Telescope Science Institute, which is operated by the Association of Universities for Research in Astronomy, Inc., under NASA contract NAS 5-26555

²Columbia University, Astronomy Department, New York, NY 10027 jake@astro.columbia.edu

³Space Telescope Science Institute, 3700 San Martin Drive, Baltimore, MD 21218

⁴European Southern Observatory, Karl-Schwarzschild Str. 2, D-85748 Garching, Germany

⁵Sterrewacht Leiden, Postbus 9513, 2300 RA Leiden, The Netherlands

⁶Institute of Astronomy, ETH Zentrum, CH-8092 Zurich, Switzerland

1. Introduction

A nearby radio galaxy can produce a radio jet that reaches up to ~ 1 Mpc, emerging from a central engine that resides in an active region $\sim 10^{-3}$ pc in radius in its nucleus. The energy that powers radio jets and active nuclei is typically believed to be produced by the accretion of material onto a central supermassive black hole (Rees 1984). Central emission line gas is detected in virtually all nearby radio galaxies that harbor kiloparsec-scale radio jets, and this gas along with nuclear dust presumably provide sources of fuel for the central black hole. However, the relationship between normal early-type galaxies and early-type galaxies that are radio-loud remains one of the mysteries in active galaxy research.

Current evidence suggests that all galaxies may have central black holes and that the size of the black hole is a strong function of the mass of the bulge (for example, Kormendy & Richstone 1995) and even stronger function of the central stellar velocity dispersion (Ferrarese & Merritt 2000; Gebhardt, et al. 2000; Merritt & Ferrarese 2001; Tremaine, et al. 2002). It is not clear what drives these relationships or whether they are the same for active and quiescent galaxies. Since black hole growth and nuclear activity are causally related, scatter in these relationship can, in principle, put limits on the frequency and duration of nuclear activity in galaxies.

Typical findings are that 60% of quiescent early-type galaxies have detections of emission line gas (e.g. Philips, et al. 1986; Goudfrooij, et al. 1994) and about 40% have nuclear dust (e.g. van Dokkum & Franx 1995; Tran, et al. 2001). Despite the apparent presence of fuel, these galaxies fail to produce radio jets or any significant nuclear activity.

Nearby early-type galaxies with radio jets provide an opportunity to gain an understanding of the conditions in a galaxy which lead to the formation of a radio-active nucleus and of the physics of the regions which harbor the black hole and jet formation regimes. To this end, we are undertaking a coordinated, multiwavelength, study of a complete sample of the nearest radio galaxies (see §2).

Based on our imaging with the *Hubble Space Telescope* (HST) Wide Field and Planetary Camera - 2 (WFPC2) we found that the galaxies of our sample show ubiquitous nuclear dust and emission line gas (Verdoes Kleijn, et al. 1999). An understanding of the gas kinematics in the central region can enable us to determine the black hole masses (Harms, et al. 1994; Ferrarese, Ford, & Jaffe 1996; Machetto, et al. 1997; van der Marel & van den Bosch 1998; Ferrarese & Ford 1999; Verdoes Kleijn, et al. 2000; Sarzi, et al. 2001; Barth, et al. 2001) and the ionization mechanisms at work in the nuclear regions (e.g. Dopita, et al. 1997) and relate these to other properties of the activity and of the galaxy as a whole. In order to achieve this goal we have obtained HST Space Telescope Imaging Spectrograph (STIS) medium

resolution long slit spectra of the nuclear regions of our sample galaxies. We present those data here. In future work we will go on to model the kinematics and other properties of the emission line gas.

The paper is organized as follows. In section 2 we describe the sample and in section 3 we describe the STIS spectroscopic observations and the data reduction. In section 4 we describe our analysis procedures. We present our initial interpretations in section 5 and draw conclusions in section 6. We use a Hubble constant of $H_0 = 50 \text{ km s}^{-1} \text{ Mpc}^{-1}$ throughout.

2. Sample selection and Properties

Our galaxy sample (the UGC FR-I sample) contains all 21 nearby ($v_r < 7000 \text{ km s}^{-1}$), elliptical or S0 galaxies in the declination range $-5^\circ < \delta < 70^\circ$ in the UGC catalog (Nilson 1973, limits magnitude $m_B < 14^m6$ and angular size $\theta_p > 1'0$) that are extended radio-loud sources (larger than $10''$ at 3σ on VLA A-Array maps and brighter than 150 mJy from single dish flux density measurements at 1400 MHz)⁷. The source information is shown in Table 1.

This complete sample was drawn from a catalog of 176 radio-loud galaxies constructed by Condon & Broderick (1988), by position coincidence of radio identifications in the Green Bank 1400 MHz sky maps and galaxies in the UGC catalog.

All of the galaxies fall into the Fanaroff & Riley (1974) Type-I (FR-I) radio classification (see Xu, et al. 2000, for a description of the radio properties of our sample); i.e. they are low luminosity radio galaxies, with jets that are brightest nearest to the nucleus. (In contrast, FR-II galaxies are more powerful radio sources, and have bright spots at the far edges of their radio lobes.)

The primary energy source of each galaxy in the sample falls into ‘monster’ rather than ‘starburst’ classification of Condon & Broderick (1988) based on their infra-red to radio flux ratios (for example, see Heckman, et al. 1983)

$$u \equiv \log \left(\frac{S_{60\mu\text{m}}}{S_{1400\text{MHz}}} \right) \ll 1.6, \quad (1)$$

and infra-red spectral gradients

⁷We have slightly adjusted the sample definition since our earlier work, however the galaxies that the sample contains remain the same. The sample is complete within the definition given here as of the time of writing according to up to date data drawn from the NED database.

$$\alpha_{\text{IR}} \equiv \frac{\log (S_{60\mu\text{m}}/S_{25\mu\text{m}})}{\log (60/25)} < +1.25. \quad (2)$$

A photometric analysis of the nuclei of these galaxies was performed by Verdoes Kleijn, et al. (1999), based on observations made using the WFPC2 instrument (using the F555W and F814W filters) on board the HST (the photometric analyses of UGC 7115 and UGC 12064 are presented in Appendix A of Verdoes Kleijn, et al. 2002).

3. STIS Observations

In program 8236 we used HST/STIS (see Kimble, et al. 1998) to take spectra of the 19 sample members not previously or concurrently observed by others. Observations were carried out at both medium (for 19/19 galaxies) and low (for 4/19 galaxies) resolution, with the G750M and the G430L and G750L gratings respectively. Our medium resolution observation log is shown in Table 2. We will present the low resolution spectra in a future paper. We include in our analysis similar medium resolution data obtained by R. Green and collaborators for the nucleus of M84 (program 7124, see Bower, et al. 1998) and H. Ford and collaborators for the nucleus of M87 (program 8666) to complete the data set for UGC FR-I galaxies.

In our program, we observed each galaxy in three parallel, adjacent slit positions. For each slit position we obtained two exposures with a shift of 0''.202800 (4 unbinned STIS Pixels) along the slit direction to enable us to more efficiently remove detector effects (bad pixels, etc.). In the case of UGC 7115 we observed in only one slit position - we sacrificed STIS observing time to make WFPC2 observations of this galaxy as it had not been included in our earlier WFPC2 program.

The data for M87 (NGC 4486) were obtained in a similar manner to our own. In the case of M84 (NGC 4374) the observation pairs were not shifted along the slit direction, thus some detector effects may remain, though will be much less significant thanks to the far greater signal to noise.

We list the instrumental properties of the STIS configurations used in Table 3. Panel (a) of Figures 2 to 22 (see key in Figure 1) shows the location of the STIS slits on each galaxy observed, along with the position angles of the galaxy major axes and radio-jet axes. For the majority of cases the STIS slits were aligned within 10° of the galaxy major axes (Table 4), with the exceptions that we note below.

In the cases of NGC 741 [$\Delta PA(\text{galaxy}, \text{STIS}) = 19.4^\circ$] and NGC 2892 [$\Delta PA(\text{galaxy}, \text{STIS}) =$

22°] more freedom in orientation was allowed to provide reasonable observing windows.

In NGC 3862 and UGC 7115 the position angles of the galaxy major axes are hard to determine, we decided to position the slits approximately perpendicular to the radio jets [$\Delta PA(radio, STIS) = 92.3^\circ \& 110.4^\circ$, respectively]. The central major axis is also hard to determine in NGC 541, where the central isophotes rotate considerably. In this case we chose to use a slit position somewhere around the mean of the isophotal position angles with considerable leeway given to allow for reasonable observing windows.

For UGC 12064 the slits were aligned along the major axis of the prominent dust disk, which is offset from the galaxy major axis by $\sim 50^\circ$.

The slits in M84 were positioned approximately perpendicular to the radio jet, which lies close to the major axis of the nuclear gas. For NGC 4486 (M87) the slits were positioned to follow certain morphological structures across the nuclear regions.

3.1. Data Reduction

We used the standard STIS calibration pipeline (`calstis`, see Brown, et al. 2002) to perform bias, dark and flat-field corrections using the best available reference files. We used `calstis` version 2.13 (26-April-2002) throughout the data reduction⁸.

We shifted the rows of alternating observations by 4 pixels, so that they were properly aligned with their counterparts and combined them using the STSDAS routine `ocrreject`. We cleaned co-incident cosmic rays and negative bad pixels, which would not be caught by `ocrreject`, using the NOAO/IRAF task `cosmicrays`. At each step we carefully investigated the effects of varying task parameters to insure we were not damaging valid data while removing most cosmic rays.

We made use of the STIS calibration pipeline tasks `wavecal` and `x2d` to perform wavelength calibration and image rectification respectively. The error introduced by rectifying after shifting one of the images is $\lesssim 0.05$ pixels (which is $\lesssim 1.3$ km s⁻¹ at 6750Å).

Panel (b) of Figures 2 to 22 (see key in Figure 1) shows (i) the central strip of the reduced spectrum for each slit position observed on each galaxy, along with (ii) Gaussian line fits to the same (see §4.1).

⁸We found that significant variations in measured parameters could be introduced by using different `calstis` versions. Versions 2.4 and 2.13 produce consistent results, while intermediate versions do not.

4. Analysis

In this section we describe the line fitting that we carried out on each spectral row of each reduced CCD spectral image, firstly with a single Gaussian per spectral line (§4.1) and secondly with the inclusion of an additional free component (§4.2). In §4.3 we discuss the sizes of the errors on quoted parameters from various sources. In §4.4 we describe each of the UGC FR-I sample members in turn. For each galaxy we define the central spectrum as the row with the greatest integrated flux after the data reduction. We list the row numbers in the final `x2d` image corresponding to the central spectrum in Table 2.

4.1. Single Gaussian line fitting

In the G750M spectra we expect to find the emission lines in the vicinity of H α that are listed in Table 5. We used wavelengths from the recent measurements of Wallerstein, et al. (2001) and converted from air to vacuum wavelengths using the IAU standard formula

$$\frac{\lambda_{\text{vac}} - \lambda_{\text{air}}}{\lambda_{\text{air}}} = 6.4328 \times 10^{-5} + \frac{2.94981 \times 10^{-2}}{146 - (10^4/\lambda_{\text{air}})^2} + \frac{2.5540 \times 10^{-4}}{41 - (10^4/\lambda_{\text{air}})^2}. \quad (3)$$

Using one Gaussian to represent each of these five lines we obtain a set of 7 free parameters to fit: the continuum flux level, velocity (v_r), velocity dispersion (σ), and the fluxes of each line. The flux of [N II]₆₅₅₀ was fixed in a ratio of 1:3 with the flux of [N II]₆₅₈₅ based on the transition probabilities derived from atomic physics (Osterbrock 1989).

We used a χ^2 minimization routine (using Levenberg-Marquardt iterations, see Press, et al. 1992) to fit the Gaussian template to the observed spectra. The application of this fitting technique and development of this routine are described by van der Marel & van den Bosch (1998). Formal errors are drawn from the covariance matrix of the fit. As we do not expect the noise in each spectrum to be normally-distributed after the steps of wavelength calibration and two-dimensional rectification, these error values should be treated strictly as the formal fit errors under the understanding that the size of the real errors may be somewhat different (see §4.3 below).

From this point on we only consider data points where the formal errors from the fits meet the following criteria, allowing us to exclude unreliable data points originating from poorly constrained fits:

$$\Delta\sigma < 50 \text{ km s}^{-1} \quad (4)$$

$$\frac{\Delta F(H\alpha)}{F(H\alpha)} < 0.75 \quad (5)$$

where $\Delta\sigma$ and $\Delta F(H\alpha)$ are the errors in velocity dispersion and line flux respectively. The main constraint arises from the limit on the velocity dispersion error. The very large flux error allowed is in place to remove only the few remaining bad data points where the profile very precisely fits the noise.

In Panel (e) of Figures 2 to 22 (see key in Figure 1) we show profiles of (i) radial velocity, (ii) velocity dispersion, (iii) $[N\text{ II}]_{6585}$ line flux and (iv) $[N\text{ II}] / H\alpha$ ratios resulting from this fitting procedure for each of our sample galaxies. These profiles are combined and visualized in 2D for each galaxy in Panel (c) of Figures 2 to 22.

We present the fit data in Tables 6 to 26, where the errors given are the formal errors from the fit. In these tables Column (1) is the row number of the portion of the spectrum fitted. Column (2) shows the offset along the slit direction in arcseconds from the row with the greatest integrated flux. Columns (3) and (4) give the radial velocities (v_r) and gas velocity dispersions (σ_{gas}) respectively. Column (5) gives the line flux of the $H\alpha$ line and columns (6) and (7) show its ratio against the fluxes of the $[N\text{ II}]_{6585}$ and $[S\text{ II}]_{total}$ (the total flux of the two $[S\text{ II}]$ lines) respectively. Column (8) gives the reduced χ^2 (R^2) value of the resulting fit.

We repeated the fit for the central row of the galaxy NGC 4335 varying the set of free parameters in order to estimate the reliability of the fits that we had used. We found that the fit was stable to within one formal error on all quoted parameters when the velocities, velocity dispersions and fluxes of all parameters were fit independently. The signal to noise falls off rapidly outside of the very nuclear regions so it is not possible to consistently run fits with a large number of free parameters. The results for the nucleus of NGC 4335 satisfy us that we are justified in fixing the parameters in the manner that we have chosen, without adding any obvious biases to our results.

4.2. Fits with an additional free component

In many cases, as the very central pixels are reached the fit begins to do a poorer job of matching the observed profile. In an attempt to improve the fit to the narrow centers of the lines we tested a fit for the central spectrum of each galaxy including an additional fit component with independent velocity, velocity dispersion and flux, along with the original set of five Gaussians. The fits to the central spectra are shown in Panel (d) of Figures 2 to 22 (see key in Figure 1), (i) excluding and (ii) including the additional component.

We assessed the effectiveness of including this component in each galaxy based on (1) an improvement in the mean of the absolute value of the residuals from the fit $\geq 5\%$ (2) an improvement in the reduced χ^2 value of the fit such that $(R_1^2 - R_2^2)/R_1^2 \geq 0.15$ and (3) an improvement judged by eye in the fit compared to the data. We assigned a score to each galaxy, with one point available for each of the three categories. We consider scores of 2 or 3 to be indicative of the presence of a broad component, a score of 1 indicates the possibility of a broad component, while we treat a score of 0 as a none detection. The three parameters and scores are listed in Table 28.

We find an additional free component improves the fit in 62% ($N = 13$) of the sample galaxies. In the cases of NGC 2329 and NGC 3862 the component appears to represent a non-flat continuum. The kinematic parameters for each galaxy including the additional free component are listed in Table 29 and the flux parameters in Table 30. We present further interpretation of the nature and origin of the features fit by the additional free component in §5.3.

4.3. Quantifying error sources

The STIS data handbook (Brown, et al. 2002) gives the following absolute and relative accuracies applicable to this work: A wavelength absolute calibration error ($\Delta\lambda$ offset) of 0.1 to 0.3 pixels (2.6 to 7.7 km s $^{-1}$ at 6500Å) within an exposure, and from 0.2 to 0.5 pixels (5.1 to 12.8 km s $^{-1}$ at 6500Å) between exposures. An absolute photometry error of 5% and a relative photometry error of 2% within a single exposure assuming a wide slit observation. 5 μ m variations in slit width along the slit lengths could result in variations of up to 20% in flux along the 0''.1 slit.

In Verdoes Kleijn, et al. (2002) H α + [N II] fluxes were presented for each nucleus in the sample. The values presented there agree well with the values we find here, certainly given our limited ability to extract comparable apertures and within the 20% potential flux errors noted above.

In Section 1 we indicated that a 1.3 km s $^{-1}$ error could be incorporated into the final data as a result of shifting the spectra for image combination and cosmic ray rejection. This shift is insignificant compared to other error sources.

In Table 27 we showed that by allowing different free parameters within the single-Gaussian-per-line fit produced changes in the measurement in velocity of ~ 8 km s $^{-1}$ and of ~ 16 km s $^{-1}$ in velocity dispersion for the nucleus of NGC 4335.

In Table 33 we show the effect on the measured velocities and velocity dispersions of the various components for each of the models described in the previous section, again for the case of NGC 4335. This illustrates that the measured velocities of the narrow lines may vary by up to $\sim 20 \text{ km s}^{-1}$ (and velocity dispersions by as much as $\sim 110 \text{ km s}^{-1}$) when additional components in the line shape are taken into account.

In the nuclei of NGC 383 and NGC 4335 (representing cases with blended and less blended lines respectively) we repeated the narrow line fit to the central spectrum with 286 different combinations of input velocity and velocity dispersion; varying the velocities over a range of 2000 km s^{-1} and the velocity dispersions over a range of 6000 km s^{-1} . In the case of NGC 4335 we found that the velocity varied by $\pm 10.91 \text{ km s}^{-1}$ and the velocity dispersion by just $\pm 0.02 \text{ km s}^{-1}$. In the case of NGC 383 we found that the velocity varied by $\pm 13.04 \text{ km s}^{-1}$ and the velocity dispersion by just $\pm 3.76 \text{ km s}^{-1}$. There was a systematic effect relating input and output velocities in both cases.

We conclude that reasonable estimates of the genuine errors on each of our measured parameters are: 5% - 10% on fluxes (dominated by the effects of variations along the narrow slits and the STIS absolute calibration); and $\sim 20 \text{ km s}^{-1}$ on velocities and velocity dispersions (dominated by the fit model dependency of the results).

4.4. Individual source descriptions

Below, we give descriptions of each member of the UGC FR-I sample in turn. The galaxy classifications are taken from the NASA Extragalactic Database, which lists references in which the terms used are described. Descriptions of dust properties and radio sources are as presented by Verdoes Kleijn, et al. (1999) and Xu, et al. (2000) respectively.

NGC 193 (UGC 408) This S0 galaxy has a complex gas morphology with two lanes apparent in the central regions (the most clearly defined lane has a $width : length = 0.18$). It has a core-jet radio morphology on VLA and VLBA scales. The STIS slits were aligned parallel to the galaxy major axis. The central kinematic and flux properties are listed in Table 6; the gas does not exhibit a regular rotation curve, though it does appear dominated by systematic rather than random motions. The fit to the central spectrum is improved by the addition of a broad component. Data for this galaxy are shown in Figure 2 (see key in Figure 1 for an explanation of these plots).

NGC 315 (UGC 597) This elliptical galaxy has a nuclear dust disk ($b/a = 0.23$). It has a core-jet radio morphology on VLA and VLBA scales. The STIS slits were aligned parallel to the galaxy major axis. The central kinematic and flux properties are listed in Table 7; the gas appears to be in organized motion, possibly regular rotation. The fit to the central spectrum is improved by the addition of a broad component. Data for this galaxy are shown in Figure 3 (see key in Figure 1 for an explanation of these plots).

NGC 383 (UGC 689) This S0 galaxy has a nuclear dust disk ($b/a = 0.77$). It has a core-jet radio morphology on VLBA scales, and a twin-jet morphology on VLA scales. The STIS slits were aligned parallel to the galaxy major axis. The central kinematic and flux properties are listed in Table 8; the gas exhibits a regular rotation profile. In the negative offset side slit there is a dip in the velocity dispersion profile at a position close to the nucleus. The fit to the central spectrum is improved by the addition of a broad component. Data for this galaxy are shown in Figure 4 (see key in Figure 1 for an explanation of these plots).

NGC 541 (UGC 1004) This cD S0 galaxy has a nuclear dust disk ($b/a = 0.91$). It has a radio core on VLBA scales and a core-jet morphology on VLA scales. The STIS slits were aligned to a mean of the position angles of the central isophotes measured from our WFPC/2 images, which vary considerably. We allowed considerable flexibility in position angle to enable reasonable observing windows. The central kinematic and flux properties are listed in Table 9; the gas does not exhibit a regular rotation profile. The fit to the central spectrum is not significantly improved by the addition of a broad component, though the fit improves somewhat when judged by eye. Data for this galaxy are shown in Figure 5 (see key in Figure 1 for an explanation of these plots).

NGC 741 (UGC 1413) This E0 galaxy has no apparent nuclear dust. It has a radio core on VLBA scales and a core-jet morphology on VLA scales. The STIS slits were aligned approximately parallel to the galaxy major axis, however a certain degree of freedom was allowed in slit placement to allow reasonable observing windows. The central kinematic and flux properties are listed in Table 10. Very few points had sufficient signal to noise to obtain good fits in these data, it has not been included in further analysis of global kinematic properties. The fit to the central spectrum is not improved by the addition of a broad component. Data for this galaxy are shown in Figure 6 (see key in Figure 1 for an explanation of these plots).

UGC 1841 This elliptical galaxy has a nuclear dust disk ($b/a \sim 0.98$). It has a core-jet radio morphology on VLBA and VLA scales. The STIS slits were aligned parallel to the galaxy major axis. The central kinematic and flux properties are listed in Table 11; the gas does not exhibit a regular rotation profile. The fit to the central spectrum is improved by the addition of a broad component. Data for this galaxy are shown in Figure 7 (see key in Figure 1 for an explanation of these plots).

NGC 2329 (UGC 3695) This S0 galaxy has a nuclear dust disk ($b/a = 0.68$). It has a core-jet radio morphology on VLBA and VLA scales. The STIS slits were aligned parallel to the galaxy major axis. The central kinematic and flux properties are listed in Table 12; the gas does not exhibit a regular rotation profile. The fit to the central spectrum is improved by the addition of a broad component which appears to represent a non-flat continuum in this case. Data for this galaxy are shown in Figure 8 (see key in Figure 1 for an explanation of these plots).

NGC 2892 (UGC 5073) This elliptical galaxy has no apparent nuclear dust. It has a radio core on VLBA scales and a twin-jet morphology on VLA scales. The STIS slits were aligned approximately parallel to the galaxy major axis, however a certain degree of freedom was allowed in slit placement to allow reasonable observing windows. The central kinematic and flux properties are listed in Table 13; the gas does not exhibit a regular rotation profile. The fit to the central spectrum is not significantly improved by the addition of a broad component. Data for this galaxy are shown in Figure 9 (see key in Figure 1 for an explanation of these plots).

NGC 3801 (UGC 6635) This S0/a galaxy has a complex nuclear dust morphology with a large scale dust lane ($width : length = 0.12$). It has a twin-jet radio morphology on VLA scales. The STIS slits were aligned parallel to the galaxy major axis. The central kinematic and flux properties are listed in Table 14; the gas does not exhibit a regular rotation profile. The fit to the central spectrum is not significantly improved by the addition of a broad component. Data for this galaxy are shown in Figure 10 (see key in Figure 1 for an explanation of these plots).

NGC 3862 (UGC 6723) This elliptical galaxy has a nuclear dust disk ($b/a \sim 0.99$). It has a core-jet radio morphology on VLBA and VLA scales. The STIS slits were aligned approximately perpendicular to the radio jet as the nuclear isophotal position angles are poorly constrained. The central kinematic and flux properties are listed in Table 15; the gas

does not exhibit a regular rotation profile. The fit to the central spectrum is improved by the addition of a broad component which appears to represent a non-flat continuum in this case. Data for this galaxy are shown in Figure 11 (see key in Figure 1 for an explanation of these plots).

UGC 7115 This elliptical galaxy has a nuclear dust disk ($b/a \sim 0.95$). It has a core-jet radio morphology on VLA scales. The STIS slit were aligned approximately perpendicular to the radio jet as the nuclear isophotal position angles are poorly constrained, a certain degree of freedom was allowed in slit placement to allow reasonable observing windows. This galaxy was observed in only one slit position, as we also required WFPC2 observations of this target in order to measure the central photometric properties (see Verdoes Kleijn, et al. 2002). The central kinematic and flux properties are listed in Table 16; the gas exhibits a regular rotation profile. The fit to the central spectrum is not significantly improved by the addition of a broad component. Data for this galaxy are shown in Figure 12 (see key in Figure 1 for an explanation of these plots).

NGC 4261 (UGC 7360) This E2-3 galaxy has a nuclear dust disk ($b/a = 0.46$). It has a twin-jet radio morphology on VLBA and VLA scales. The STIS slits were aligned parallel to the galaxy major axis. The central kinematic and flux properties are listed in Table 17. The nucleus of this galaxy lies closer to one of the side slits (slit one) than the central position, however it is still possible to see a clear rotation curve along that slit. The fit to the central spectrum is improved by the addition of a broad component. Data for this galaxy are shown in Figure 13 (see key in Figure 1 for an explanation of these plots).

NGC 4335 (UGC 7455) This elliptical galaxy has a nuclear dust disk ($b/a = 0.41$). It has a radio core on VLBA scales and a twin-jet morphology on VLA scales. The STIS slits were aligned parallel to the galaxy major axis. The central kinematic and flux properties are listed in Table 18; the gas exhibits a regular rotation profile. In the positive offset side slit there is a dip in the velocity dispersion profile at the position closest to the nucleus. See also Verdoes Kleijn, et al. (2002). The fit to the central spectrum is improved by the addition of a broad component. Data for this galaxy are shown in Figure 14 (see key in Figure 1 for an explanation of these plots).

NGC 4374 (M84; UGC 7494) This E1 galaxy has a nuclear dust lane ($width : length = 0.15$). It has a core-jet radio morphology on VLBA scales, and a twin-jet morphology on VLA scales. The STIS slits were aligned approximately perpendicular to the radio jets,

which lies close to the major axis of the emission line gas. The central kinematic and flux properties are listed in Table 19; the gas exhibits a regular rotation profile. See also Bower, et al. (1998). The fit to the central spectrum is not significantly improved by the addition of a broad component. Data for this galaxy are shown in Figure 15 (see key in Figure 1 for an explanation of these plots).

NGC 4486 (M87; UGC 7654) This elliptical galaxy has an irregular nuclear dust morphology. It has a core-jet radio morphology on VLBA and VLA scales. The STIS slits were aligned to trace morphological features in the emission line gas across the nuclear region of this galaxy. The central kinematic and flux properties are listed in Table 20; the gas exhibits a regular rotation profile. The fit to the central spectrum is improved by the addition of a broad component. Data for this galaxy are shown in Figure 16 (see key in Figure 1 for an explanation of these plots).

NGC 5127 (UGC 8419) This elliptical peculiar galaxy has a nuclear dust lane ($width : length = 0.25$). It has a radio core on VLBA scales and a twin-jet morphology on VLA scales. The STIS slits were aligned parallel to the galaxy major axis. The central kinematic and flux properties are listed in Table 21; the gas exhibits a regular rotation profile. The fit to the central spectrum is not significantly improved by the addition of a broad component. Data for this galaxy are shown in Figure 17 (see key in Figure 1 for an explanation of these plots).

NGC 5141 (UGC 8433) This S0 galaxy has a nuclear dust lane ($width : length = 0.25$). It has a core-jet radio morphology on VLBA scales and a twin-jet morphology on VLA scales. The STIS slits were aligned parallel to the galaxy major axis. The central kinematic and flux properties are listed in Table 22; the gas exhibits a regular rotation profile. The fit to the central spectrum is improved by the addition of a broad component. Data for this galaxy are shown in Figure 18 (see key in Figure 1 for an explanation of these plots).

NGC 5490 (UGC 9058) This elliptical galaxy has a nuclear dust lane ($width : length = 0.35$). It has a core-jet radio morphology on VLBA scales and a twin-jet morphology on VLA scales. The STIS slits were aligned parallel to the galaxy major axis. The central kinematic and flux properties are listed in Table 23; the gas does not exhibit a regular rotation profile. The fit to the central spectrum is improved by the addition of a broad component. Data for this galaxy are shown in Figure 19 (see key in Figure 1 for an explanation of these plots).

NGC 7052 (UGC 11718) This elliptical galaxy has a nuclear dust disk ($b/a = 0.30$). It has a twin-jet radio morphology on VLBA scales and a core-jet morphology on VLA scales. The STIS slits were aligned parallel to the galaxy major axis. The central kinematic and flux properties are listed in Table 24; the gas exhibits a regular rotation profile. The fit to the central spectrum is not significantly improved by the addition of a broad component. Data for this galaxy are shown in Figure 20 (see key in Figure 1 for an explanation of these plots).

UGC 12064 This S0 galaxy has a nuclear dust disk ($b/a = 0.54$). It has a twin-jet radio morphology on VLA scales. The STIS slits were aligned parallel to the dust disk major axis. The central kinematic and flux properties are listed in Table 25; the gas exhibits a regular rotation profile. The fit to the central spectrum is improved by the addition of a broad component. Data for this galaxy are shown in Figure 21 (see key in Figure 1 for an explanation of these plots).

NGC 7626 (UGC 12531) This elliptical peculiar galaxy has a nuclear dust lane ($width : length = 0.17$). It has a core-jet radio morphology on VLBA scales and a twin-jet morphology on VLA scales. The STIS slits were aligned parallel to the galaxy major axis. The central kinematic and flux properties are listed in Table 26; the gas exhibits a regular rotation profile. The fit to the central spectrum is improved by the addition of a broad component. Data for this galaxy are shown in Figure 22 (see key in Figure 1 for an explanation of these plots).

5. Interpretation and Discussion

In our initial interpretation we have focussed on understanding the general parameters of the data set. We will undertake more detailed analyses in future work that we outline in §6 below. Here, we first describe the categorization of sources as rotating and non-rotating systems based on the observed kinematics (§5.1). We then discuss the ionization states of the nuclear regions (§5.2). We go on to discuss the presence of broad components in these nuclei and a more detailed analysis of the line shapes (§5.3).

5.1. Rotators and non-rotators

By inspecting maps of the central kinematics and the velocity profiles along each slit (as presented above in figures 2 to 22), we have classified, by eye, the galaxies into two

classes: rotators and non-rotators. Rotators are systems where we see patterns reminiscent of rotation curves; in non-rotators we find no such patterns - the kinematics seem either irregular or organized in some manner that does not represent regular rotation. We do not include NGC 741 in discussions of kinematics as very few points were well fit during our analysis. We classify 67% ($N = 14/21$) of the UGC FR-I galaxies as rotators. 73% of galaxies with dust disks ($N = 8/11$), 100% of galaxies with dust lanes ($N = 5/5$) and 50% of galaxies with complex dust or no dust ($N = 2/4$) are rotators.

We have made use of the mean velocity dispersion

$$\overline{\sigma_{100\text{pc}}} = \frac{1}{N} \sum_i \sigma_i : x_i \leq 100\text{pc}, \quad (6)$$

and the difference in mean velocities on each side of the nucleus

$$\Delta_{100\text{pc}} = \left| \left(\frac{1}{N_1} \sum_i v_i : -100\text{pc} \leq x_i < 0 \right) - \left(\frac{1}{N_2} \sum_j v_j : 0 < x_j \leq 100\text{pc} \right) \right| \quad (7)$$

within 100 pc of the brightest pixel as illustrative of the global kinematic parameters along the central slit⁹. These parameters are shown in Table 31 for each galaxy, along with the mean properties for each class of galaxy. In Figure 23 we show the relationship between the two parameters for each galaxy. It is clear that the non-rotators lie at the bottom of the $\Delta_{100\text{pc}}$ distribution, so it is conceivable that irregular motions conceal any remaining signs of rotation in these cases. We note that we detect rotation in all cases where the disk is $\gtrsim 25^\circ$ from face on, other than those cases where the dust morphology is highly irregular. The only exception is NGC 5490 where the signal to noise was particularly poor.

In Figure 24 we show the values of $\Delta_{100\text{pc}}$ plotted as a function of dust disk axis ratio, or dust lane width to length ratio; if the dust were all in circular disks this would be an indicator of disk inclination. We included lines showing an indication of the projection of several values of $\Delta_{100\text{pc}}$ at different disk inclinations through the relation

$$\Delta_{obs} \approx \Delta_{int} \cdot \sin i \approx \Delta_{int} \times \sqrt{1 - \left(\frac{b}{a} \right)^2}, \quad (8)$$

⁹For NGC 4261 we used the offset slit closest to the nucleus as explained above.

Where Δ_{obs} is the observed Δ_{100pc} parameter at a given inclination, Δ_{int} is the presumed intrinsic rotation of the disk and b/a is the axis (or width:length) ratio. This is not a rigorously valid means of projecting these values, but it serves our purposes of illustration here.

It is easy to see that the non-rotators with face on disks would have to be intrinsically rotating very fast for their rotation to register over the random motions in these cases. From the observations of systems at greater inclinations we have no cause to expect any disks to be rotating that fast. In a similar manner we plot the values of $\overline{\sigma_{100pc}}$ against dust disk axis ratio, or dust lane width to length ratio in Figure 25. Here we see no clear trend in velocity dispersion with axis ratio.

We find no significant systematic differences between the typical values $\overline{\sigma_{100pc}}$ between the two classes. Using the Kolmogorov-Smirnov Test to assess the two groups we find a probability of 0.93 that the distributions of velocity dispersions were drawn from the same underlying distribution. Applying the same test to the Δ_{100pc} parameter gives only a 0.08 probability that these were drawn from the same distribution.

This evidence suggests to us that rotators and non-rotators represent the same type of kinematic systems, with observational effects such as inclination and dust properties limiting our ability to detect the rotation of those systems where we do not. We conclude that a model of a rotating gas disk with significant random motions is compatible with all of the observations.

5.2. Flux ratios and ionization

In Figure 26 we show the [N II] flux as a function of H α narrow line flux for each central spectrum. The values are compatible with values typically found for photo-ionization and shock models (see, for example, Dopita, et al. 1997). The unusually low ratios shown in two nuclei (NGC 383 and M84) are likely a consequence of the high degree of blending of the lines in these observations (see panel (d) of Figures 4 and 15), rather than any underlying physics.

While we are satisfied that our data have not produced any results that are incompatible with reasonable parameters, detailed modeling is required to understand the various ionization mechanisms at work in each individual case. We intend to undertake this type of modeling and present the outcomes in future work.

5.3. Are we observing broad lines?

The fit to the central spectrum is improved in 62% of the galaxies by the inclusion of an additional free Gaussian component (see §4.2). Each of these fits resulted in the supplementary component being centered redwards of the H α line with a velocity dispersion between about two and ten times that of the narrow lines; thus we describe this feature as a broad fit component. We identify these broad components in 73% of galaxies with dust disks ($N=8/11$), 60% of galaxies with dust lanes ($N=3/5$), 67% of galaxies with irregular dust ($N=2/3$) and 0% of galaxies with no dust ($N=0/2$).

If we make a flux cut in H α we find broad components in 40% of nuclei with $1 \times 10^{-15} \leq F(H\alpha) \leq 1 \times 10^{-14}$, in 55% of nuclei with $1 \times 10^{-14} \leq F(H\alpha) \leq 5 \times 10^{-14}$ and in 100% of nuclei with $F(H\alpha) \geq 5 \times 10^{-14}$. This detection trend with flux is reflected in Figure 26. This suggests that the detection of nuclear broad components is somewhat flux (and therefore signal to noise) dependent across the sample.

The broad components could originate either as an artifact of attempting to fit Gaussians to non-Gaussian line profiles, or from a physical source – such as a broad line region or a change in the characteristics of the gas as the inner regions of the disk are approached.

We detect broad components only in the central few pixels, this could be a consequence of either the fall in signal to noise or that the component is an unresolved source. It is important to note as a consequence of this, that fitting single Gaussians to each line samples a different part of the line shape as the central pixels are approached.

In Table 32 we show the mean properties of the broad components and compare them to the samples of LINERS by Ho, et al. (1997) and Radio Galaxies summarized by Sulentic, et al. (2000). These comparisons show that our broad components are compatible with the broad lines seen in LINERs and that the observed offsets from the narrow line components are compatible with those observed in samples of radio loud galaxies.

5.4. Constraining the line shapes

In order to better establish the line shape, we investigated the profiles from the nucleus of NGC 4335, which has a relatively good signal to noise and relatively non-blended lines (Verdoes Kleijn, et al. 2002).

We first investigated the profile of the two [S II] lines, as they are less entangled than the H α + [N II] complex. We fit these two lines with a varying number of Gaussians per line. The minimum in the reduced χ^2 parameter resulting from each of these fits lay between

two and three Gaussians per line. We extended the two Gaussian per line model to fit the entire profile of the five emission lines. By then testing various sets of free parameters we were able to discover an optimal set.

Fitting these models quickly illustrated that the additional broad component is a very strongly favored feature; in any case where it was possible for the parameters to contrive to create a broad component they did so. Table 33 shows the kinematic parameters and reduced χ^2 values from five combinations of fit parameters that produce distinct fits. These were:

1. *Narrow lines only*: The original 5 Gaussian model (one Gaussian for each of the following 5 lines: $[\text{N II}]_{6550}$, $\text{H}\alpha$, $[\text{N II}]_{6585}$, $[\text{S II}]_{6718}$, $[\text{S II}]_{6733}$), with a single value of velocity and velocity dispersion for all lines.
2. *Additional broad component*: The same as the *Narrow lines only* model, with an additional broad component, with an independent velocity, velocity dispersion and flux.
3. *Flux-constrained Broad Bases (i)*: The same as model 2, with an additional set of 5 Gaussians, representing the broader wings (Broad Bases). This new set of lines had a single velocity and velocity dispersion and the velocity was fixed to be the same as for the other lines. The fluxes of each line in the second set of Gaussians was fixed at a constant ratio to its counterpart in the first set, based on the mean ratio measured in the fit of two Gaussians per line to the two $[\text{S II}]$ lines as described above.
4. *Flux-constrained Broad Bases (ii)*: The same as model 3, however in this case the velocity of the set of broad bases was allowed to vary from that of the narrow lines.
5. *Flux-unconstrained Broad Bases*: the same as model 3, however in this case the lines in both sets were able to vary independently in flux, other than the fixed 1:3 ratio between the two $[\text{N II}]$ lines in each set.

We conclude, as the *Flux-constrained Broad Bases (ii)* model not only produces the most satisfying fit judged by eye, but also the lowest reduced χ^2 value, that this model is likely to most closely represent the line profile present in the central regions. The broad bases in this case are able to represent an asymmetric red wing on each line, but they do not reduce the importance of the broad component in the fit.

6. Conclusions

In this paper we presented the medium resolution spectra of the 21 galaxies in our UGC FR-I sample, obtained by ourselves and others using STIS. Data were obtained for three parallel slit positions on each nucleus (other than UGC 7115, which was observed in only one slit position).

We find that all nuclei are compatible with a single kinematic description: a rotating gas disk, where random motions are always important. We observe patterns reminiscent of rotation in 67% of the nuclei, in the remainder the non-detection can be accounted for as the systems are either face on, have complex central morphologies (as judged from the nuclear dust distribution) or, in the case of NGC 5490, particularly poor signal to noise.

We find that the inclusion of an additional fit component with unconstrained parameters improves our fit to the nuclear spectrum in 62% of the galaxies, where it fits in every case as a broad component in the vicinity of $H\alpha$ and [N II]. The detection of the broad component is related to the line flux (and therefore the signal to noise). The broad components have a mean velocity dispersion of 1349 ± 345 km s $^{-1}$ and are redshifted from the narrow line components (assuming an origin in $H\alpha$) by 486 ± 443 km s $^{-1}$.

The broad component could be a consequence of non-Gaussian line profiles with broad wings, which would be biased toward the brightest [N II] line (redwards of $H\alpha$). However, our more detailed analysis of line shape shows that it is very hard to reproduce this effect by including broad (even asymmetric) wings on each line, suggesting the broad component may indeed have a physical origin.

The measured $H\alpha$ to [N II] ratios for the narrow components in the central spectra are consistent with standard photo-ionization or shock-ionization models (for example, Dopita, et al. 1997) other than two examples where the lines are highly blended and may be leading us to misleading fits in the very center.

As we continue with this research we will next model the galaxies with thin disks and with spherical gas distributions (see, for example, Verdoes Kleijn, et al. 2002) in order to obtain estimates of the black hole masses for each galaxy in this complete sample. We will also extend our investigation into the ionization profiles of each nucleus; investigating the ionization properties of each nucleus and seeking the signs of jet / disk interactions.

The authors would like to thank Jacqueline van Gorkom for her very valuable comments on this work.

Support for this work was provided by NASA through grant number HST-GO-08236.01-

A from the Space Telescope Science Institute, which is operated by the Association of Universities for Research in Astronomy, Inc., under NASA contract NAS5-26555.

This research has made use of the NASA/IPAC Extragalactic Database (NED) which is operated by the Jet Propulsion Laboratory, California Institute of Technology, under contract with the National Aeronautics and Space Administration.

REFERENCES

- Barth, A. J., Sarzi, M. R., Rix, H.-W., Ho, L. C., Filippenko, A. V., & Sargent, W. L. W. 2001, ApJ, 555, 685
- Bower, G. A. et al. 1998, ApJ, 492, L111
- Brown, T. et al. 2002, in HST STIS Data Handbook, version 4.0, ed. B. Mobasher, Baltimore, STScI
- Condon, J. J., Broderick, J. J. 1988, AJ, 96, 30
- Davies, R. L., et al. 1987, ApJS, 64, 581
- Di Nella H., Garcia A.M., Garnier R., & Paturel G. 1995, A&AS, 113, 151
- Doptia, M. A., Koratkar, A. P., Allen, M. G., Tsvetanov, Z. I., Ford, H. C., Bicknell, G. V., & Sutherland, R. S. 1997, ApJ, 490, 202
- Fanaroff, B. L., & Riley, J. M. 1974, MNRAS, 167, 31P
- Ferrarese, L., Ford, H. C., & Jaffe, W. 1996, ApJ, 470, 444
- Ferrarese, L. C., & Ford, H. C. 1999, ApJ, 515, 583
- Ferrarese, L., & Merritt, D. 2000, ApJ, 539, 9
- Gebhardt, K., et al. 2000, ApJ, 539, 13
- Goudfrooij, P., Hansen, L., Jørgensen, H. E., & Nørgaard-Nielsen, H. U. 1994, A&AS, 105, 341
- Hardcastle, M. J., Alexander, P., Pooley, G. G., Riley, J. M. 1998, MNRAS, 296, 445
- Harms, R. J., et al. 1994, ApJ, 435, 35
- Heckman, T. M., Van Breugel, W., Miley, G. K., Butcher, H. R. 1983, AJ, 88, 1077

- Ho, L. C., Filippenko, A. V., Sargent, W. L. W., & Peng, C. Y. 1997, ApJS, 112, 391
- Jørgensen, I., Franx, M., & Kjærgaard, P. 1995, MNRAS, 276, 1341
- Kimble, R., et al. 1998, ApJ, 539, 13
- Kormendy, J., & Richstone, D. 1995, ARA&A, 33, 581
- Macchetto, F., et al. 1997, ApJ, 489, 579
- Maciejewski, W., Binney, J. 2001, MNRAS, 323, 831
- Merritt, D., & Ferrarese, L. 2001, ApJ, 547, 140
- Nilson, P. 1973, The Uppsala General Catalogue of Galaxies [UGC], (Uppsala: Astronomiska Observatorium)
- Osterbrock, D. E. 1989, Astrophysics of gaseous nebulae and active galactic nuclei, (Mill Valley, CA: University Science Books)
- Philips, M. M., Jenkins, C. R., Dopita, M. A., Sadler, E. M., & Binette, L. 1986, AJ, 91, 1062
- Press, W. H., Teukolsky, S. A., Vetterling, W. T., Flannery, B. P. 1992, Numerical Recipies in Fortran, 2nd Edition (Cambridge: Cambridge University Press)
- Reader, J., & Corliss, C. H., Eds. 1998, CRC Handbook of Chemistry and Physics, 79th Edition, (Boca Raton, FL: CRC)
- Rees, M. 1984, ARA&A, 22, 471
- Sarzi, M., Rix, H.-W., Shields, J. C., Rudnick, G., Ho, L. C., McIntosh, D. H., Filippenko, A. V., & Sargent, W. L. W. 2001, ApJ, 550, 65
- Shaw, D., & Hodge, P. 1998, STIS Instrument Science Report 98-22, (Baltimore, MD: Space Telescope Science Institute)
- Sulentic, J. W., Marziani, P., & Dultzin-Hacyan, D. 2000, ARA&A, 38, 521
- Tonry J.L., & Davis M. 1981, ApJ, 246, 666
- Tran, H. D., Tsvetanov, Z., Ford, H. C., Davies, J., Jaffe, W., van den Bosch, F. C., & Rest, A. 2001, AJ, 121, 2928
- Tremaine, S., et al. 2002, ApJ, 574, 740

- Xu, C., Baum, S. A., O’Dea, C. P., Wrobel, J. M., & Condon, J. J. 2000, AJ, 120, 2950
- van der Marel, R. P., & van den Bosch, F. C. 1998, AJ, 116, 2220
- van Dokkum, P. G., & Franx, M. 1995, AJ, 110, 2027
- Verdoes Kleijn, G. A., Baum, S. A., de Zeeuw, P. T., & O’Dea, C. P. 1999, AJ, 118, 2592
- Verdoes Kleijn, G. A., van der Marel, R. P., Carollo, C. M., & de Zeeuw, P. T. 2000, AJ, 120, 1221
- Verdoes Kleijn, G. A., Baum, S. A., de Zeeuw, P. T., & O’Dea, C. P. 2002, AJ, 123, 1334
- Verdoes Kleijn, G. A., van der Marel, R. P., de Zeeuw, P. T., Noel-Storr, J., & Baum, S. A. 2002, AJ, 124, 2524
- Wagner, S. J., Bender, R., Möllenhof, C. 1988, A&A, 195, L5
- Wallerstein, G., Gilroy, K. K., Zethson, T., Johansson, S., & Hamann, F. 2001, PASP, 113, 1210

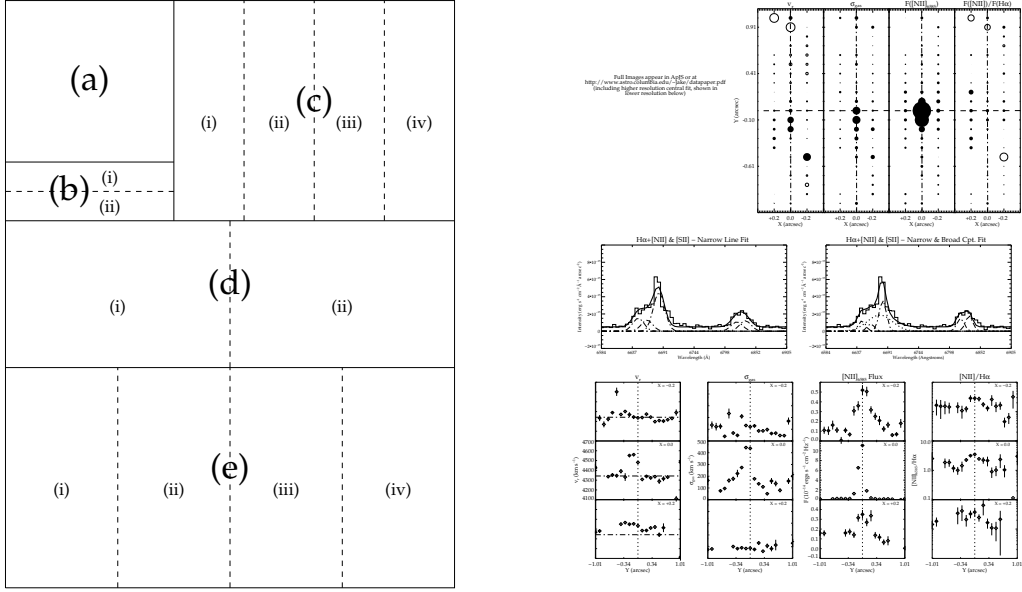


Fig. 1.— Key to plots. **Region (a):** the HST acquisition image for each galaxy observed is shown with the positions of the observed long slits overlaid. The relative position angles of the galaxy major axes measured from the central isophotes (dashed lines) and the arcsecond scale radio jets (dotted lines) are shown. These lines cross, and a North-East indicator is drawn, at the location of the central pixel (see text). **Region (b):** (i) the central portion of the reduced 2-D spectrum from the central slit position is shown along with (ii) an image created from fitting a set of 5 Gaussian lines to the same. **Region (c):** plots representing the two-dimensional distributions of parameters measured by fitting a one Gaussian per emission line model to spectra from the nuclear region. The dashed and dash-dot lines indicate the directions of the minor and major axes respectively. The lines cross at the location of the central pixel. We show: (i) radial velocity (filled circles represent velocities greater than the mean, empty circles represent velocities less than the mean and the radius of each point $[i,j]$ is proportional to $|v_{i,j} - v_{mean}|$); (ii) velocity dispersion (the radius of the circle is proportional to $\sigma_{i,j}$); (iii) integrated line flux (the area of each point is proportional to $F_{i,j}$); and (iv) $[\text{N II}]_{6585} / \text{H}\alpha$ ratio (The radius of each circle is proportional to $\log(F([\text{N II}]_{6585})/F(\text{H}\alpha))$). **Region (d):** single Gaussian per line fit and residuals without (i) and with (ii) the additional free component described in the text for the central spectrum of each galaxy. **Region (e):** plots of (i) radial velocity, (ii) velocity dispersion, (iii) $[\text{N II}]$ line flux and (iv) $[\text{N II}]_{6585} / \text{H}\alpha$ ratio along each slit measured by fitting a one Gaussian per line model to the emission line spectra. The vertical dotted line indicates the Y position of the central row. The dash-dot line in the velocity panel indicates the quoted recession velocity for the galaxy (see Table 1).

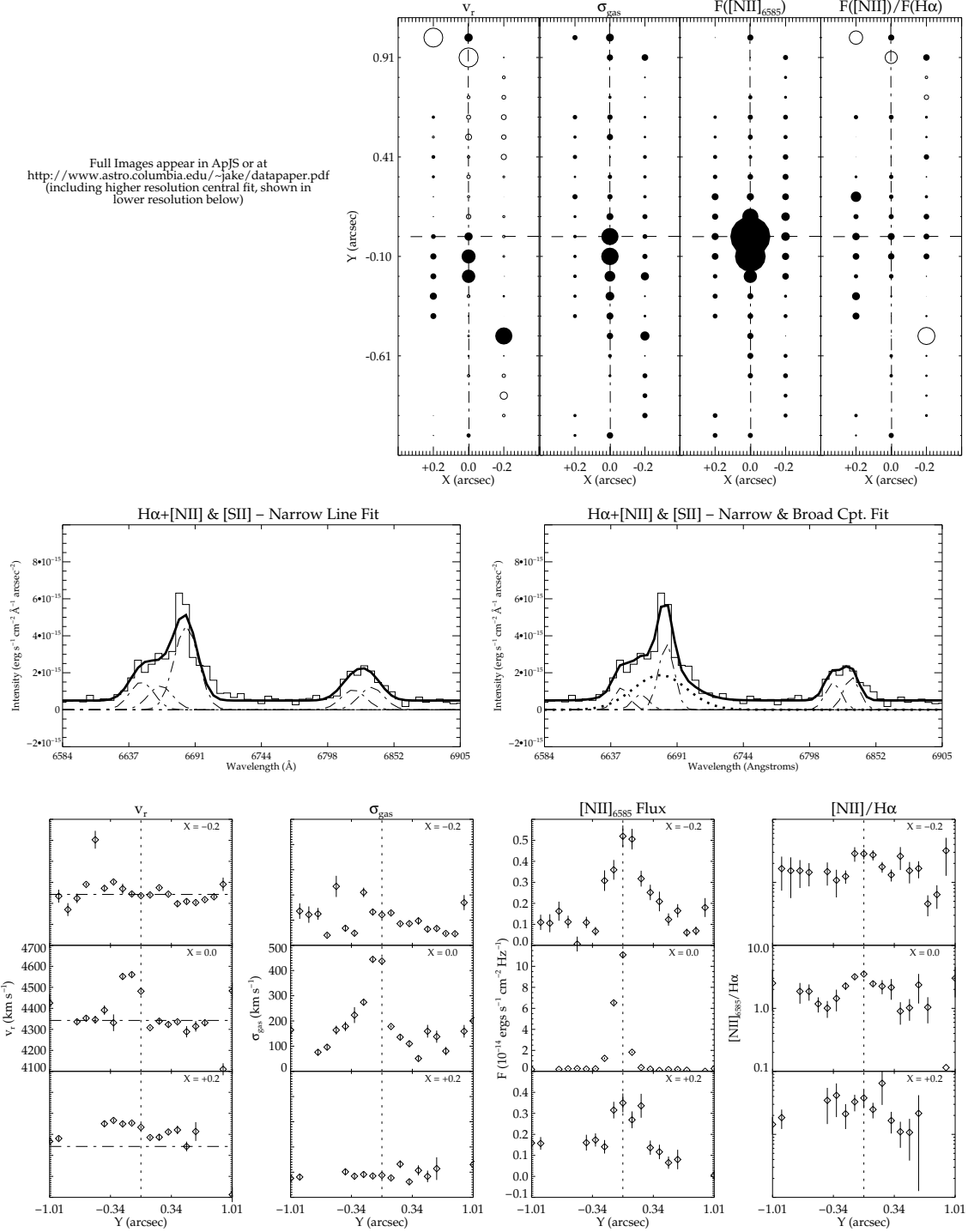


Fig. 2.— Observation and fit data for NGC 193, see Figure 1 for description.

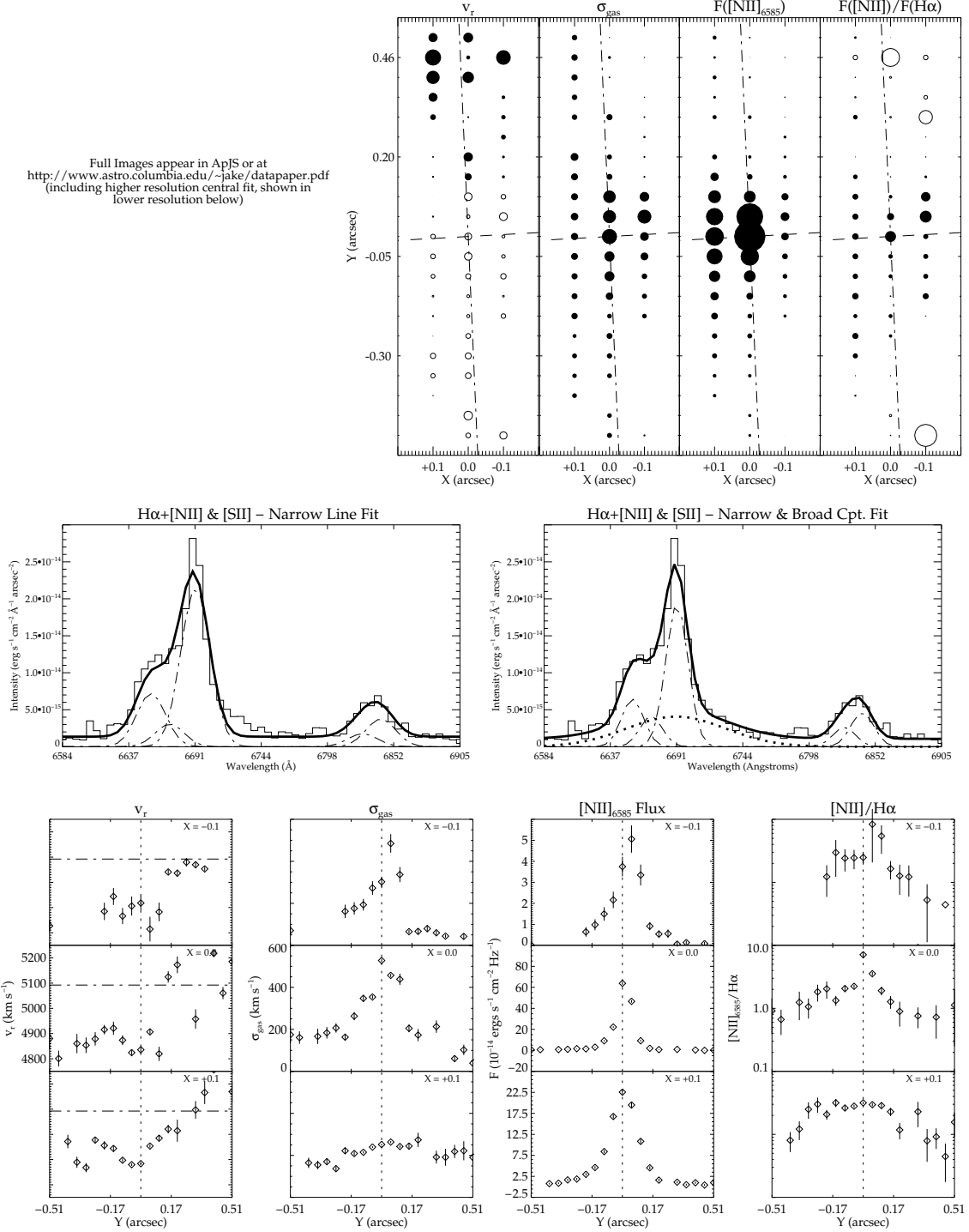


Fig. 3.— Observation and fit data for NGC 315, see Figure 1 for description.

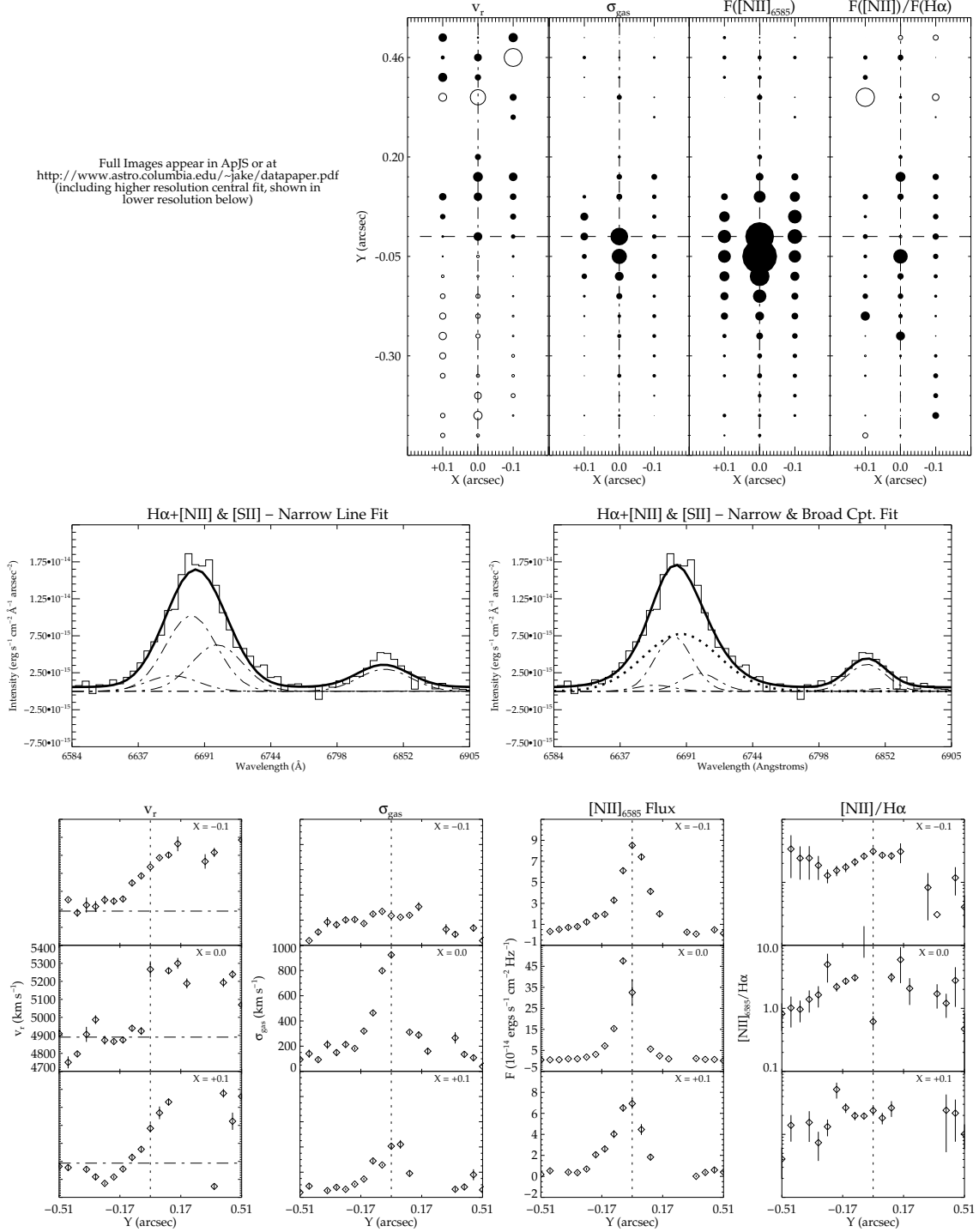


Fig. 4.— Observation and fit data for NGC 383, see Figure 1 for description.

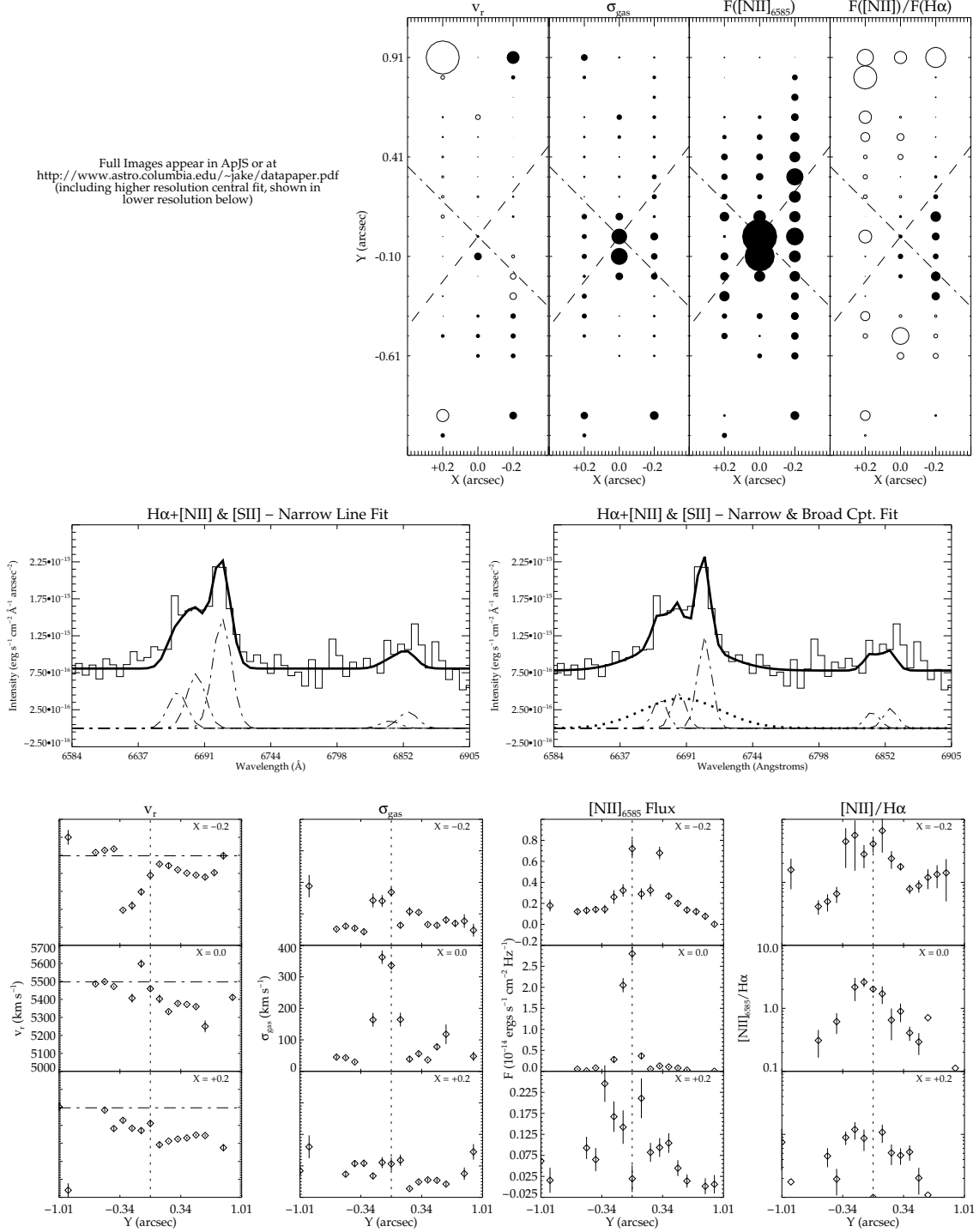


Fig. 5.— Observation and fit data for NGC 541, see Figure 1 for description.

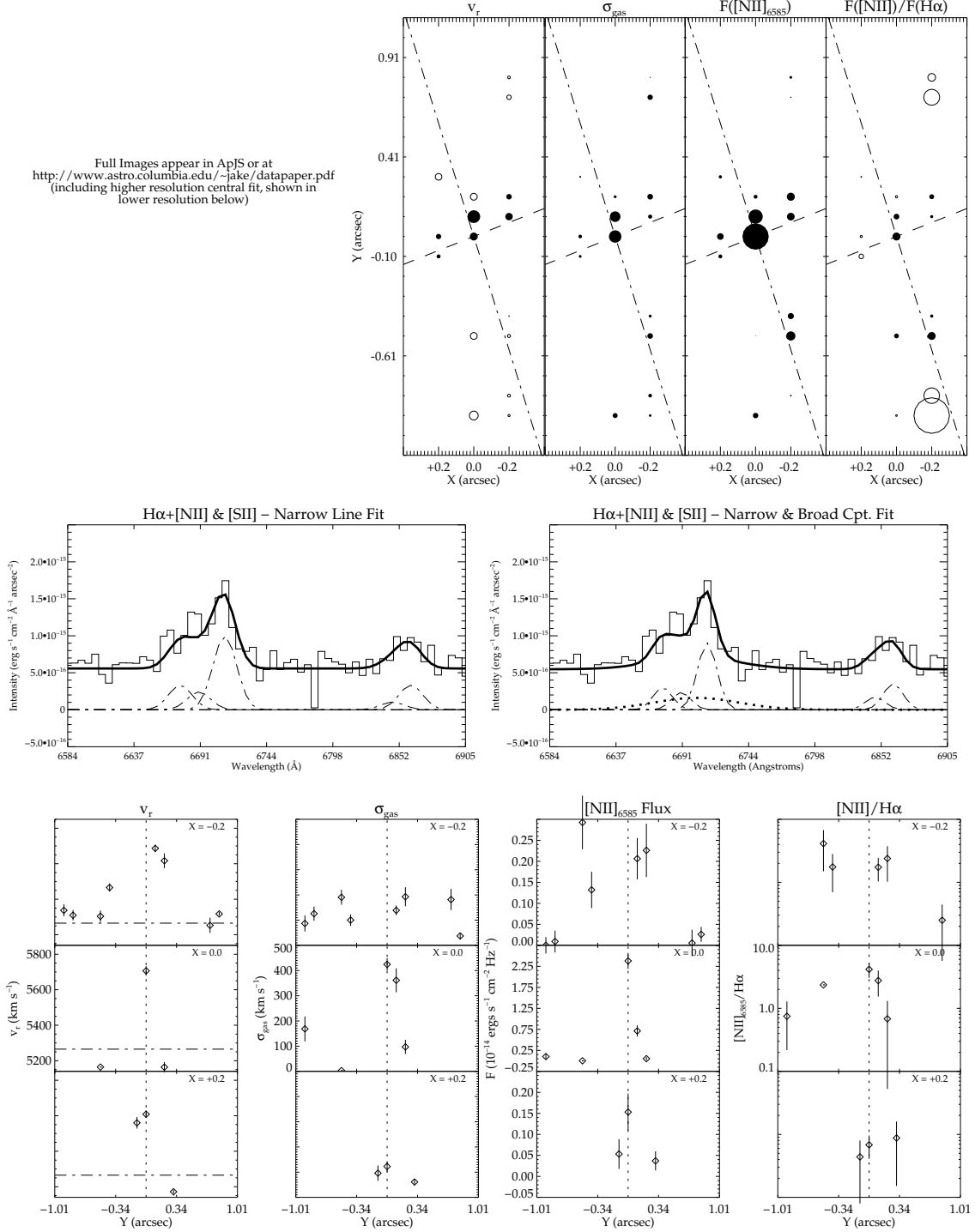


Fig. 6.— Observation and fit data for NGC 741, see Figure 1 for description.

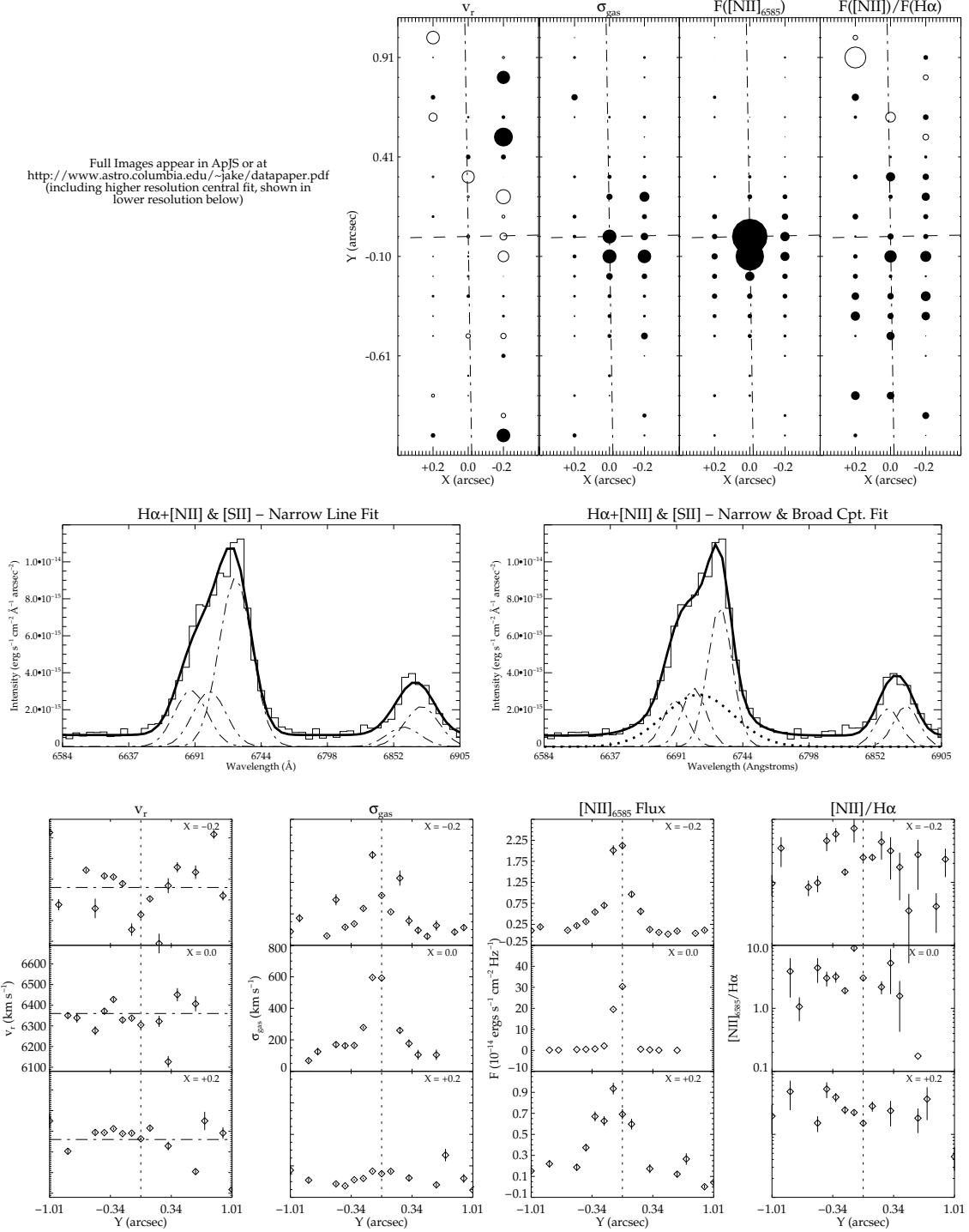


Fig. 7.— Observation and fit data for UGC 1841, see Figure 1 for description.

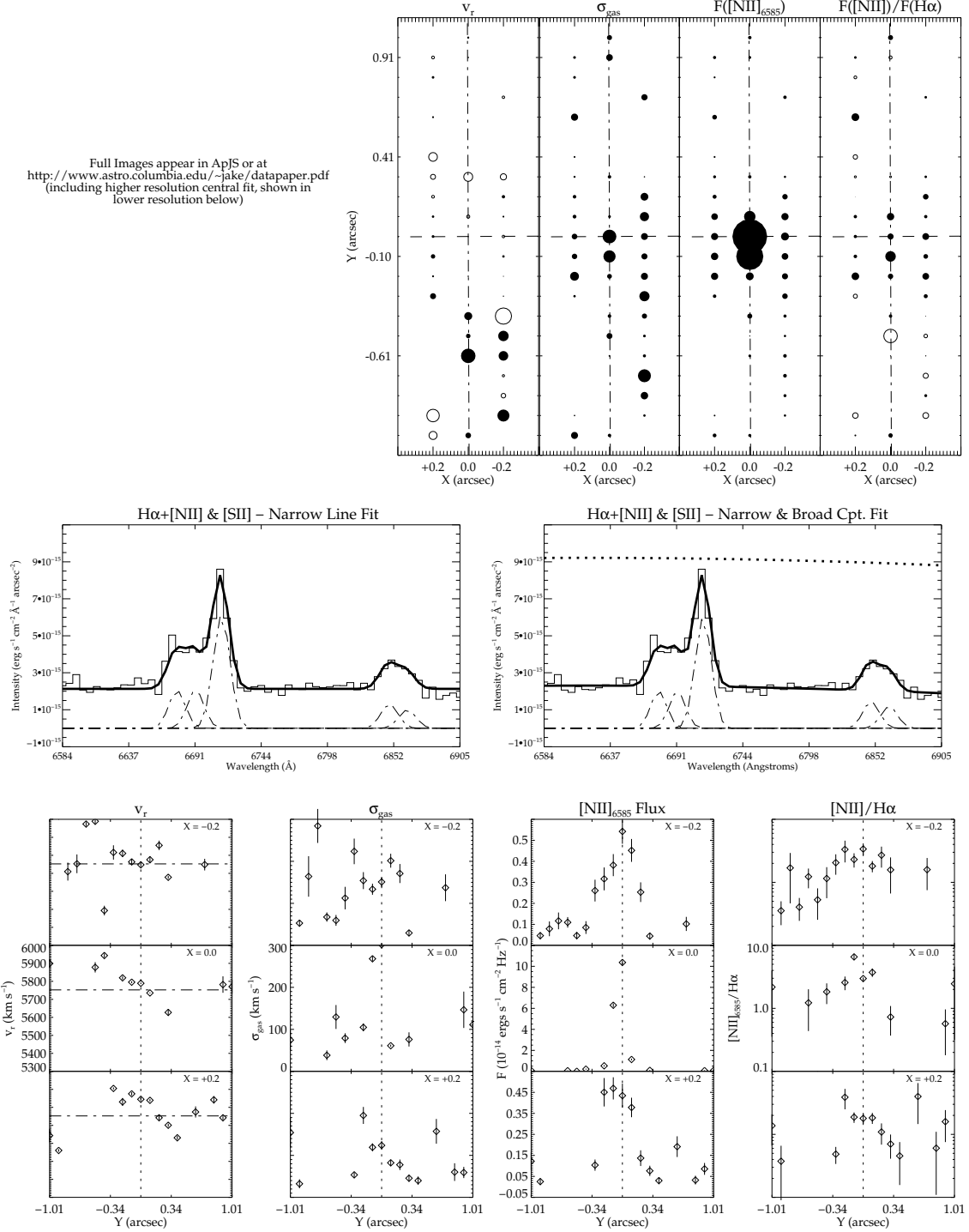


Fig. 8.— Observation and fit data for NGC 2329, see Figure 1 for description.

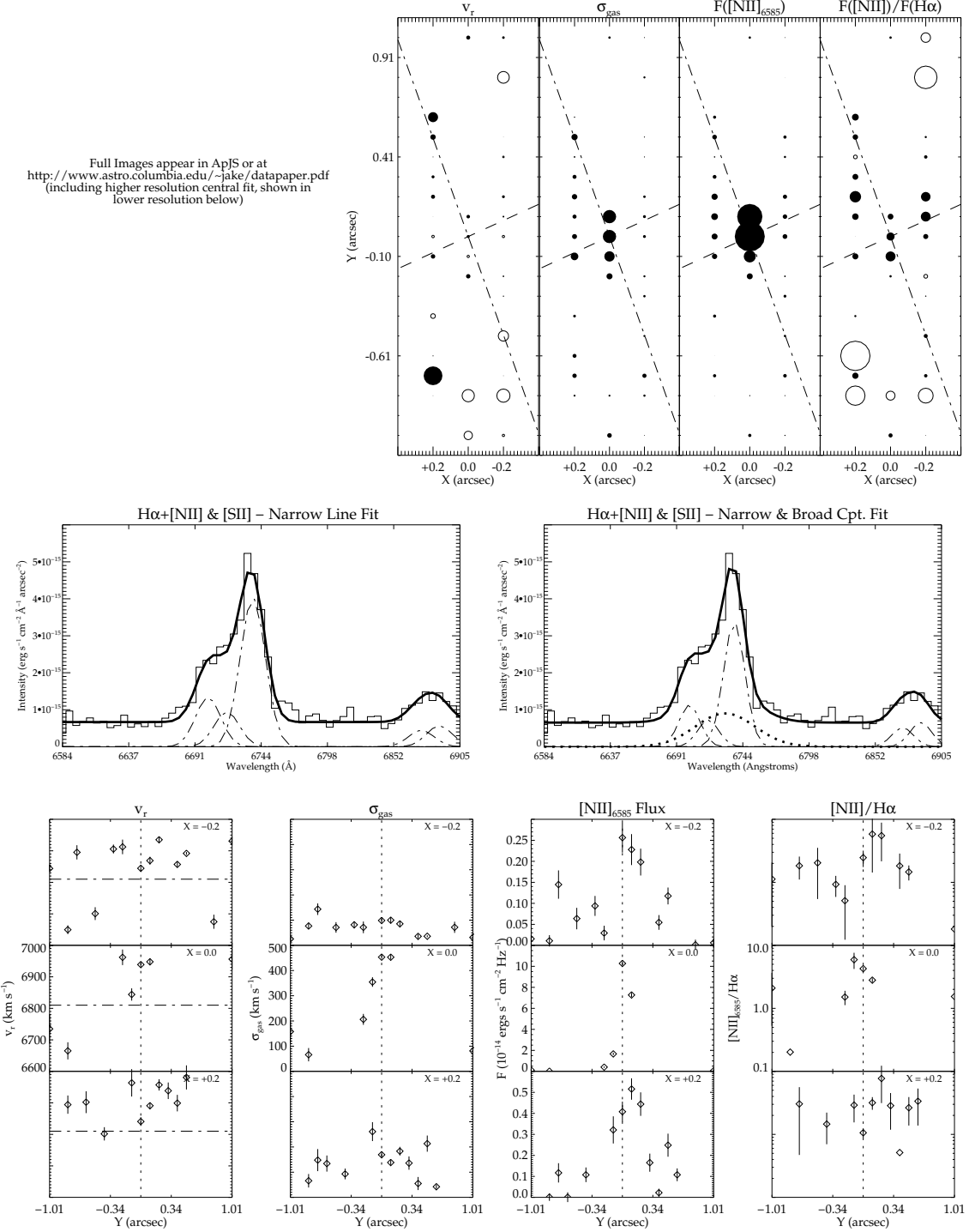


Fig. 9.— Observation and fit data for NGC 2892, see Figure 1 for description.

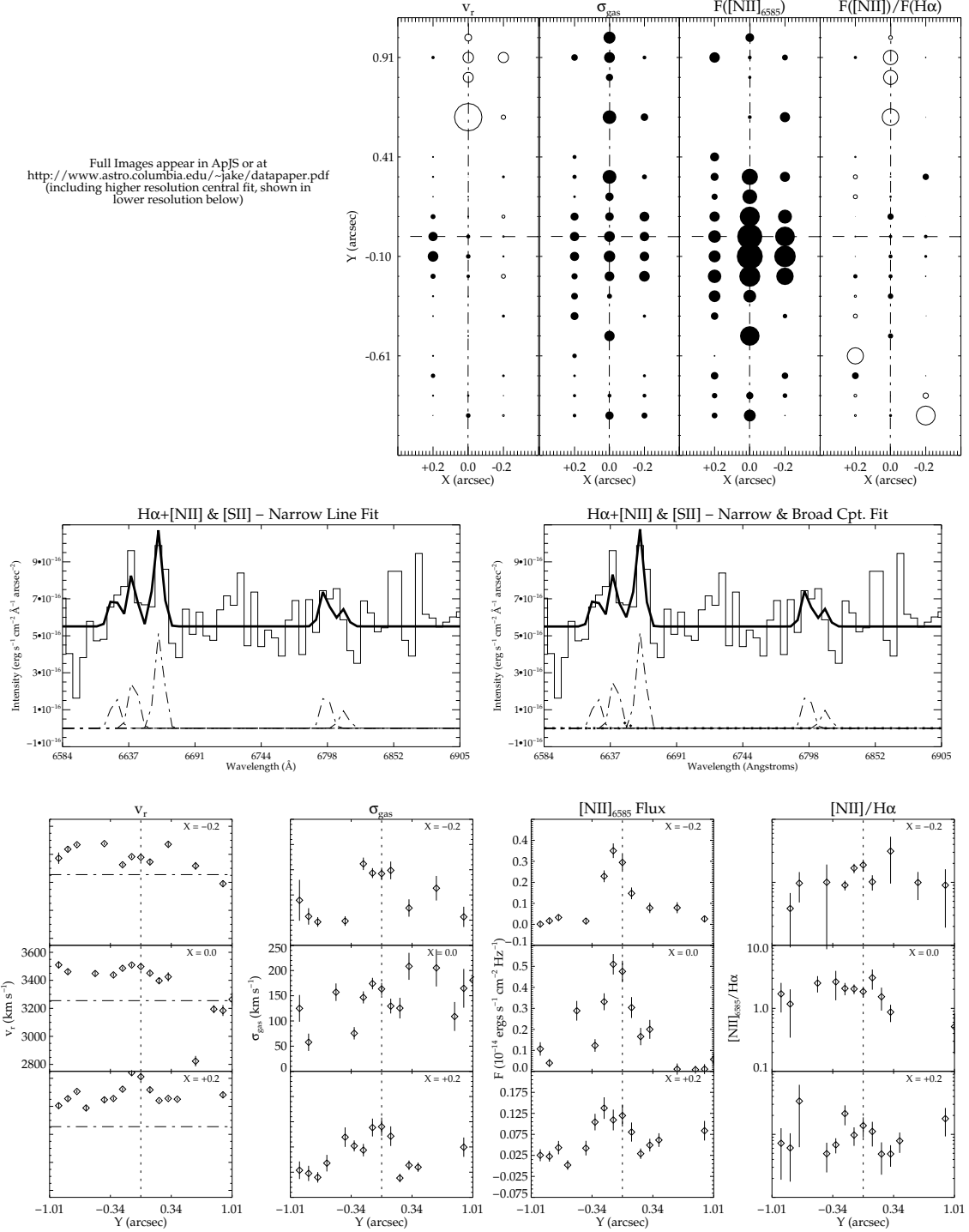


Fig. 10.— Observation and fit data for NGC 3801, see Figure 1 for description.

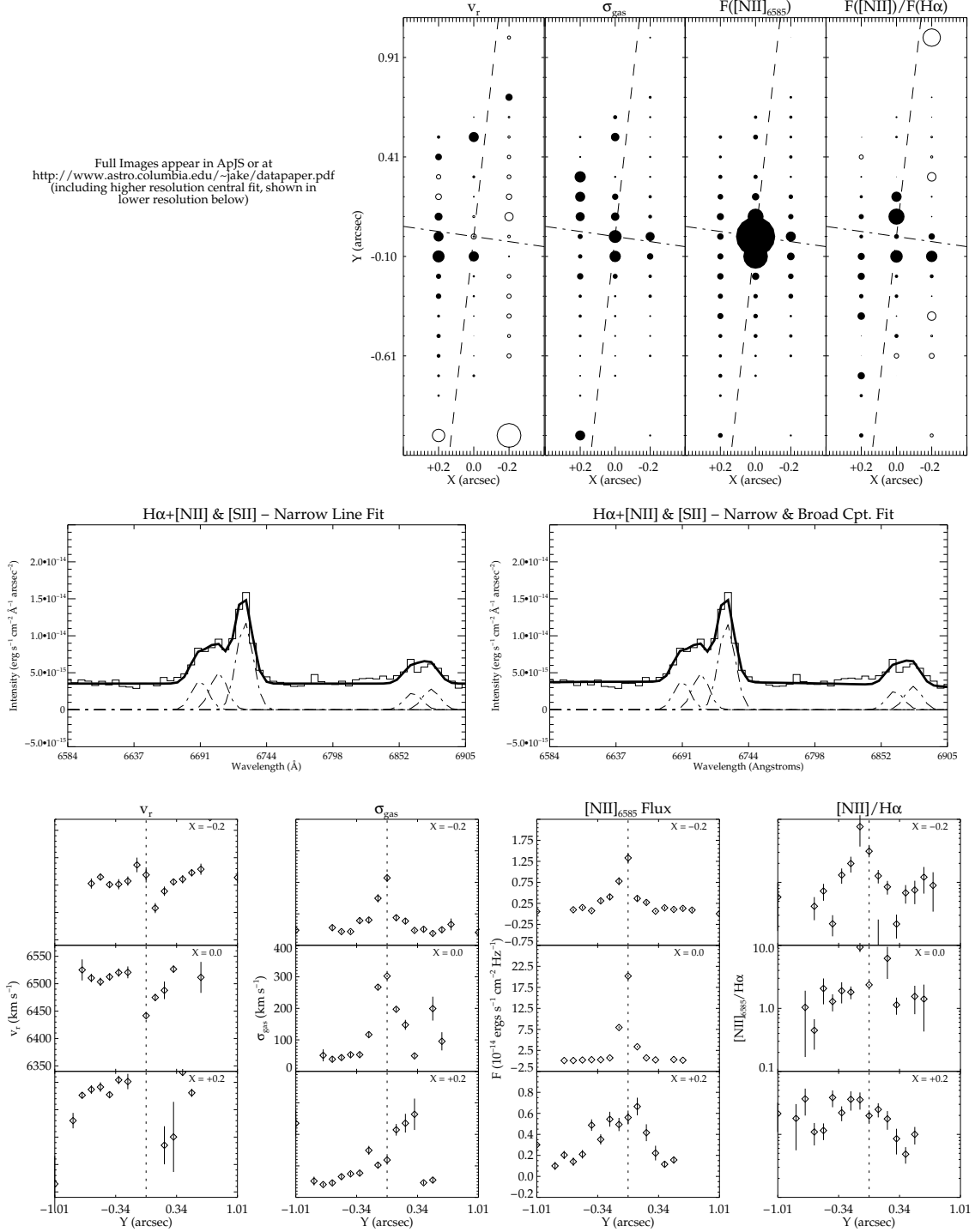


Fig. 11.— Observation and fit data for NGC 3862, see Figure 1 for description.

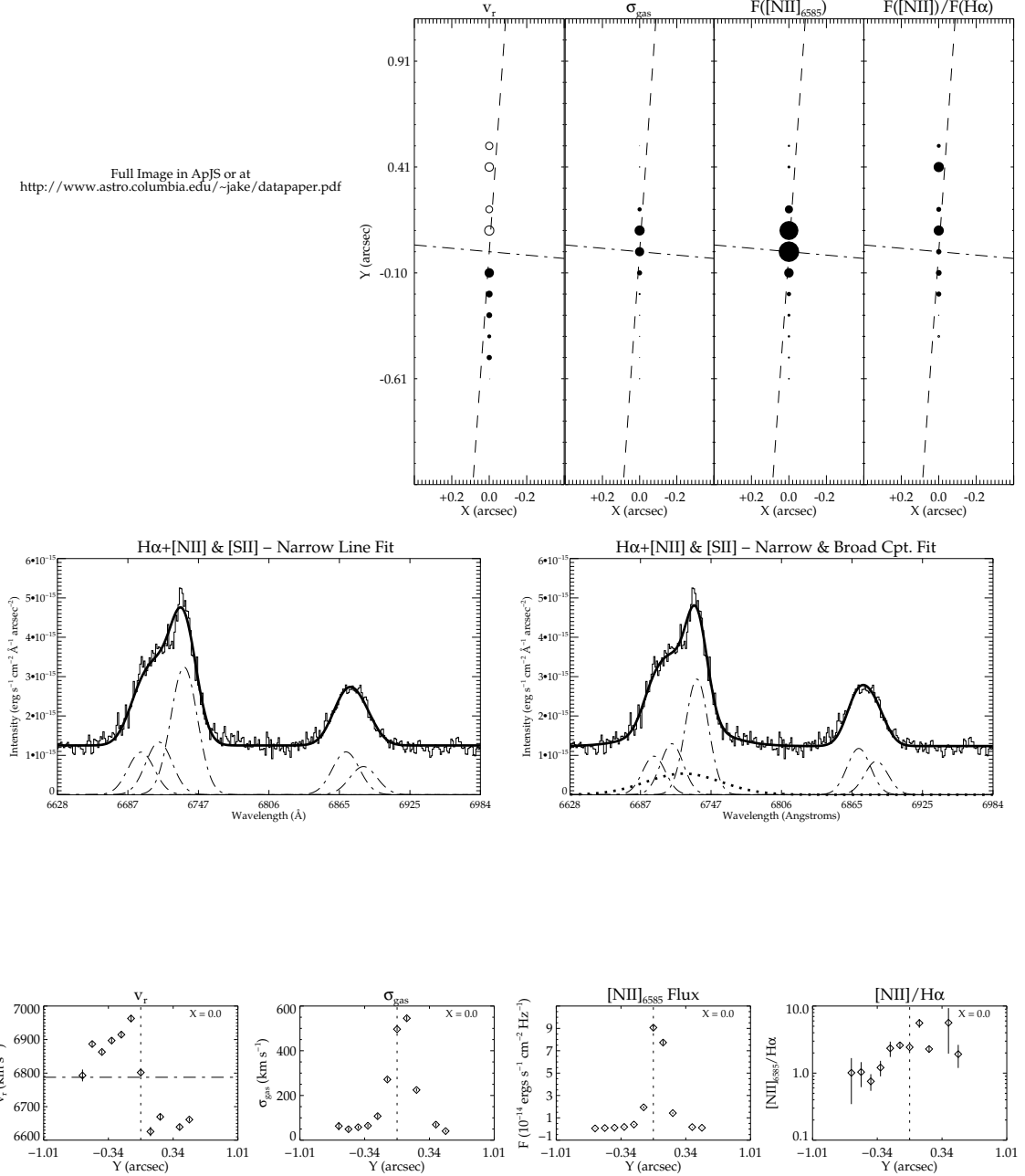


Fig. 12.— Observation and fit data for UGC 7115, see Figure 1 for description.

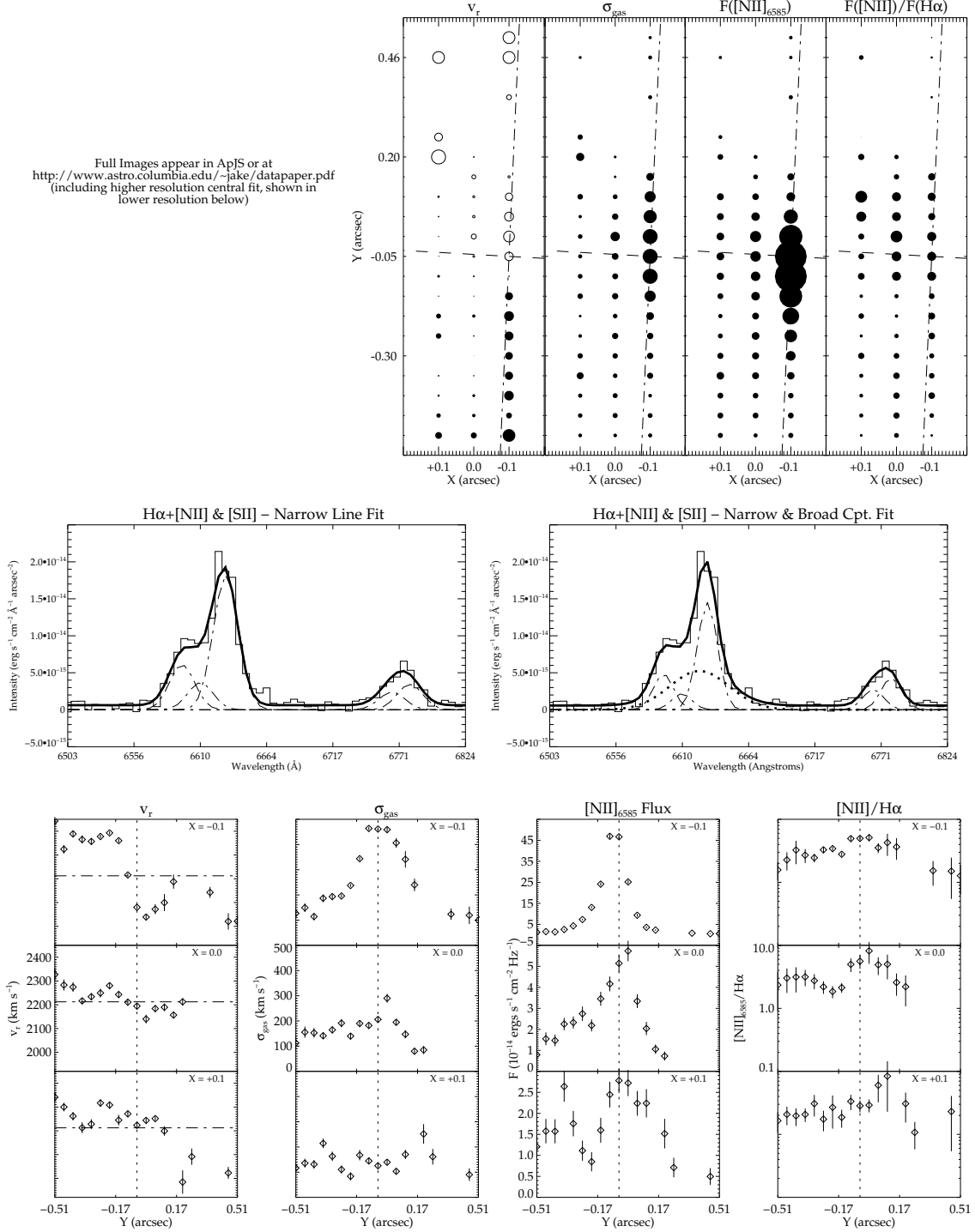


Fig. 13.— Observation and fit data for NGC 4261, see Figure 1 for description.

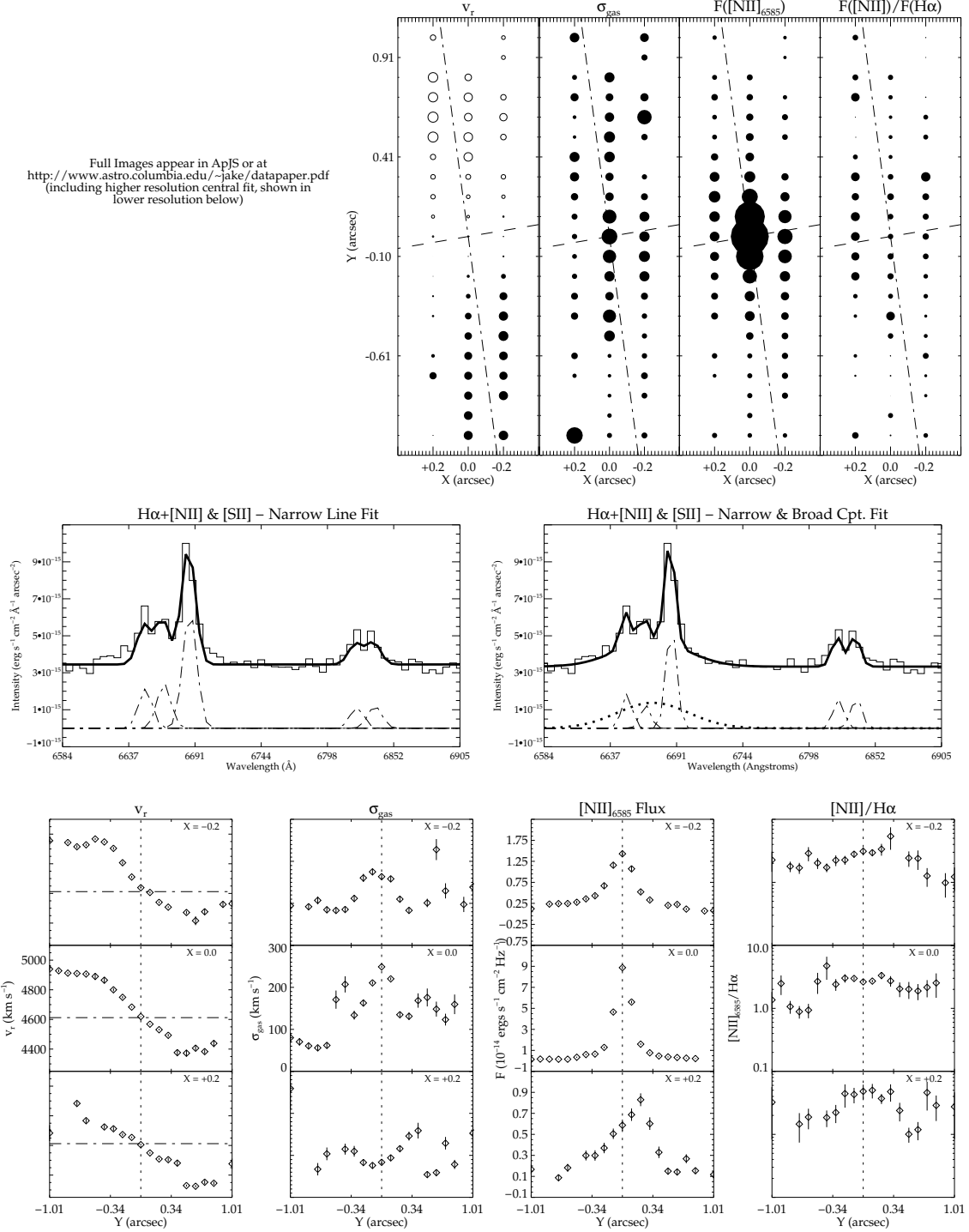


Fig. 14.— Observation and fit data for NGC 4335, see Figure 1 for description.

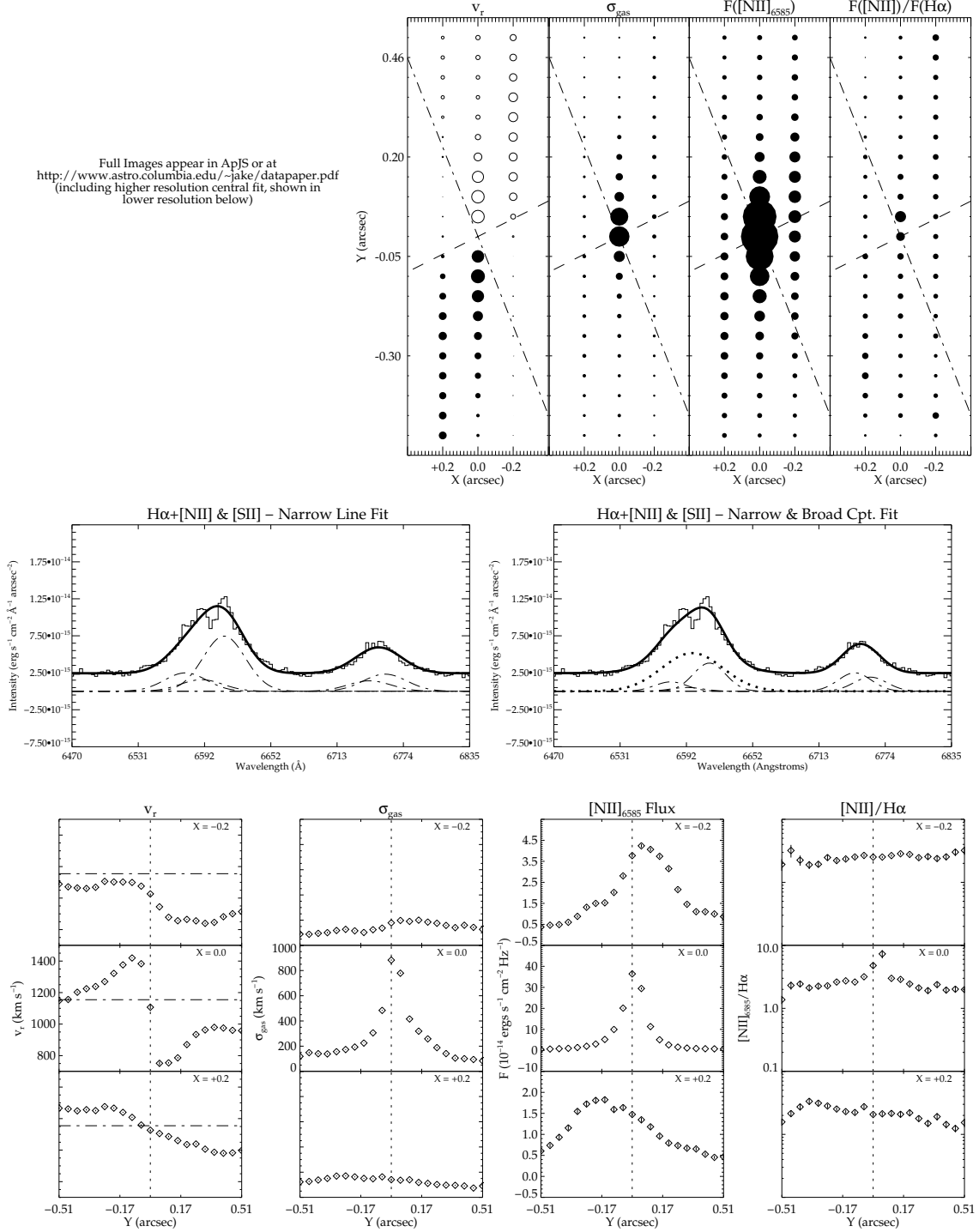


Fig. 15.— Observation and fit data for NGC 4374, see Figure 1 for description.

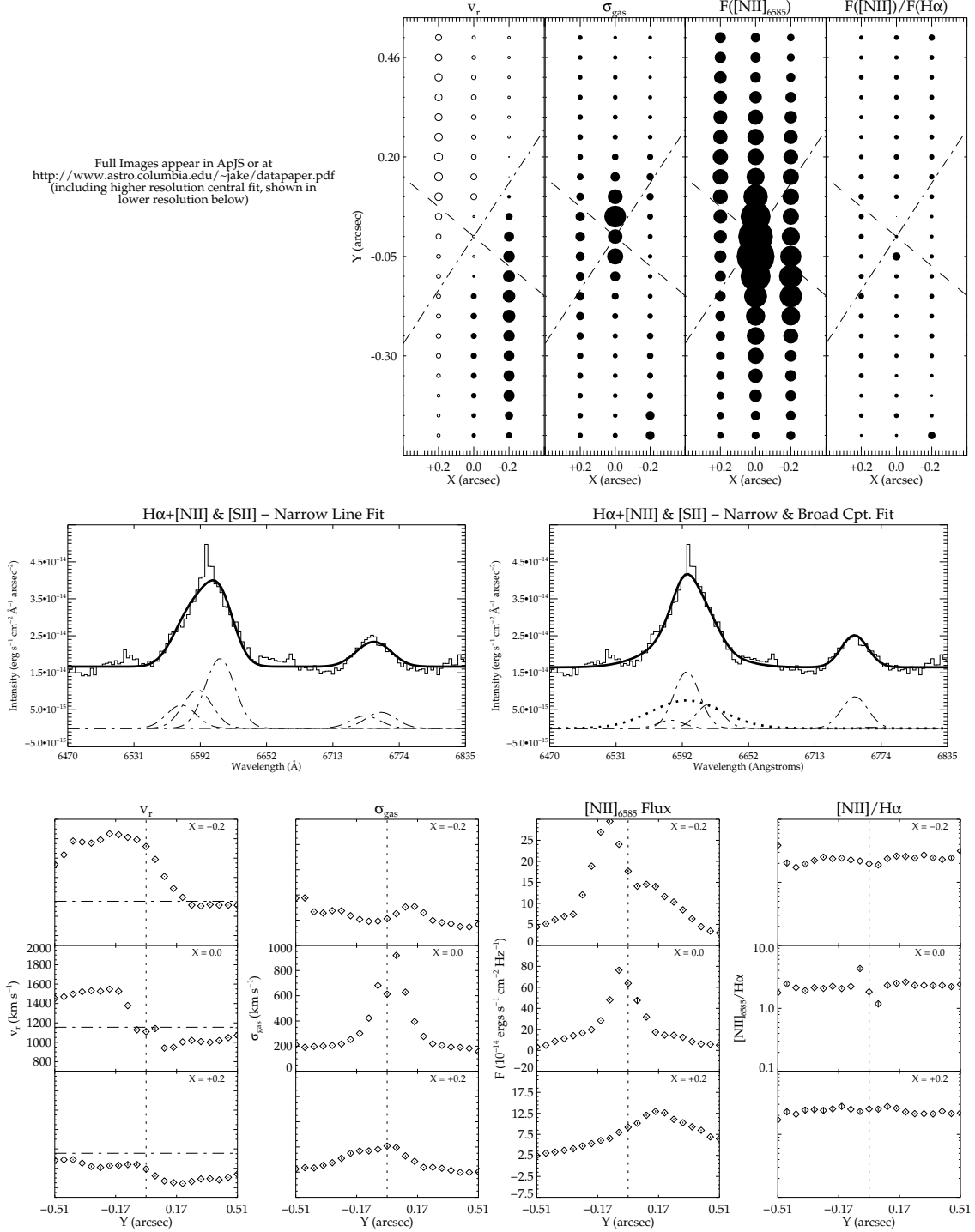


Fig. 16.— Observation and fit data for NGC 4486, see Figure 1 for description.

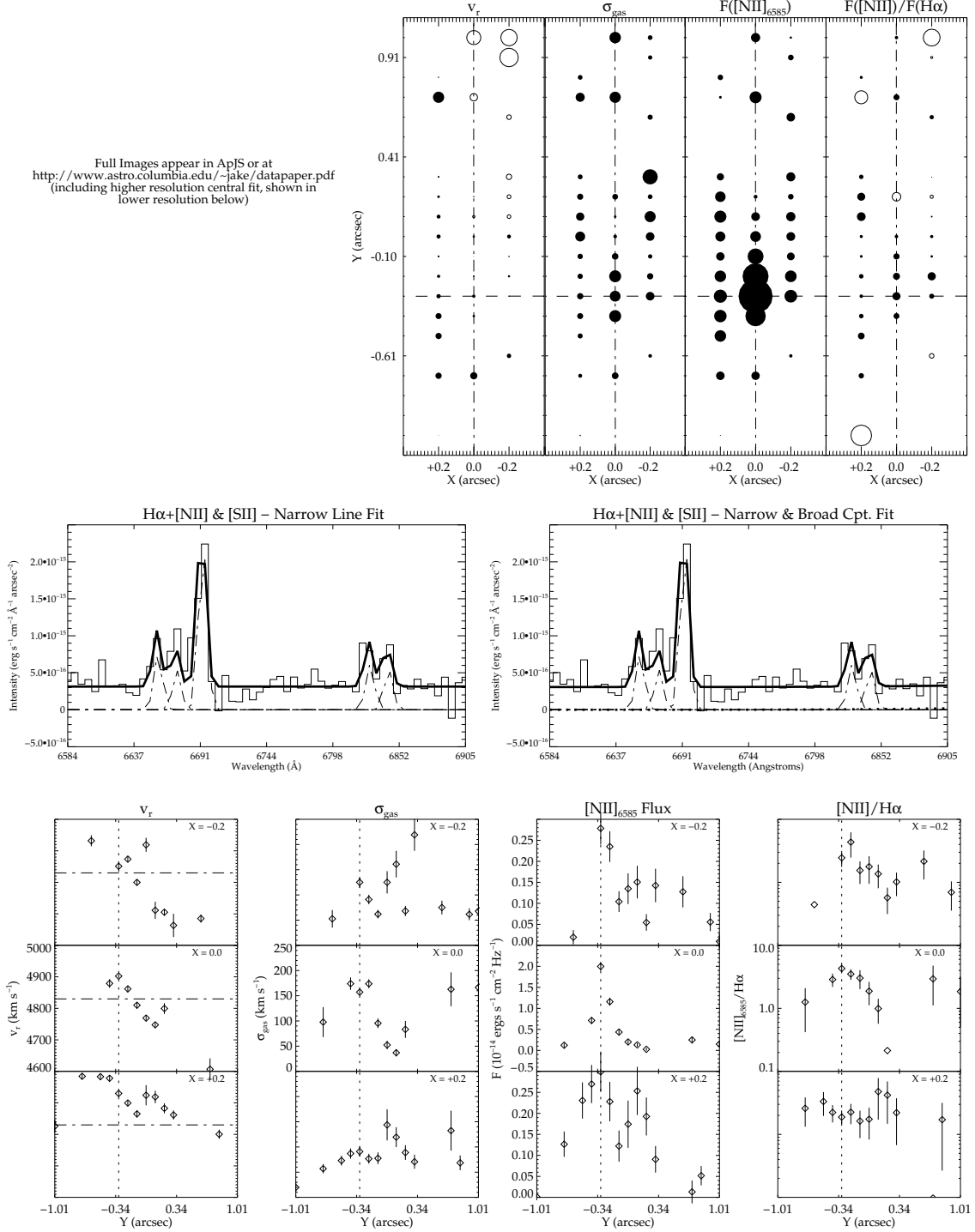


Fig. 17.— Observation and fit data for NGC 5127, see Figure 1 for description.

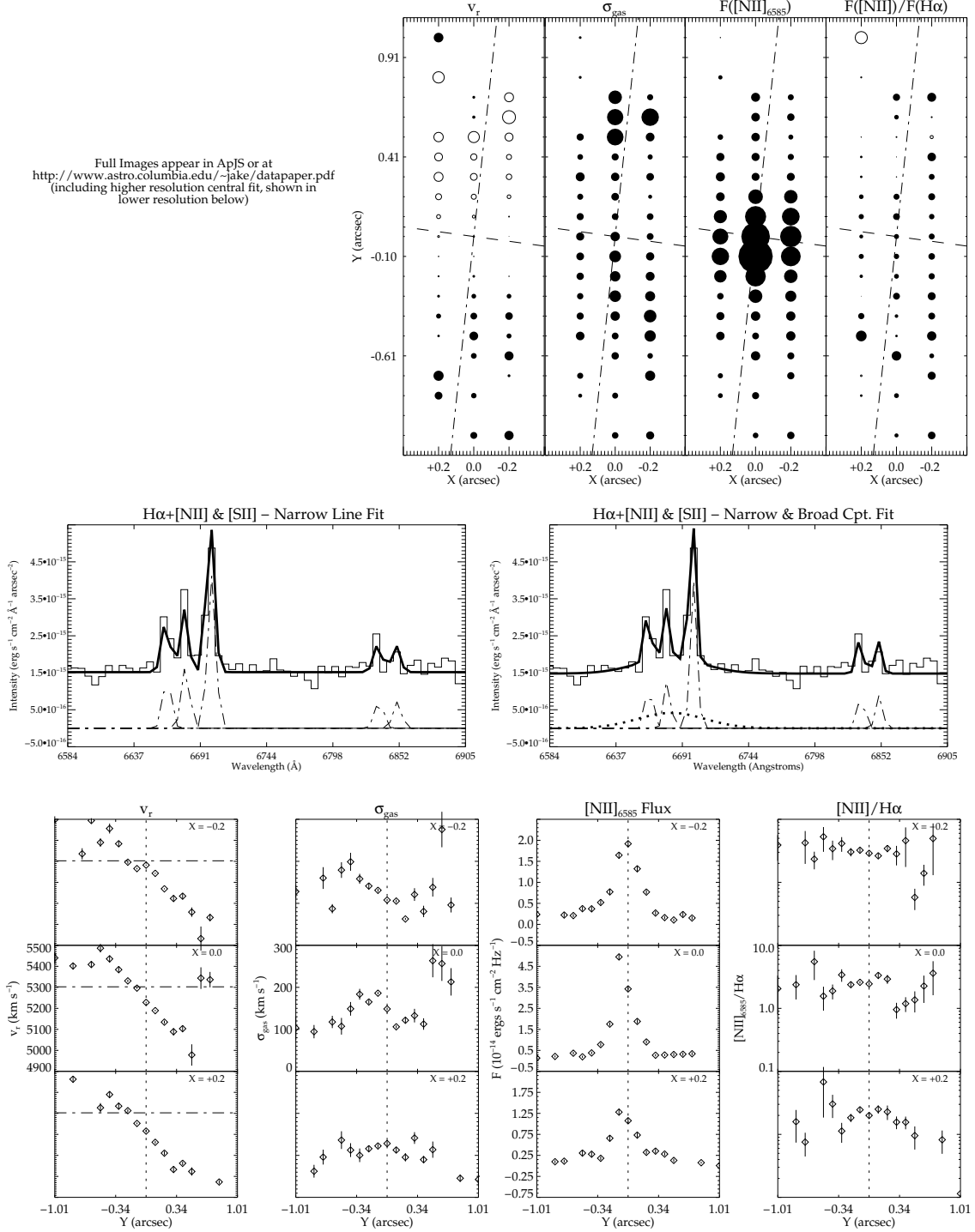


Fig. 18.— Observation and fit data for NGC 5141, see Figure 1 for description.

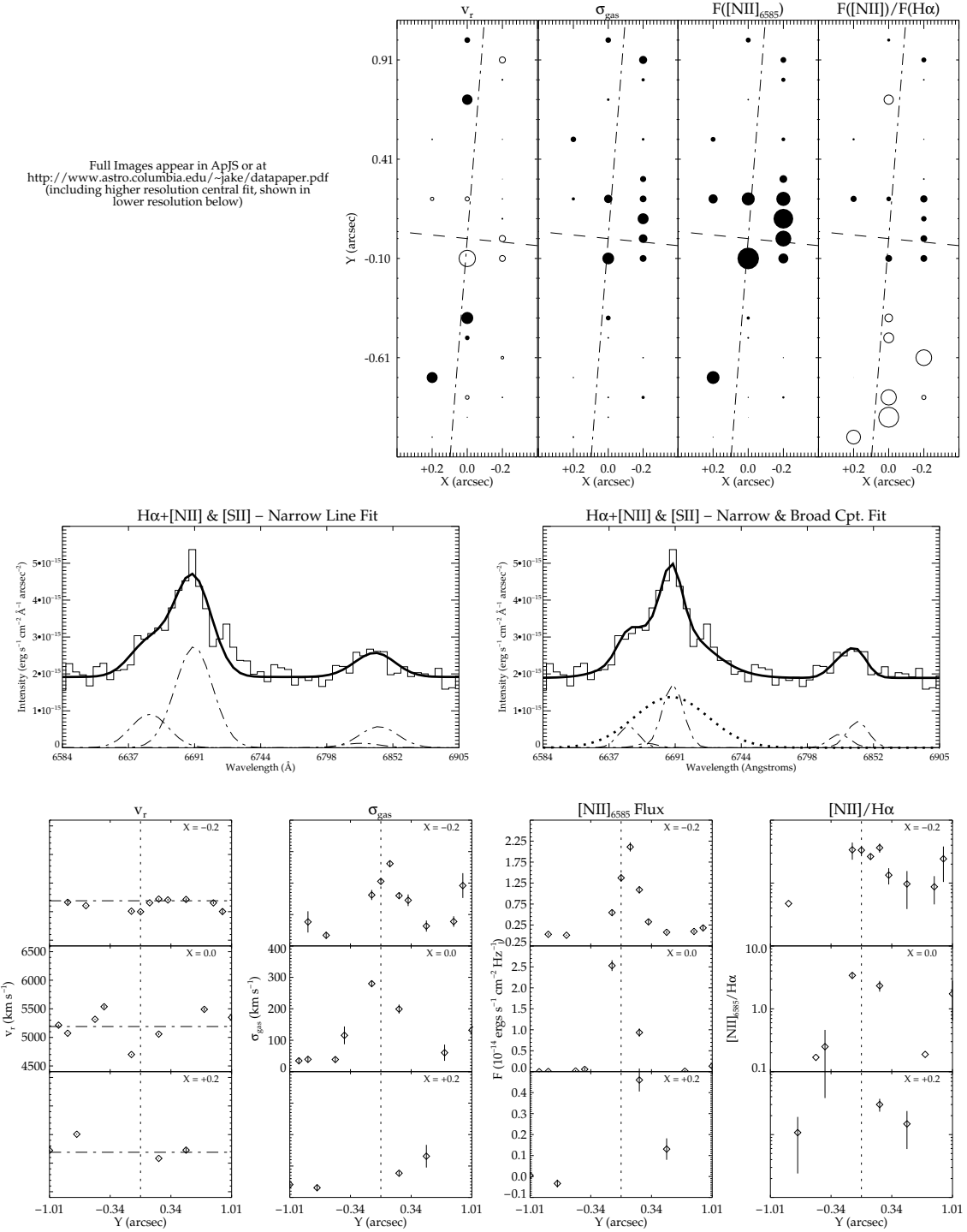


Fig. 19.— Observation and fit data for NGC 5490, see Figure 1 for description.

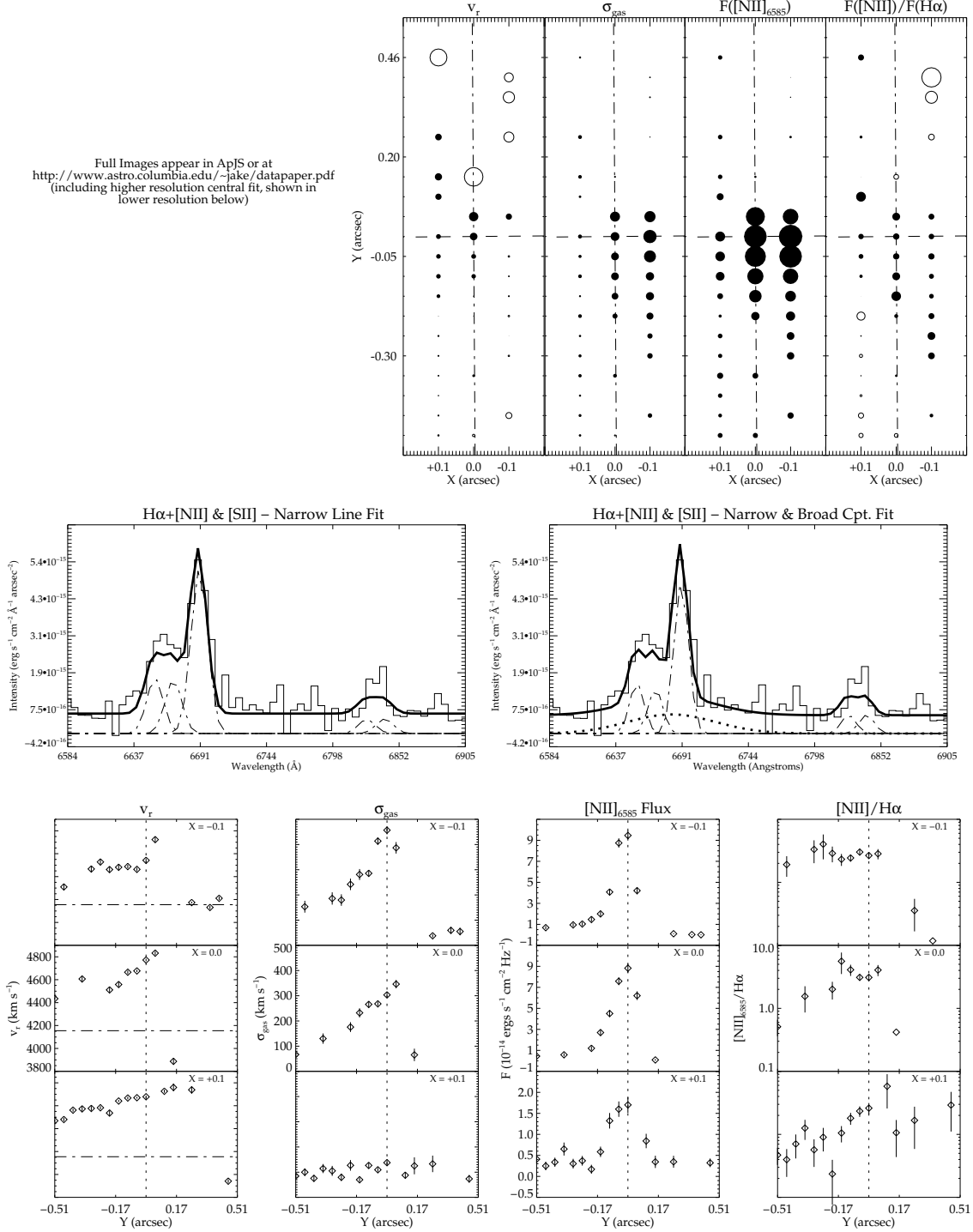


Fig. 20.— Observation and fit data for NGC 7052, see Figure 1 for description.

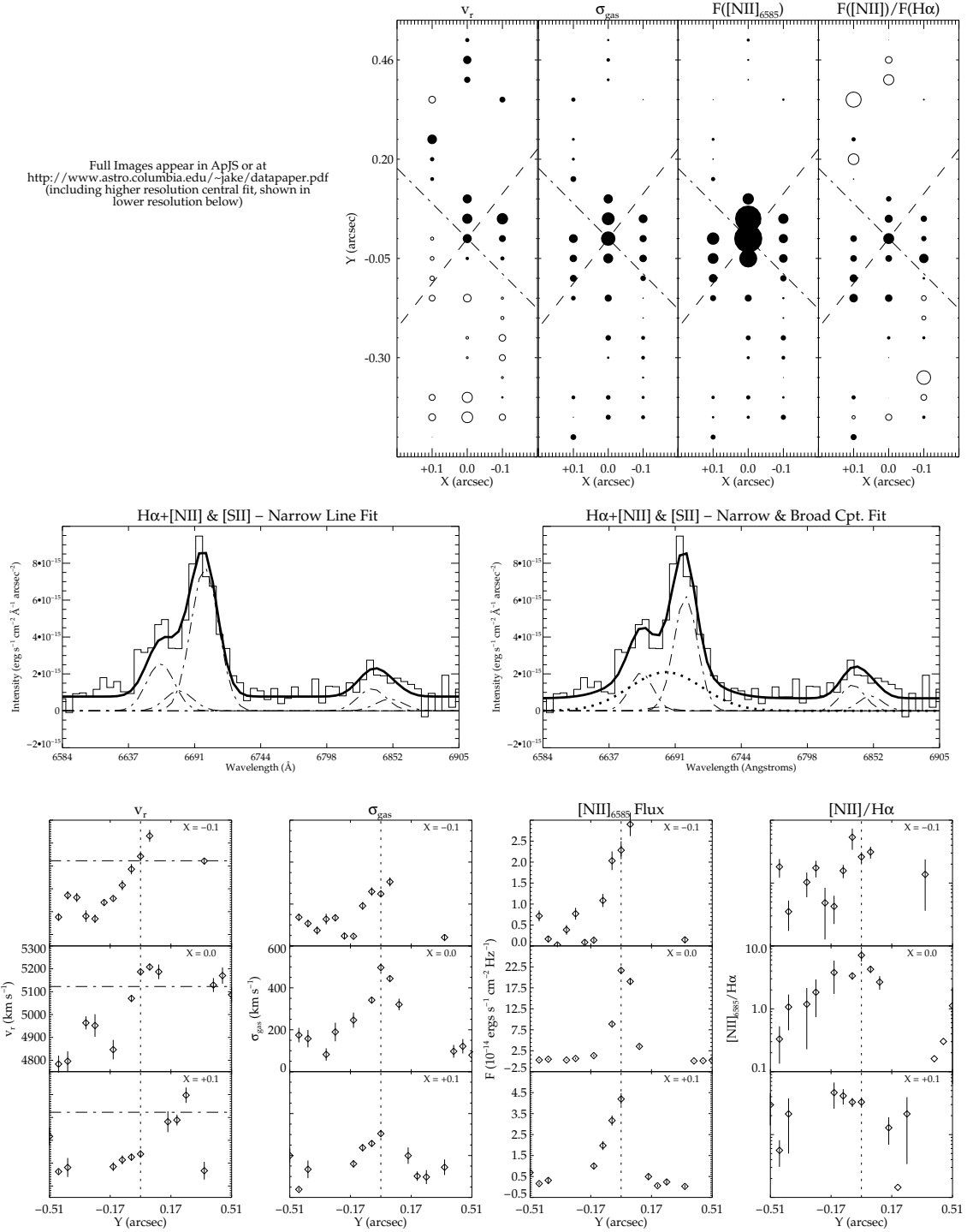


Fig. 21.— Observation and fit data for UGC 12064, see Figure 1 for description.

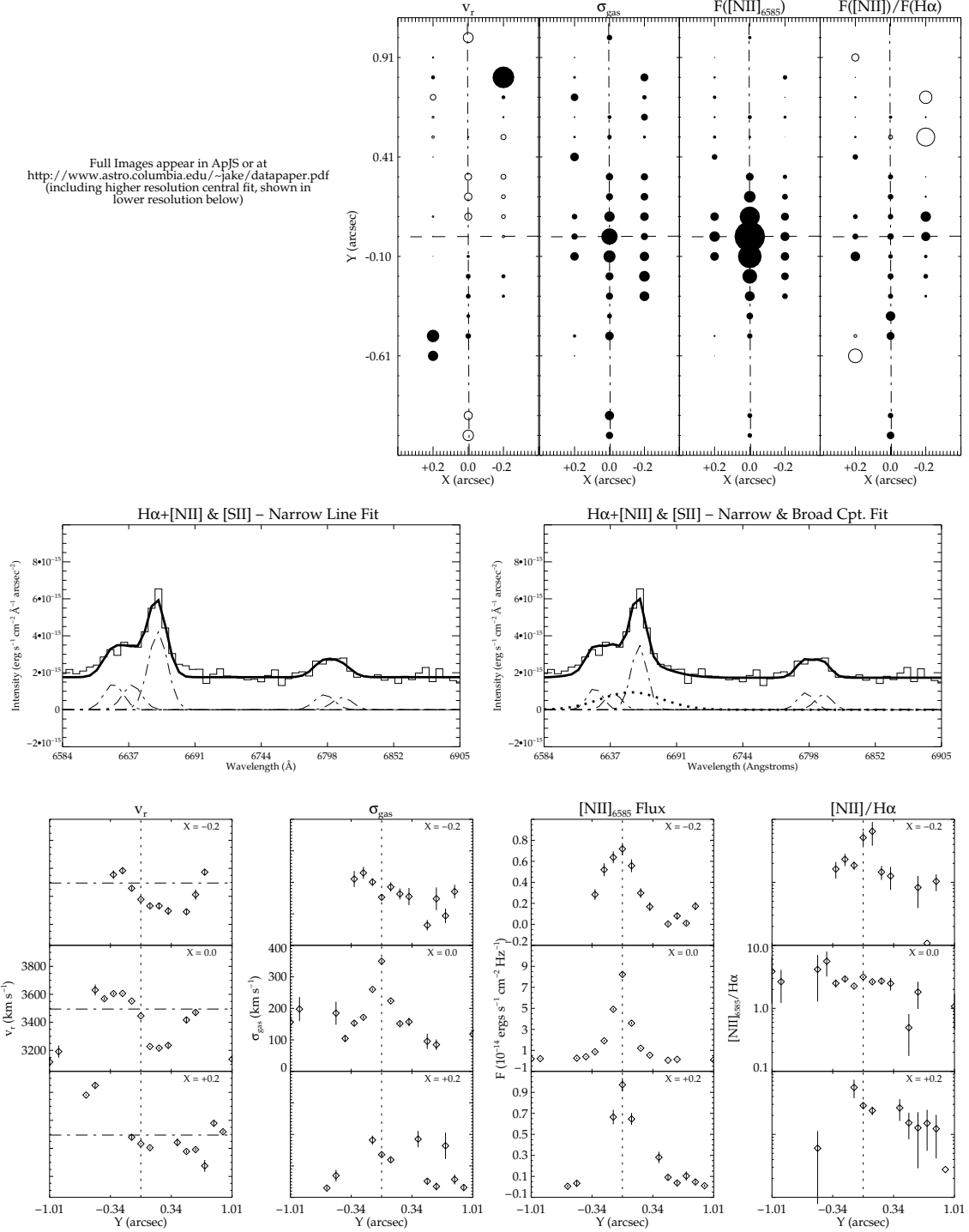


Fig. 22.— Observation and fit data for NGC 7626, see Figure 1 for description.

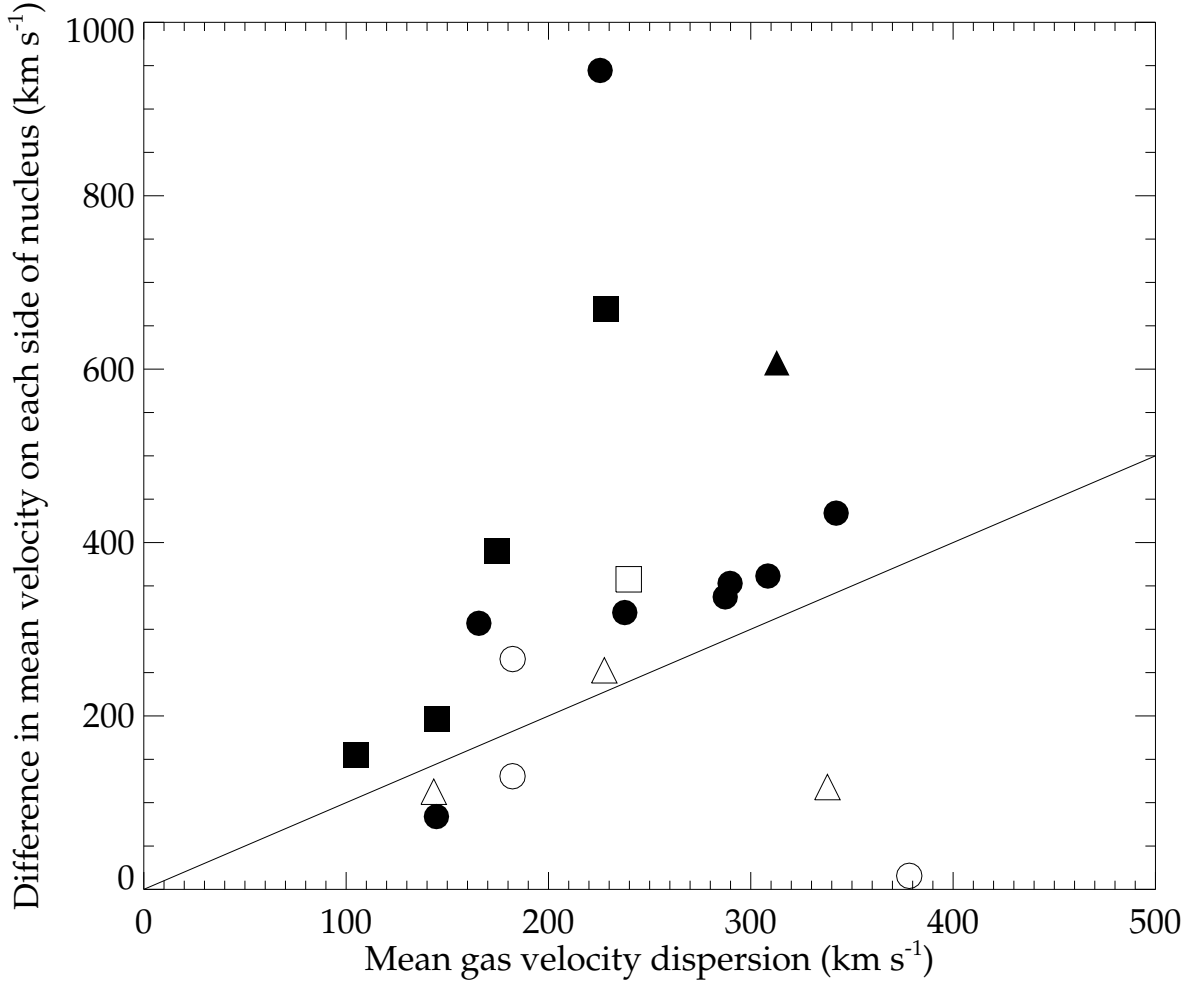


Fig. 23.— Difference in mean velocity within 100 pc of each side of the nucleus ($\Delta_{100\text{pc}}$, see text) as a function of the mean gas velocity dispersion within 100 pc of the nucleus ($\overline{\sigma}_{100\text{pc}}$). The different kinematic classes and dust morphologies are indicated. Filled symbols represent rotators: with dust disks (●), with dust lanes (■) or with irregular dust (▲); Empty symbols represent non-rotators: with dust disks (○), with dust lanes (□) or with no-dust or irregular dust (△). The solid line is the 1:1 ratio between $\Delta_{100\text{pc}}$ and $\overline{\sigma}_{100\text{pc}}$, indicating regions where organized motions (above the line) or random motions (below the line) dominate.

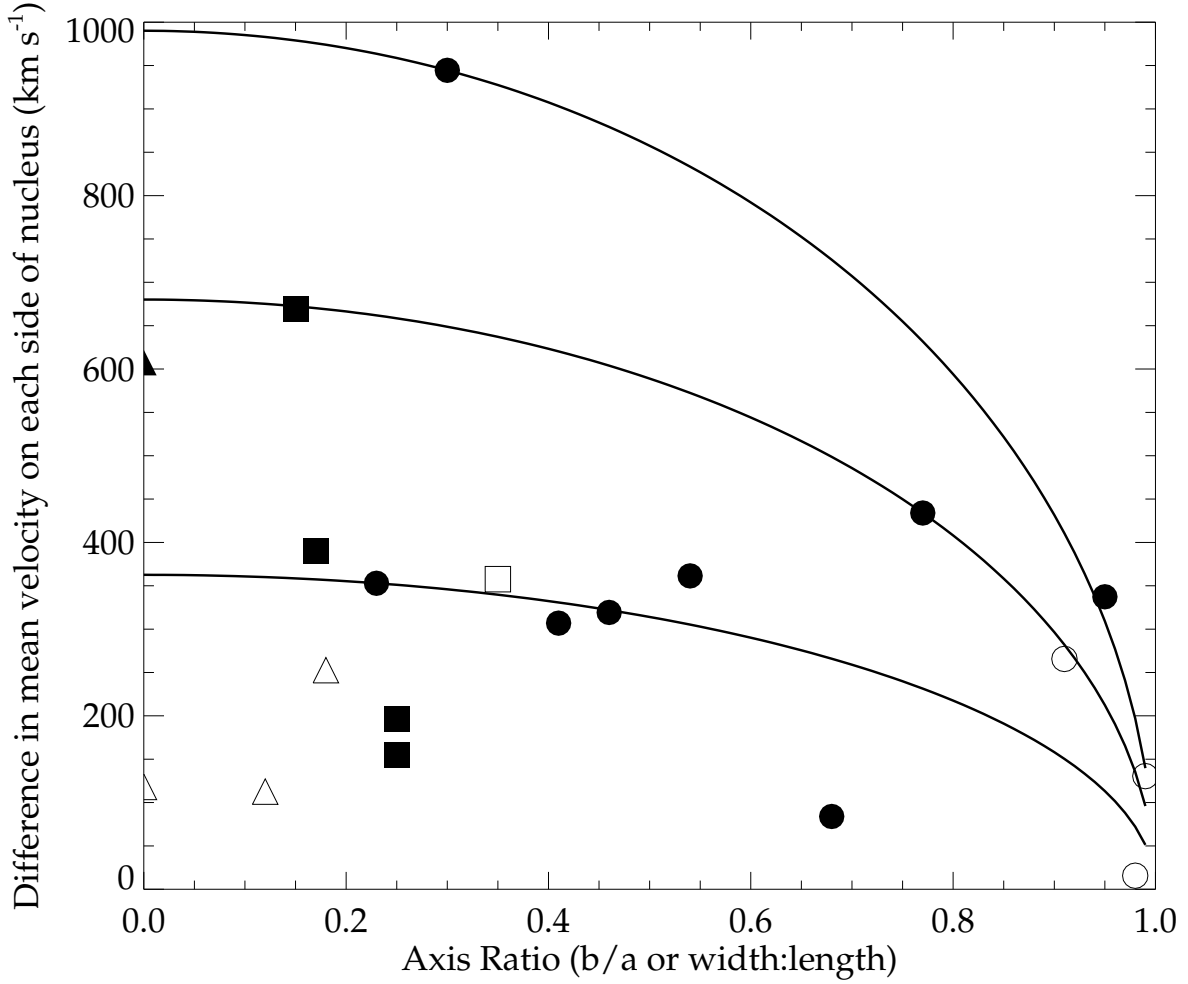


Fig. 24.— Difference in mean velocity within 100 pc of each side of the nucleus ($\Delta_{100\text{pc}}$, see text) as a function of dust disk axis ratio (b/a) or dust lane *width : length* ratio, which is an indicator of inclination. The different kinematic classes and dust morphologies are indicated. Filled symbols represent rotators: with dust disks (\bullet), with dust lanes (\blacksquare) or with irregular dust (\blacktriangle); Empty symbols represent non-rotators: with dust disks (\circ), with dust lanes (\square) or with no-dust or irregular dust (\triangle). The solid lines are loci for disks with the same intrinsic $\Delta_{100\text{pc}}$ (990, 680 and 360 km s^{-1}) viewed at inclinations projected assuming $b/a = \sin i$ (i.e. a circular disk).

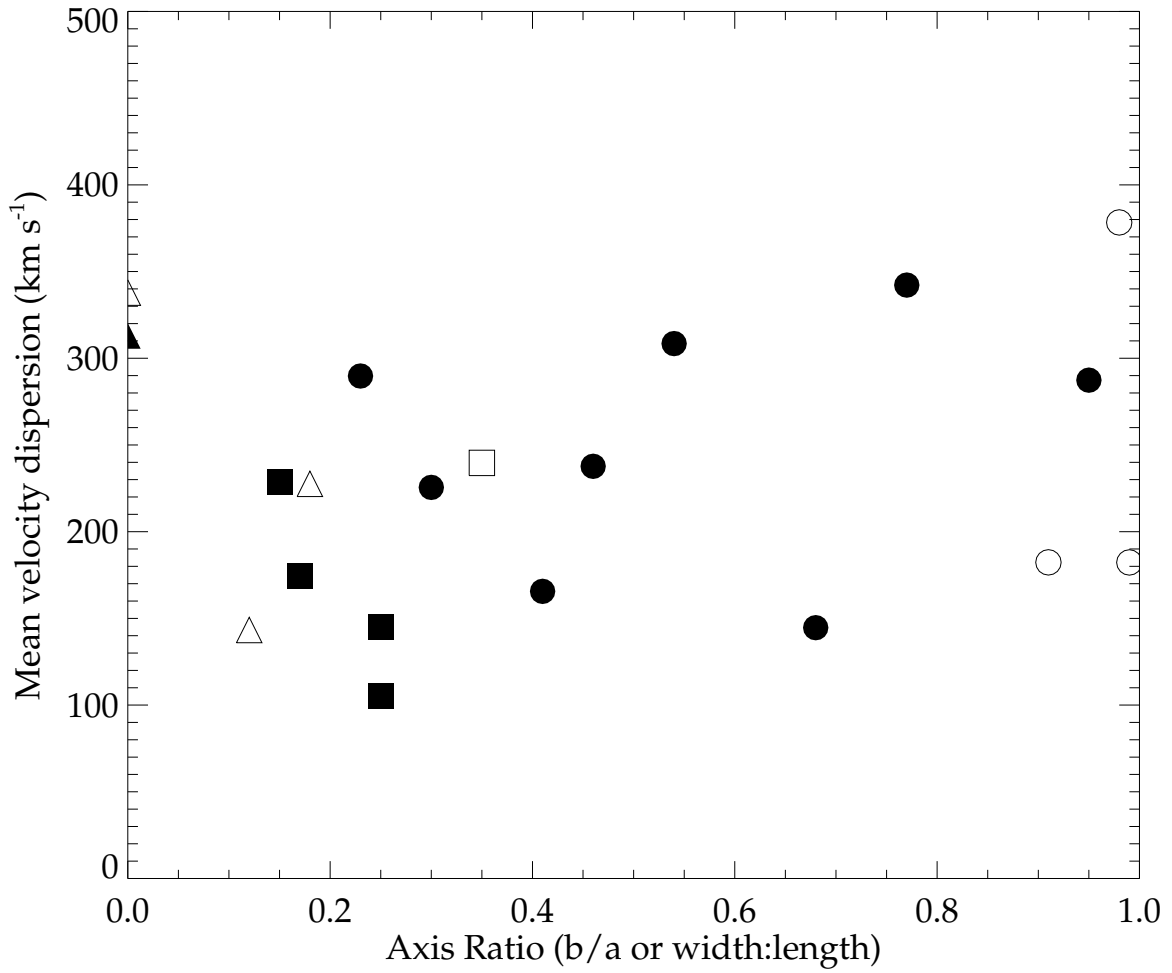


Fig. 25.— Mean gas velocity dispersion within 100 pc of the nucleus ($\overline{\sigma_{100\text{pc}}}$) as a function of dust disk axis ratio (b/a) or dust lane *width : length* ratio, which is an indicator of inclination. The different kinematic classes and dust morphologies are indicated. Filled symbols represent rotators: with dust disks (\bullet), with dust lanes (\blacksquare) or with irregular dust (\blacktriangle); Empty symbols represent non-rotators: with dust disks (\circ), with dust lanes (\square) or with no-dust or irregular dust (\triangle).

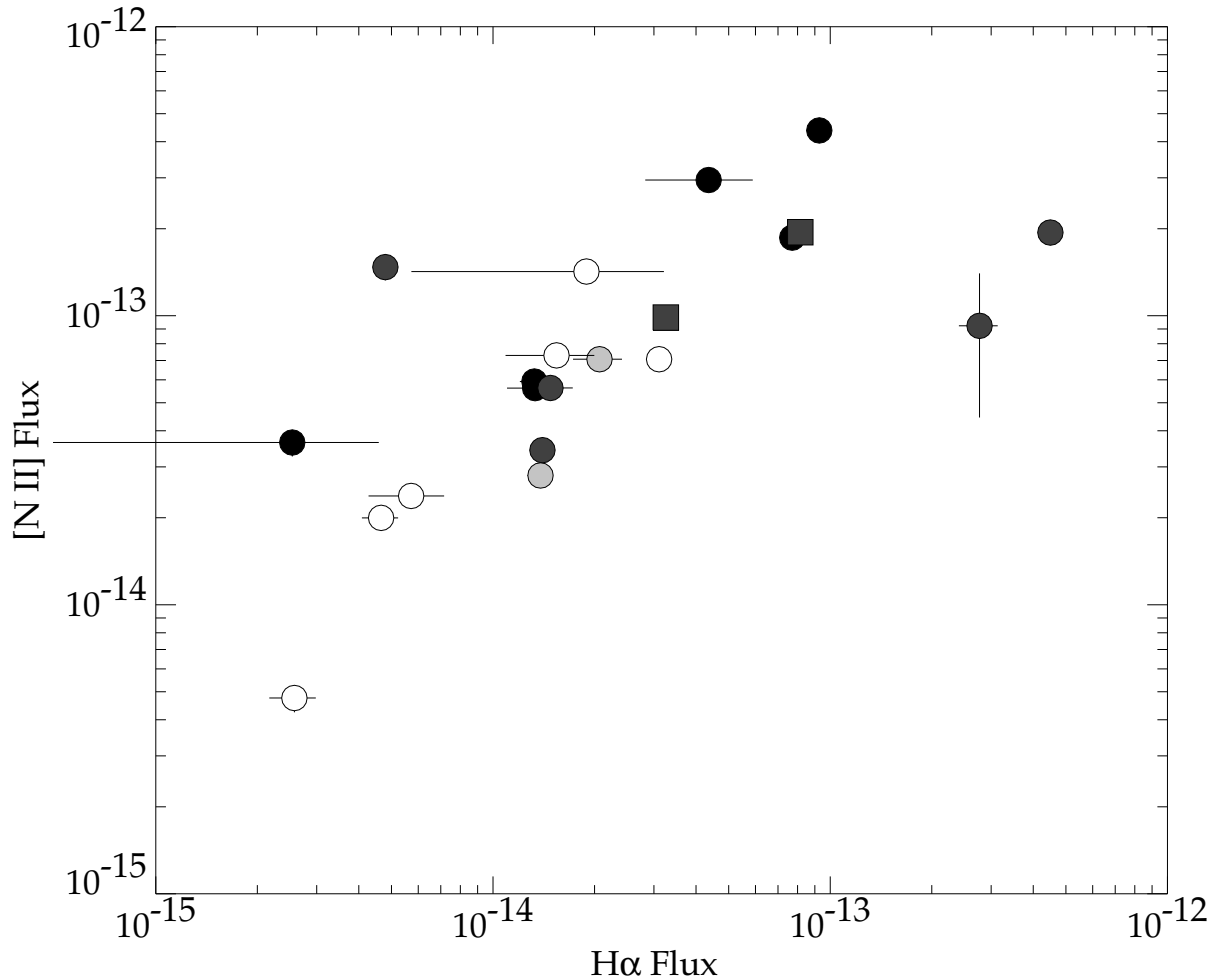


Fig. 26.— [N II] against H α fluxes for the UGC FR-I sample members. Formal errors in the fluxes are shown. The shading of the symbols indicates the score assigned to the broad component in each case (see text). A score of 3 (most confident) is shown by black symbols, through to white symbols for a score of zero (no confidence in a broad-line detection). It is possible to see a trend with flux from less to more confidence in broad-line detection.

Table 1. Properties of the galaxy sample members.

NGC (1)	UGC (2)	Other Names (3)	Type (4)	v_{sys} (km s $^{-1}$) (5)	STIS Scale (pc/pixel) (6)	M_B (mag) (7)	$\log(L_{1400})$ (W Hz $^{-1}$) (8)	Axis Ratio b/a (9)
193	408		E-S0	4342.5	15.0	-21.0	23.93	(0.18)
315	597		E	5092.5	17.6	-22.6	24.10	0.23
383	689	3C 31	E-S0	4890.0	16.9	-22.2	24.51	0.77
541	1004		E	5497.5	19.0	-21.7	23.94	0.91
741	1413		E	5265.0	18.2	-22.6	23.85	...
	1841	3C 66B	E	6360.0	22.0	-22.5	24.94	~ 0.98
2329	3695		E-S0	5725.0	19.8	-21.9	23.76	0.68
2892	5073		E	6810.0	23.6	-21.1	23.36	...
3801	6635		S0	3255.0	11.3	-20.8	23.49	(0.12)
3862	6723	3C 264	E	6330.0	21.9	-21.7	24.75	~ 0.99
	7115		E	6787.5	23.5	-21.0	23.94	~ 0.95
4261	7360	3C 270	E	2212.5	7.7	-21.5	24.40	0.46
4335	7455		E-S0	4672.5	16.2	-21.6	23.11	0.41
4374	7494	M84, 3C 272.1	S0	1155.0	4.0	-20.9	23.35	(0.15)
4486	7654	M87, 3C 274	E	1155.0	4.0	-22.2	24.90	...
5127	8419		E	4830.0	16.7	-21.3	24.08	(0.25)
5141	8433		S0	5302.5	18.4	-21.0	23.80	(0.25)
5490	9058		E	5790.0	20.1	-21.7	23.79	(0.35)
7052	11718		E	4155.0	14.4	-21.0	23.04	0.30
	12064	3C 449	E-S0	5122.5	17.7	-20.8	24.38	0.54
7626	12531		E	3495.0	12.1	-21.7	23.37	(0.17)

Note. — Col. (1): NGC number where available; Col. (2): *Upsalla General Catalog* (UGC) number; Col. (3): Alternative names; Col. (4): From the *NASA Extragalactic Database* (NED); Col. (5): Measured from the stellar kinematics (from NED); Col. (6): Parsecs per unbinned STIS pixel; Col. (7): Absolute blue magnitude from Condon & Broderick (1988); Col. (8): Radio Luminosity from Condon & Broderick (1988); Col. (9): Dust disk axis ratio from Verdoes Kleijn, et al. (1999), numbers in parentheses indicate a dust lane where the width:length ratio is given instead. All physical parameters assume $H_0 = 70 \text{ km s}^{-1} \text{Mpc}^{-1}$

Table 2. HST-STIS G750M observing log for this program.

Galaxy	Visit ID	Aperture	Offsets (")	Exposure times (seconds)	Brightest Row
(1)	(2)	(3)	(4)	(5)	(6)
NGC 193	o5ee01	52x0.2	-0.20, 0.00, +0.20	1700, 1300, 1560	300
NGC 315	o5ee02	52x0.1	-0.10, 0.00, +0.10	1082, 1000, 1098	598
NGC 383	o5ee03	52x0.1	-0.10, 0.00, +0.10	1082, 1000, 1098	599
NGC 541	o5ee04	52x0.2	-0.20, 0.00, +0.20	1442, 1300, 1500	300
NGC 741	o5ee05	52x0.2	-0.20, 0.00, +0.20	1667, 1145, 1500	300
UGC 1841	o5ee06	52x0.2	-0.20, 0.00, +0.20	1870, 1300, 1560	300
NGC 2329	o5ee07	52x0.2	-0.20, 0.00, +0.20	1967, 1245, 1560	300
NGC 2892	o5ee09	52x0.2	-0.20, 0.00, +0.20	2037, 1300, 1560	299
NGC 3801	o5ee10	52x0.2	-0.20, 0.00, +0.20	1699, 1292, 1560	305
NGC 3862	o5ee11	52x0.2	-0.20, 0.00, +0.20	900, 731, 1066	300
UGC 7115	o5ee22	52x0.2	0.00	2058	299
NGC 4261	o5ee12	52x0.1	-0.10, 0.00, +0.10	994, 1000, 1000	601
NGC 4335	o5ee13	52x0.2	-0.20, 0.00, +0.20	2154, 1300, 1560	300
NGC 4374	o3wn01	52x0.2	-0.20, 0.00, +0.20	2245, 2600, 2600	600
NGC 4486	o67z01/2	52x0.2	-0.20, 0.00, +0.20	1708, 1380, 1708	601
NGC 5127	o5ee15	52x0.2	-0.20, 0.00, +0.20	1660, 1000, 1500	303
NGC 5141	o5ee16	52x0.2	-0.20, 0.00, +0.20	1968, 1300, 1560	300
NGC 5490	o5ee17	52x0.2	-0.20, 0.00, +0.20	1590, 1300, 1560	299
NGC 7052	o5ee18	52x0.1	-0.10, 0.00, +0.10	1747, 1300, 1500	600
UGC 12064	o5ee20	52x0.1	-0.10, 0.00, +0.10	1532, 1000, 1500	599
NGC 7626	o5ee19	52x0.2	-0.20, 0.00, +0.20	1905, 1263, 1560	300

Note. — Col. (1): NGC/UGC Number; Col. (2): Root name for the HST visit and data sets; Col. (3): HST/STIS aperture used; Col. (4): Slit positions with offsets perpendicular to the slit direction, given relative to the central slit position. UGC 7115 was observed in only one position. Further data not included here is available for NGC 4374 (M84) and NGC 4486 (M87); Col. (5): Exposure times in each offset position. For each position two observations were obtained separated by 0''.2028 along the direction of the slit, the combined exposure time is shown; Col. (6): Row number in the final x2d file of the brightest row.

Table 3. HST/STIS Instrumental properties for the configurations used.

Grating	Aperture	Slit Width (")	Binning	Central λ (Å)	Wavelength Covered (Å ... Å)	λ Scale (Å/ pixel)	Spatial Scale (/ pixel)
(1)	(2)	(3)	(4)	(5)	(6)	(7)	(8)
G750M	52x0.1	0.1	2×1	6768	6482 ... 7054	1.108	0.05
G750M	52x0.2	0.2	2×2	6768	6482 ... 7054	1.108	0.1
G750M	52x0.2 (M84)	0.2	1×1	6581	6295 ... 6867	0.554	0.05
G750M	52x0.2 (M87)	0.2	1×1	6581	6295 ... 6867	0.554	0.05

Note. — Col. (1): HST/STIS Grating Used; Col. (2): HST/STIS Aperture Used; Col. (3): The slit width of the chosen aperture; Col. (4): The degree of on chip binning used given as `binaxis1`×`binaxis2` (wavelength by spatial binning); Col. (5): The set central wavelength; Col. (6): The minimum and maximum wavelengths on the CCD chip at that central wavelength position; Col. (7) The wavelength scale per binned pixel; Col. (8) The spatial scale per binned pixel. Further details of HST/STIS configurations can be found in Kimble, et al. (1998).

Table 4. Position angles of various axes.

Galaxy (1)	Major Axis (°N \leftrightarrow E) (2)	Radio Axis (°N \leftrightarrow E) (3)	Dust Axis (°N \leftrightarrow E) (4)	STIS Slits (°N \leftrightarrow E) (5)	Target (6)	ΔPA (°) (7)
NGC 193	58	104	0	57.9	M.Ax.	0.1
NGC 315	39	130	40	-143.8	M.Ax.	2.8
NGC 383	144	162	138	144.1	M.Ax.	0.1
NGC 541	143	76	...	-85.6
NGC 741	92	-107.4	M.Ax. [†]	19.4
UGC 1841	91	50	...	90.0	M.Ax.	1.0
NGC 2329	171	150	174	170.8	M.Ax.	0.2
NGC 2892	164	52	...	142.0	M.Ax. [†]	22.0
NGC 3801	121	121	24	121.1	M.Ax.	0.1
NGC 3862	25	30	...	122.3	\perp Jet	2.3
UGC 7115	91	116	175	-174.4	\perp Jet [†]	20.4
NGC 4261	155	87	163	157.9	M.Ax.	2.9
NGC 4335	156	82	158	-32.5	M.Ax.	8.5
NGC 4374	128	1	79	104.0	\perp Jet	13.0
NGC 4486	128	112	...	164.7
NGC 5127	68	118	48	68.0	M.Ax.	0.0
NGC 5141	65	12	88	71.9	M.Ax.	6.9
NGC 5490	1	75	143	-173.9	M.Ax.	5.1
NGC 7052	64	23	65	63.6	M.Ax.	0.4
UGC 12064	39	11	171	170.6	Dust	0.4
NGC 7626	171	44	167	170.8	M.Ax.	0.2

Note. — Col. (1): NGC/UGC Name; Col. (2): Position angles of the major axes just outside the central dust distributions; Col. (3): Position angles of the radio jet axes on arcsecond scales or smaller; Col. (4): Position angles of the central dust distributions; Col. (5): Position angles of the STIS slits on the nucleus; Col. (6): The target orientation of the STIS slits (|| M.Ax.: Parallel to the Major Axis; || Dust: Parallel to the Dust Axis; \perp Jet: Perpendicular to the radio jet; [†] Additional flexibility allowed to reduce scheduling constraints); Col. (7): Offset in degrees of the STIS slits from the target orientation.

References. — Data for Columns 3 - 5 taken from Verdoes Kleijn, et al. (1999)

Table 5. Spectral Lines in the region of H α .

Ion	Ref.	Transition	λ_{air}	λ_{vac}
			(\AA)	(\AA)
(1)	(2)	(3)	(4)	(5)
[N II]	(a)	${}^3\text{P}_1 - {}^1\text{D}_2$	6548.05	6549.86
H α	(b)		6562.80	6564.61
[N II]	(a)	${}^3\text{P}_2 - {}^1\text{D}_2$	6583.39	6585.21
[S II]	(a)	${}^4\text{S}_{3/2} - {}^2\text{D}_{5/2}$	6716.44	6718.29
[S II]	(a)	${}^4\text{S}_{3/2} - {}^2\text{D}_{3/2}$	6730.81	6732.67

Note. — Col. (1): Ion responsible for the line; Col. (2): Wavelength reference; Col. (3): Transition configuration terms; Col. (4): Air wavelength; Col. (5): Vacuum wavelength. Note that the value for H α is computed from the intensity weighted mean of fine structure lines at $\lambda_{\text{air}} = 6562.7247$ and $\lambda_{\text{air}} = 6562.8516$ with relative intensities of 120 and 180 respectively.

References. — (a) Wallerstein, et al. (2001);
 (b) Reader & Corliss (1998)

Table 6. NGC 193: Measured Parameters.

Row	Y-Offset (")	v_r (km s $^{-1}$)	σ_{gas} (km s $^{-1}$)	F(H α /10 $^{-16}$) (erg s $^{-1}$ cm $^{-2}$ Hz $^{-1}$)	$\frac{F(N\text{ II}_{6585})}{F(H\alpha)}$	$\frac{F(S\text{ II}_{total})}{F(H\alpha)}$	R^2
Slit 1: X-Offset -0.2"							
2	-0.9128	4334 ± 30	135 ± 30	6.6 ± 2.9	1.7 ± 0.9	1.2 ± 0.7	3.79
3	-0.8114	4270 ± 30	121 ± 32	6.9 ± 3.3	1.5 ± 1.0	0.2 ± 0.3	3.17
4	-0.7099	4323 ± 22	124 ± 23	10.6 ± 4.0	1.5 ± 0.7	0.1 ± 0.2	3.90
5	-0.6085	4390 ± 7	40 ± 7	7.8 ± 2.3	1.4 ± 0.6	0.1 ± 0.2	3.23
6	-0.5071	4602 ± 42	233 ± 41	12.9 ± 4.5	0.0 ± 0.3	1.8 ± 0.8	2.83
7	-0.4057	4371 ± 10	67 ± 10	7.4 ± 2.3	1.5 ± 0.6	1.2 ± 0.5	3.67
8	-0.3043	4402 ± 9	48 ± 9	6.2 ± 2.2	1.1 ± 0.5	0.9 ± 0.5	3.46
9	-0.2028	4369 ± 23	210 ± 18	24.7 ± 4.4	1.2 ± 0.3	1.3 ± 0.3	3.28
10	-0.1014	4344 ± 9	132 ± 9	12.5 ± 2.8	2.9 ± 0.7	3.0 ± 0.7	3.49
11	0.0000	4336 ± 7	121 ± 7	18.3 ± 2.8	2.8 ± 0.5	2.2 ± 0.4	3.66
12	0.1014	4340 ± 8	128 ± 8	18.6 ± 2.9	2.7 ± 0.5	1.6 ± 0.3	3.50
13	0.2028	4374 ± 6	85 ± 6	18.0 ± 2.7	1.8 ± 0.3	1.1 ± 0.2	3.11
14	0.3043	4343 ± 7	86 ± 7	19.2 ± 3.1	1.3 ± 0.3	1.0 ± 0.2	2.77
15	0.4057	4298 ± 14	97 ± 14	8.0 ± 2.6	2.6 ± 1.0	0.2 ± 0.3	2.52
16	0.5071	4309 ± 10	64 ± 10	8.0 ± 2.3	1.5 ± 0.6	1.0 ± 0.4	3.05
17	0.6085	4303 ± 8	66 ± 8	9.9 ± 2.3	1.7 ± 0.5	0.9 ± 0.3	2.96
18	0.7099	4317 ± 6	47 ± 6	13.3 ± 2.7	0.5 ± 0.2	0.6 ± 0.2	2.95
19	0.8114	4331 ± 8	45 ± 7	10.8 ± 2.9	0.6 ± 0.3	0.2 ± 0.1	3.50
20	0.9128	4390 ± 31	169 ± 29	5.7 ± 3.1	3.2 ± 1.9	1.6 ± 1.1	3.42

Table 6—Continued

Row	Y-Offset (")	v_r (km s $^{-1}$)	σ_{gas} (km s $^{-1}$)	F(H α /10 $^{-16}$) (erg s $^{-1}$ cm $^{-2}$ Hz $^{-1}$)	$\frac{F(\text{N II}_{6585})}{F(\text{H}\alpha)}$	$\frac{F(\text{S II}_{total})}{F(\text{H}\alpha)}$	R^2
Slit 0: X-Offset 0.0"							
1	-1.0142	4425 ± 41	164 ± 38	7.2 ± 4.0	2.5 ± 1.6	0.4 ± 0.5	2.62
4	-0.7099	4336 ± 10	75 ± 10	10.5 ± 3.1	1.9 ± 0.7	0.8 ± 0.4	2.41
5	-0.6085	4353 ± 10	96 ± 10	13.4 ± 3.1	1.9 ± 0.5	1.4 ± 0.4	2.58
6	-0.5071	4345 ± 18	163 ± 17	22.8 ± 4.5	1.2 ± 0.3	1.0 ± 0.3	2.81
7	-0.4057	4391 ± 22	178 ± 18	22.4 ± 4.7	1.0 ± 0.3	1.7 ± 0.4	2.86
8	-0.3043	4331 ± 39	223 ± 31	17.3 ± 4.9	1.4 ± 0.5	1.6 ± 0.6	2.78
9	-0.2028	4551 ± 15	274 ± 12	54.9 ± 6.3	2.3 ± 0.3	2.1 ± 0.3	2.61
10	-0.1014	4560 ± 10	444 ± 9	205.9 ± 13.8	3.2 ± 0.2	2.0 ± 0.2	3.16
11	0.0000	4481 ± 7	437 ± 6	316.4 ± 16.3	3.5 ± 0.2	1.8 ± 0.1	3.89
12	0.1014	4308 ± 5	178 ± 4	74.1 ± 5.0	2.5 ± 0.2	1.6 ± 0.1	2.87
13	0.2028	4339 ± 10	135 ± 9	16.0 ± 3.4	2.2 ± 0.6	3.4 ± 0.8	2.33
14	0.3043	4323 ± 12	109 ± 11	10.1 ± 3.0	2.1 ± 0.8	3.5 ± 1.2	2.67
15	0.4057	4336 ± 9	51 ± 8	11.2 ± 3.0	0.9 ± 0.4	0.3 ± 0.2	2.50
16	0.5071	4288 ± 26	159 ± 25	17.0 ± 4.4	1.0 ± 0.4	0.9 ± 0.4	2.88
17	0.6085	4314 ± 25	137 ± 24	7.9 ± 3.3	2.4 ± 1.2	1.9 ± 1.0	2.97
18	0.7099	4331 ± 15	80 ± 16	11.4 ± 3.6	1.0 ± 0.5	0.3 ± 0.2	2.90
20	0.9128	4110 ± 28	158 ± 24	11.4 ± 3.5	0.1 ± 0.3	2.3 ± 0.9	2.96
21	1.0142	4483 ± 39	200 ± 33	8.7 ± 3.8	3.0 ± 1.5	0.7 ± 0.6	2.86

Table 6—Continued

Row	Y-Offset (")	v_r (km s $^{-1}$)	σ_{gas} (km s $^{-1}$)	F(H α /10 $^{-16}$) (erg s $^{-1}$ cm $^{-2}$ Hz $^{-1}$)	$\frac{F(N\text{ II}_{6585})}{F(H\alpha)}$	$\frac{F(S\text{ II}_{total})}{F(H\alpha)}$	R^2
Slit 2: X-Offset +0.2"							
1	-1.0142	4366 ± 10	75 ± 9	11.1 ± 2.7	1.4 ± 0.4	0.4 ± 0.2	3.19
2	-0.9128	4380 ± 10	80 ± 10	8.5 ± 2.4	1.8 ± 0.6	1.1 ± 0.4	3.07
7	-0.4057	4450 ± 13	101 ± 13	4.6 ± 2.5	3.5 ± 2.0	3.7 ± 2.1	2.81
8	-0.3043	4466 ± 9	84 ± 9	4.2 ± 2.2	4.2 ± 2.3	5.0 ± 2.7	2.91
9	-0.2028	4449 ± 11	91 ± 11	6.7 ± 2.4	2.1 ± 0.9	3.0 ± 1.2	2.83
10	-0.1014	4453 ± 7	84 ± 7	9.6 ± 2.6	3.3 ± 1.0	1.8 ± 0.6	2.91
11	0.0000	4433 ± 7	87 ± 7	9.3 ± 2.6	3.8 ± 1.2	2.4 ± 0.7	2.78
12	0.1014	4385 ± 7	77 ± 7	10.8 ± 2.5	2.5 ± 0.7	1.4 ± 0.4	2.67
13	0.2028	4386 ± 14	131 ± 15	5.2 ± 2.7	6.5 ± 3.5	1.9 ± 1.1	2.56
14	0.3043	4411 ± 8	61 ± 8	8.3 ± 2.3	1.7 ± 0.6	1.3 ± 0.5	2.61
15	0.4057	4421 ± 20	107 ± 19	10.6 ± 3.5	1.1 ± 0.5	0.9 ± 0.4	2.66
16	0.5071	4342 ± 22	83 ± 23	6.1 ± 2.8	1.1 ± 0.7	1.1 ± 0.7	2.77
17	0.6085	4413 ± 44	114 ± 44	3.7 ± 2.8	2.2 ± 2.0	0.4 ± 0.7	2.96
21	1.0142	4112 ± 35	130 ± 34	5.6 ± 2.8	0.1 ± 0.4	2.0 ± 1.2	3.34

Table 7. NGC 315: Measured Parameters.

Row	Y-Offset (")	v_r (km s $^{-1}$)	σ_{gas} (km s $^{-1}$)	F(H α /10 $^{-16}$) (erg s $^{-1}$ cm $^{-2}$ Hz $^{-1}$)	$\frac{F(\text{N II}_{6585})}{F(\text{H}\alpha)}$	$\frac{F(\text{S II}_{total})}{F(\text{H}\alpha)}$	R^2
Slit 1: X-Offset -0.1"							
1	-0.5071	4827 ± 22	70 ± 21	39.1 ± 17.8	0.0 ± 0.3	0.5 ± 0.4	1.67
7	-0.2028	4884 ± 34	161 ± 31	52.2 ± 19.8	1.2 ± 0.6	1.2 ± 0.6	1.90
8	-0.1521	4943 ± 33	175 ± 29	33.0 ± 17.3	3.0 ± 1.7	2.7 ± 1.6	1.93
9	-0.1014	4866 ± 32	193 ± 27	62.0 ± 19.8	2.4 ± 0.9	1.0 ± 0.4	1.65
10	-0.0507	4905 ± 37	272 ± 32	88.4 ± 25.3	2.4 ± 0.8	0.9 ± 0.4	1.84
11	0.0000	4917 ± 28	302 ± 24	151.2 ± 29.4	2.5 ± 0.6	1.3 ± 0.3	1.83
12	0.0507	4814 ± 48	485 ± 44	60.7 ± 45.0	8.3 ± 6.3	3.0 ± 2.3	1.90
13	0.1014	4882 ± 36	337 ± 35	61.7 ± 28.1	5.4 ± 2.6	2.2 ± 1.1	1.88
14	0.1521	5041 ± 8	65 ± 8	55.6 ± 13.8	1.6 ± 0.5	0.9 ± 0.3	1.64
15	0.2028	5036 ± 14	66 ± 13	42.2 ± 15.7	1.3 ± 0.6	0.5 ± 0.3	1.51
16	0.2535	5079 ± 17	79 ± 17	45.6 ± 17.0	1.2 ± 0.6	0.5 ± 0.3	1.45
17	0.3043	5069 ± 12	59 ± 11	65.0 ± 19.4	0.1 ± 0.2	0.6 ± 0.3	1.68
18	0.3550	5053 ± 8	43 ± 7	25.4 ± 9.9	0.5 ± 0.4	2.1 ± 1.0	1.46
20	0.4564	5283 ± 11	42 ± 11	18.7 ± 10.4	0.4 ± 0.5	1.6 ± 1.1	1.28
Slit 0: X-Offset 0.0"							
1	-0.5071	4880 ± 43	174 ± 40	58.9 ± 22.8	0.9 ± 0.5	0.7 ± 0.4	1.36
2	-0.4564	4800 ± 31	160 ± 29	98.9 ± 26.6	0.7 ± 0.3	0.1 ± 0.2	1.65

Table 7—Continued

Row	Y-Offset (")	v_r (km s $^{-1}$)	σ_{gas} (km s $^{-1}$)	F(H α /10 $^{-16}$) (erg s $^{-1}$ cm $^{-2}$ Hz $^{-1}$)	$\frac{F(N\text{ II}_{6585})}{F(H\alpha)}$	$\frac{F(S\text{ II}_{total})}{F(H\alpha)}$	R^2
4	-0.3550	4860 ± 38	166 ± 36	63.5 ± 22.0	1.2 ± 0.6	0.4 ± 0.3	1.55
5	-0.3043	4853 ± 30	183 ± 27	96.9 ± 23.9	1.1 ± 0.4	0.6 ± 0.3	1.47
6	-0.2535	4878 ± 26	206 ± 22	90.1 ± 21.7	1.8 ± 0.5	1.5 ± 0.4	1.62
7	-0.2028	4915 ± 18	162 ± 16	72.1 ± 17.8	2.0 ± 0.6	2.1 ± 0.6	1.63
8	-0.1521	4921 ± 26	263 ± 19	228.1 ± 29.8	1.3 ± 0.2	0.9 ± 0.2	1.38
9	-0.1014	4873 ± 19	347 ± 16	442.4 ± 43.7	2.1 ± 0.2	0.9 ± 0.1	1.79
10	-0.0507	4824 ± 9	354 ± 8	992.3 ± 53.0	2.2 ± 0.1	1.1 ± 0.1	2.39
11	0.0000	4835 ± 9	528 ± 7	899.0 ± 108.2	7.1 ± 0.9	1.8 ± 0.2	3.84
12	0.0507	4906 ± 9	457 ± 8	1314.6 ± 83.9	3.6 ± 0.2	0.9 ± 0.1	2.94
13	0.1014	4819 ± 28	438 ± 26	479.8 ± 62.2	1.9 ± 0.3	0.7 ± 0.1	1.89
14	0.1521	5124 ± 22	204 ± 18	156.1 ± 26.6	1.3 ± 0.3	0.8 ± 0.2	1.37
15	0.2028	5172 ± 33	172 ± 29	81.8 ± 22.6	0.9 ± 0.4	0.9 ± 0.4	1.74
17	0.3043	4957 ± 38	213 ± 29	117.9 ± 25.8	0.8 ± 0.3	0.7 ± 0.2	1.84
19	0.4057	5218 ± 14	60 ± 14	47.4 ± 16.3	0.7 ± 0.4	0.4 ± 0.3	1.49
20	0.4564	5060 ± 24	102 ± 24	60.6 ± 20.9	0.0 ± 0.2	0.6 ± 0.3	1.58
21	0.5071	5185 ± 8	39 ± 8	15.8 ± 8.5	1.1 ± 0.9	2.8 ± 1.7	1.78
Slit 2: X-Offset +0.1"							
3	-0.4057	4971 ± 26	164 ± 24	97.2 ± 22.4	0.8 ± 0.3	0.3 ± 0.2	1.60
4	-0.3550	4889 ± 22	154 ± 20	72.4 ± 17.4	1.2 ± 0.4	1.2 ± 0.4	1.67
5	-0.3043	4868 ± 18	169 ± 16	66.0 ± 16.7	2.5 ± 0.7	1.8 ± 0.5	1.67

Table 7—Continued

Row	Y-Offset (")	v_r (km s $^{-1}$)	σ_{gas} (km s $^{-1}$)	F(H α /10 $^{-16}$) (erg s $^{-1}$ cm $^{-2}$ Hz $^{-1}$)	$\frac{F(N\text{ II}_{6585})}{F(H\alpha)}$	$\frac{F(S\text{ II}_{total})}{F(H\alpha)}$	R^2
6	-0.2535	4977 ± 12	136 ± 11	61.9 ± 14.8	3.0 ± 0.8	1.8 ± 0.5	1.83
7	-0.2028	4956 ± 16	222 ± 13	143.8 ± 20.6	2.1 ± 0.4	1.4 ± 0.3	1.69
8	-0.1521	4944 ± 11	208 ± 9	145.5 ± 18.8	3.2 ± 0.5	2.0 ± 0.3	1.56
9	-0.1014	4897 ± 7	214 ± 5	320.3 ± 22.0	2.6 ± 0.2	1.5 ± 0.1	1.96
10	-0.0507	4880 ± 5	239 ± 4	597.9 ± 27.9	2.8 ± 0.2	1.4 ± 0.1	1.99
11	0.0000	4883 ± 4	251 ± 3	712.0 ± 30.2	3.2 ± 0.2	1.4 ± 0.1	1.90
12	0.0507	4953 ± 6	263 ± 4	657.0 ± 31.9	3.0 ± 0.2	1.2 ± 0.1	2.04
13	0.1014	4984 ± 8	242 ± 6	378.2 ± 26.5	2.9 ± 0.2	1.1 ± 0.1	2.30
14	0.1521	5021 ± 17	244 ± 13	198.5 ± 24.1	2.3 ± 0.3	1.2 ± 0.2	1.54
15	0.2028	5014 ± 43	273 ± 33	136.9 ± 28.1	1.2 ± 0.3	0.9 ± 0.3	1.68
17	0.3043	5097 ± 35	191 ± 30	49.1 ± 17.4	2.3 ± 1.0	1.0 ± 0.5	1.70
18	0.3550	5165 ± 45	190 ± 40	65.0 ± 21.8	0.8 ± 0.4	0.7 ± 0.4	1.94
19	0.4057	5256 ± 40	218 ± 31	108.3 ± 26.6	0.9 ± 0.3	0.4 ± 0.2	1.56
20	0.4564	5313 ± 50	222 ± 45	97.2 ± 30.9	0.4 ± 0.3	0.5 ± 0.3	1.71
21	0.5071	5169 ± 41	190 ± 35	63.9 ± 20.5	1.6 ± 0.7	0.1 ± 0.3	1.76

Table 8. NGC 383: Measured Parameters.

Row	Y-Offset (")	v_r (km s $^{-1}$)	σ_{gas} (km s $^{-1}$)	F(H α /10 $^{-16}$) (erg s $^{-1}$ cm $^{-2}$ Hz $^{-1}$)	$\frac{F(\text{N II}_{6585})}{F(\text{H}\alpha)}$	$\frac{F(\text{S II}_{total})}{F(\text{H}\alpha)}$	R^2
Slit 1: X-Offset -0.1"							
2	-0.4564	4953 ± 7	37 ± 7	9.5 ± 5.5	3.4 ± 2.2	3.6 ± 2.4	1.40
3	-0.4057	4880 ± 21	105 ± 21	21.6 ± 10.0	2.4 ± 1.3	1.6 ± 1.1	1.58
4	-0.3550	4923 ± 41	184 ± 38	29.1 ± 13.5	2.4 ± 1.3	0.1 ± 0.7	1.62
5	-0.3043	4915 ± 30	163 ± 28	42.5 ± 14.2	1.9 ± 0.8	0.1 ± 0.4	1.86
6	-0.2535	4952 ± 24	201 ± 20	95.3 ± 17.3	1.3 ± 0.3	0.6 ± 0.3	1.91
7	-0.2028	4945 ± 18	205 ± 15	116.8 ± 16.9	1.5 ± 0.3	1.1 ± 0.3	1.48
8	-0.1521	4957 ± 13	173 ± 11	112.3 ± 14.9	1.7 ± 0.3	1.0 ± 0.2	1.68
9	-0.1014	5046 ± 16	248 ± 12	156.8 ± 18.2	2.1 ± 0.3	0.9 ± 0.2	1.64
10	-0.0507	5086 ± 11	269 ± 9	235.4 ± 20.0	2.6 ± 0.3	1.3 ± 0.2	1.65
11	0.0000	5135 ± 7	235 ± 5	274.4 ± 18.7	3.1 ± 0.2	1.3 ± 0.1	1.90
12	0.0507	5186 ± 7	223 ± 5	275.3 ± 18.6	2.7 ± 0.2	1.0 ± 0.1	2.04
13	0.1014	5201 ± 13	239 ± 10	157.2 ± 17.6	2.6 ± 0.3	1.0 ± 0.2	1.48
14	0.1521	5263 ± 40	306 ± 35	64.9 ± 20.0	3.1 ± 1.1	0.5 ± 0.5	1.34
17	0.3043	5166 ± 40	126 ± 40	31.0 ± 14.3	0.8 ± 0.6	0.6 ± 0.7	1.76
18	0.3550	5216 ± 25	87 ± 25	26.6 ± 11.7	0.3 ± 0.3	1.6 ± 1.0	1.58
20	0.4564	4457 ± 30	137 ± 29	40.8 ± 14.6	1.2 ± 0.6	0.4 ± 0.5	1.60
21	0.5071	5285 ± 7	37 ± 7	33.6 ± 9.2	0.4 ± 0.2	0.5 ± 0.3	1.70

Slit 0: X-Offset 0.0"

Table 8—Continued

Row	Y-Offset (")	v_r (km s $^{-1}$)	σ_{gas} (km s $^{-1}$)	F(H α /10 $^{-16}$) (erg s $^{-1}$ cm $^{-2}$ Hz $^{-1}$)	$\frac{F(N\text{ II}_{6585})}{F(H\alpha)}$	$\frac{F(S\text{ II}_{total})}{F(H\alpha)}$	R^2
1	-0.5071	4909 ± 19	94 ± 19	55.7 ± 18.5	0.8 ± 0.4	0.3 ± 0.3	1.68
2	-0.4564	4750 ± 33	140 ± 32	49.6 ± 18.0	1.0 ± 0.5	0.5 ± 0.5	1.68
3	-0.4057	4796 ± 16	93 ± 15	57.9 ± 15.5	1.0 ± 0.4	0.8 ± 0.4	1.72
4	-0.3550	4905 ± 41	212 ± 33	70.8 ± 21.1	1.4 ± 0.5	0.2 ± 0.4	1.71
5	-0.3043	4987 ± 24	149 ± 23	59.9 ± 17.9	1.6 ± 0.6	0.2 ± 0.4	1.56
6	-0.2535	4873 ± 24	213 ± 23	36.6 ± 16.8	5.0 ± 2.4	2.4 ± 1.4	1.76
7	-0.2028	4865 ± 11	182 ± 10	140.6 ± 18.8	2.2 ± 0.4	0.6 ± 0.2	1.89
8	-0.1521	4874 ± 15	319 ± 14	263.4 ± 29.6	2.7 ± 0.3	1.0 ± 0.2	2.08
9	-0.1014	4939 ± 16	464 ± 15	501.0 ± 54.0	3.1 ± 0.4	1.1 ± 0.2	2.17
10	-0.0507	4924 ± 21	798 ± 13	359.0 ± 186.5	13.3 ± 6.9	3.8 ± 2.0	2.99
11	0.0000	5266 ± 44	924 ± 28	5274.1 ± 587.9	0.6 ± 0.1	0.3 ± 0.1	2.68
13	0.1014	5258 ± 16	311 ± 15	181.2 ± 28.0	3.1 ± 0.5	0.7 ± 0.2	1.83
14	0.1521	5299 ± 29	288 ± 29	40.4 ± 22.6	5.9 ± 3.4	0.4 ± 0.8	1.80
15	0.2028	5188 ± 27	159 ± 26	46.7 ± 18.3	2.1 ± 0.9	0.2 ± 0.5	1.69
18	0.3550	4537 ± 57	265 ± 44	67.6 ± 22.3	1.7 ± 0.7	0.5 ± 0.5	1.47
19	0.4057	5193 ± 24	135 ± 24	58.6 ± 18.6	1.2 ± 0.5	0.4 ± 0.4	1.53
20	0.4564	5239 ± 22	108 ± 21	23.9 ± 13.3	2.8 ± 1.7	0.6 ± 0.9	1.76
21	0.5071	5069 ± 11	38 ± 10	22.4 ± 10.1	0.5 ± 0.4	1.5 ± 1.0	1.36

Slit 2: X-Offset +0.1"

Table 8—Continued

Row	Y-Offset (")	v_r (km s $^{-1}$)	σ_{gas} (km s $^{-1}$)	F(H α /10 $^{-16}$) (erg s $^{-1}$ cm $^{-2}$ Hz $^{-1}$)	$\frac{F(N\text{ II}_{6585})}{F(H\alpha)}$	$\frac{F(S\text{ II}_{total})}{F(H\alpha)}$	R^2
1	-0.5071	4871 ± 8	39 ± 7	45.1 ± 13.5	0.4 ± 0.2	0.2 ± 0.2	1.48
2	-0.4564	4865 ± 18	89 ± 18	38.1 ± 12.8	1.4 ± 0.6	0.2 ± 0.4	1.74
4	-0.3550	4855 ± 12	54 ± 12	26.0 ± 10.1	1.5 ± 0.8	0.1 ± 0.5	2.26
5	-0.3043	4813 ± 16	79 ± 16	48.2 ± 15.6	0.7 ± 0.4	0.4 ± 0.3	1.77
6	-0.2535	4777 ± 8	64 ± 8	53.1 ± 11.6	1.3 ± 0.4	0.6 ± 0.3	1.97
7	-0.2028	4813 ± 8	105 ± 8	40.0 ± 10.5	5.2 ± 1.5	1.4 ± 0.6	1.79
8	-0.1521	4857 ± 9	145 ± 9	98.8 ± 14.3	2.6 ± 0.5	1.2 ± 0.3	1.91
9	-0.1014	4922 ± 20	289 ± 17	203.9 ± 24.9	2.0 ± 0.3	1.1 ± 0.2	1.67
10	-0.0507	4967 ± 11	257 ± 8	333.5 ± 25.0	2.0 ± 0.2	0.6 ± 0.1	1.76
11	0.0000	5083 ± 22	406 ± 21	290.3 ± 38.2	2.4 ± 0.4	0.9 ± 0.2	1.53
12	0.0507	5169 ± 35	420 ± 34	245.2 ± 42.5	1.8 ± 0.4	0.7 ± 0.2	1.82
13	0.1014	5229 ± 19	190 ± 18	69.8 ± 16.8	2.6 ± 0.7	0.8 ± 0.4	1.65
18	0.3550	4761 ± 16	64 ± 15	34.8 ± 12.3	0.0 ± 0.3	0.9 ± 0.6	1.75
19	0.4057	5278 ± 23	82 ± 23	15.8 ± 10.7	2.4 ± 1.9	1.4 ± 1.5	1.66
20	0.4564	5122 ± 47	179 ± 43	28.2 ± 15.5	2.2 ± 1.4	1.5 ± 1.3	1.84
21	0.5071	5260 ± 11	59 ± 11	40.4 ± 12.3	1.0 ± 0.4	0.1 ± 0.3	1.81

Table 9. NGC 541: Measured Parameters.

Table 9—Continued

Row	Y-Offset (")	v_r (km s $^{-1}$)	σ_{gas} (km s $^{-1}$)	F(H α /10 $^{-16}$) (erg s $^{-1}$ cm $^{-2}$ Hz $^{-1}$)	$\frac{F(N\text{ II}_{6585})}{F(H\alpha)}$	$\frac{F(S\text{ II}_{total})}{F(H\alpha)}$	R^2
5	-0.6085	5485 ± 7	45 ± 6	17.6 ± 3.7	0.3 ± 0.1	0.2 ± 0.1	2.10
6	-0.5071	5498 ± 5	43 ± 4	25.2 ± 4.1	0.1 ± 0.1	0.1 ± 0.1	2.59
7	-0.4057	5471 ± 5	29 ± 4	13.4 ± 3.0	0.6 ± 0.2	0.1 ± 0.1	2.98
9	-0.2028	5406 ± 24	163 ± 22	13.0 ± 4.3	2.2 ± 0.9	2.1 ± 0.8	2.26
10	-0.1014	5597 ± 23	362 ± 21	78.5 ± 11.2	2.6 ± 0.4	1.0 ± 0.2	2.78
11	0.0000	5459 ± 16	336 ± 13	138.3 ± 11.7	2.0 ± 0.2	0.4 ± 0.1	2.44
12	0.1014	5402 ± 23	164 ± 21	21.6 ± 5.2	1.7 ± 0.5	0.3 ± 0.2	2.54
13	0.2028	5331 ± 8	38 ± 8	8.7 ± 2.8	0.7 ± 0.3	0.7 ± 0.4	2.60
14	0.3043	5377 ± 8	55 ± 7	14.5 ± 3.2	0.9 ± 0.3	0.6 ± 0.2	2.73
15	0.4057	5372 ± 3	36 ± 3	26.1 ± 3.5	0.4 ± 0.1	0.3 ± 0.1	2.54
16	0.5071	5360 ± 8	77 ± 8	27.2 ± 4.4	0.3 ± 0.1	0.5 ± 0.1	2.51
17	0.6085	5250 ± 32	117 ± 31	4.5 ± 2.9	0.7 ± 0.8	3.1 ± 2.3	2.28
20	0.9128	5411 ± 14	47 ± 14	5.5 ± 2.6	0.1 ± 0.3	0.9 ± 0.7	2.62
Slit 2: X-Offset +0.2"							
1	-1.0142	5503 ± 24	84 ± 22	8.2 ± 3.4	0.8 ± 0.5	0.5 ± 0.4	3.02
2	-0.9128	5039 ± 38	160 ± 36	8.9 ± 3.7	0.2 ± 0.3	1.4 ± 0.8	2.87
6	-0.5071	5484 ± 8	73 ± 8	20.5 ± 3.6	0.5 ± 0.2	0.6 ± 0.2	3.47
7	-0.4057	5382 ± 11	107 ± 11	33.3 ± 5.0	0.2 ± 0.1	0.4 ± 0.1	3.15
8	-0.3043	5428 ± 11	108 ± 11	27.5 ± 4.5	0.9 ± 0.2	0.2 ± 0.1	2.56

Table 9—Continued

Row	Y-Offset (")	v_r (km s $^{-1}$)	σ_{gas} (km s $^{-1}$)	F(H α /10 $^{-16}$) (erg s $^{-1}$ cm $^{-2}$ Hz $^{-1}$)	$\frac{F(\text{N II}_{6585})}{F(\text{H}\alpha)}$	$\frac{F(\text{S II}_{total})}{F(\text{H}\alpha)}$	R^2
9	-0.2028	5383 ± 9	68 ± 8	14.0 ± 3.1	1.2 ± 0.4	0.9 ± 0.3	2.62
10	-0.1014	5371 ± 17	110 ± 17	16.4 ± 4.0	0.9 ± 0.3	1.0 ± 0.3	2.34
11	0.0000	5410 ± 20	106 ± 20	19.5 ± 5.4	0.1 ± 0.2	0.6 ± 0.2	2.79
12	0.1014	5292 ± 17	117 ± 17	19.6 ± 4.5	1.1 ± 0.3	0.2 ± 0.2	2.62
13	0.2028	5312 ± 3	27 ± 4	16.1 ± 3.8	0.5 ± 0.2	0.3 ± 0.1	2.63
14	0.3043	5324 ± 5	49 ± 5	20.2 ± 3.4	0.5 ± 0.1	0.3 ± 0.1	2.89
15	0.4057	5330 ± 6	55 ± 5	19.9 ± 3.1	0.5 ± 0.1	0.5 ± 0.1	2.85
16	0.5071	5346 ± 6	54 ± 5	22.0 ± 3.5	0.2 ± 0.1	0.3 ± 0.1	2.85
17	0.6085	5343 ± 6	42 ± 6	12.9 ± 2.9	0.1 ± 0.1	0.4 ± 0.2	2.60
19	0.8114	5275 ± 20	75 ± 19	9.2 ± 3.3	0.0 ± 0.2	0.4 ± 0.3	2.60
20	0.9128	4453 ± 26	144 ± 24	11.4 ± 3.0	0.1 ± 0.2	1.4 ± 0.5	2.37

Table 10. NGC 741: Measured Parameters.

Table 10—Continued

Row	Y-Offset (")	v_r (km s $^{-1}$)	σ_{gas} (km s $^{-1}$)	F(H α /10 $^{-16}$) (erg s $^{-1}$ cm $^{-2}$ Hz $^{-1}$)	$\frac{F(N\text{ II}_{6585})}{F(H\alpha)}$	$\frac{F(S\text{ II}_{total})}{F(H\alpha)}$	R^2
10	-0.1014	5559 ± 32	96 ± 30	12.1 ± 5.8	0.4 ± 0.4	0.3 ± 0.3	2.40
11	0.0000	5608 ± 21	122 ± 20	22.4 ± 6.3	0.7 ± 0.3	0.3 ± 0.2	2.92
14	0.3043	5171 ± 10	61 ± 10	4.2 ± 2.3	0.9 ± 0.7	3.5 ± 2.1	2.63

Table 11. UGC 01841: Measured Parameters.

Table 11—Continued

Row	Y-Offset (")	v_r (km s $^{-1}$)	σ_{gas} (km s $^{-1}$)	F(H α /10 $^{-16}$) (erg s $^{-1}$ cm $^{-2}$ Hz $^{-1}$)	$\frac{F(N\text{ II}_{6585})}{F(H\alpha)}$	$\frac{F(S\text{ II}_{total})}{F(H\alpha)}$	R^2
3	-0.8114	6350 ± 12	68 ± 11	4.0 ± 2.2	3.9 ± 2.4	0.4 ± 0.7	3.40
4	-0.7099	6339 ± 23	125 ± 23	14.1 ± 4.2	1.1 ± 0.4	0.5 ± 0.3	2.62
6	-0.5071	6276 ± 21	169 ± 19	9.2 ± 3.6	4.4 ± 1.9	1.1 ± 0.7	2.43
7	-0.4057	6371 ± 15	163 ± 14	16.3 ± 3.8	3.0 ± 0.8	0.1 ± 0.3	3.18
8	-0.3043	6428 ± 10	164 ± 10	22.8 ± 3.9	3.2 ± 0.6	0.9 ± 0.3	3.83
9	-0.2028	6329 ± 10	278 ± 8	110.7 ± 7.2	1.9 ± 0.2	1.1 ± 0.1	3.44
10	-0.1014	6337 ± 7	596 ± 6	215.6 ± 26.7	9.1 ± 1.1	3.2 ± 0.4	4.16
11	0.0000	6305 ± 5	592 ± 4	1001.2 ± 37.8	3.0 ± 0.1	1.1 ± 0.1	4.79
13	0.2028	6322 ± 26	260 ± 21	26.3 ± 5.2	2.2 ± 0.5	0.3 ± 0.2	3.46
14	0.3043	6126 ± 27	176 ± 26	5.2 ± 3.3	5.2 ± 3.5	2.8 ± 2.1	2.94
15	0.4057	6451 ± 31	105 ± 31	5.1 ± 3.0	1.6 ± 1.1	1.6 ± 1.2	3.10
17	0.6085	6407 ± 36	104 ± 33	10.6 ± 4.8	0.2 ± 0.2	0.5 ± 0.4	3.84

Slit 2: X-Offset +0.2"

1	-1.0142	6449 ± 35	172 ± 33	7.7 ± 3.1	2.0 ± 1.0	0.7 ± 0.6	4.02
3	-0.8114	6303 ± 12	109 ± 12	4.6 ± 2.1	4.8 ± 2.3	3.8 ± 1.9	3.60
6	-0.5071	6394 ± 10	85 ± 10	12.3 ± 2.7	1.5 ± 0.4	0.9 ± 0.3	3.62
7	-0.4057	6393 ± 5	72 ± 4	7.1 ± 1.9	5.2 ± 1.5	1.3 ± 0.5	3.12
8	-0.3043	6412 ± 5	111 ± 5	17.2 ± 2.6	3.9 ± 0.6	0.9 ± 0.3	3.54
9	-0.2028	6388 ± 5	120 ± 5	25.7 ± 3.1	2.4 ± 0.3	1.6 ± 0.3	4.25

Table 11—Continued

Row	Y-Offset (")	v_r (km s $^{-1}$)	σ_{gas} (km s $^{-1}$)	F(H α /10 $^{-16}$) (erg s $^{-1}$ cm $^{-2}$ Hz $^{-1}$)	$\frac{F(N\text{ II}_{6585})}{F(H\alpha)}$	$\frac{F(S\text{ II}_{total})}{F(H\alpha)}$	R^2
10	-0.1014	6390 ± 6	166 ± 6	42.1 ± 3.7	2.2 ± 0.2	1.5 ± 0.2	3.76
11	0.0000	6363 ± 6	150 ± 6	46.0 ± 3.8	1.5 ± 0.2	1.1 ± 0.1	3.04
12	0.1014	6415 ± 10	165 ± 9	21.3 ± 3.4	2.8 ± 0.5	1.1 ± 0.3	4.05
14	0.3043	6328 ± 20	123 ± 20	7.3 ± 2.6	2.4 ± 1.0	0.5 ± 0.6	4.44
17	0.6085	6204 ± 14	79 ± 14	6.7 ± 2.3	1.8 ± 0.8	0.1 ± 0.5	3.44
18	0.7099	6450 ± 44	268 ± 39	7.3 ± 3.6	3.6 ± 1.9	1.0 ± 0.9	3.65
20	0.9128	6391 ± 27	120 ± 27	7.7 ± 2.9	0.0 ± 0.2	1.9 ± 1.0	3.41
21	1.0142	6118 ± 7	45 ± 7	9.7 ± 2.3	0.4 ± 0.2	0.5 ± 0.3	3.95

Table 12. NGC 2329: Measured Parameters.

Row	Y-Offset (")	v_r (km s $^{-1}$)	σ_{gas} (km s $^{-1}$)	F(H α /10 $^{-16}$) (erg s $^{-1}$ cm $^{-2}$ Hz $^{-1}$)	$\frac{F(N\text{ II}_{6585})}{F(H\alpha)}$	$\frac{F(S\text{ II}_{total})}{F(H\alpha)}$	R^2
Slit 1: X-Offset -0.2"							
2	-0.9128	6017 ± 7	52 ± 7	13.0 ± 2.6	0.4 ± 0.1	0.3 ± 0.2	3.27
3	-0.8114	5709 ± 49	164 ± 48	4.6 ± 2.7	1.7 ± 1.2	1.7 ± 1.4	2.73
4	-0.7099	5752 ± 52	284 ± 40	28.8 ± 5.7	0.4 ± 0.2	0.2 ± 0.2	3.24
5	-0.6085	5973 ± 10	67 ± 11	8.9 ± 2.3	1.2 ± 0.4	0.5 ± 0.3	3.19
6	-0.5071	5989 ± 13	59 ± 12	8.8 ± 3.1	0.5 ± 0.3	0.8 ± 0.4	2.98
7	-0.4057	5493 ± 26	112 ± 26	7.4 ± 2.7	1.2 ± 0.6	0.6 ± 0.5	3.33
8	-0.3043	5816 ± 39	223 ± 30	12.7 ± 3.8	2.1 ± 0.7	0.2 ± 0.4	3.04
9	-0.2028	5810 ± 20	154 ± 20	9.5 ± 3.2	3.3 ± 1.3	0.2 ± 0.5	2.53
10	-0.1014	5763 ± 13	133 ± 13	16.6 ± 3.6	2.3 ± 0.6	0.7 ± 0.4	2.67
11	0.0000	5747 ± 13	150 ± 12	16.0 ± 3.2	3.4 ± 0.8	0.5 ± 0.4	2.51
12	0.1014	5775 ± 19	201 ± 16	25.0 ± 4.0	1.8 ± 0.4	0.1 ± 0.2	2.94
13	0.2028	5855 ± 26	170 ± 22	9.4 ± 3.0	2.7 ± 1.0	0.9 ± 0.6	2.90
14	0.3043	5678 ± 8	29 ± 7	2.8 ± 1.2	1.6 ± 0.9	1.0 ± 0.9	3.03
18	0.7099	5748 ± 32	137 ± 31	6.4 ± 2.6	1.6 ± 0.8	0.6 ± 0.7	3.22
Slit 0: X-Offset 0.0"							
1	-1.0142	5898 ± 23	74 ± 23	3.7 ± 2.6	2.2 ± 1.8	2.0 ± 2.0	1.93
5	-0.6085	6063 ± 10	38 ± 11	5.3 ± 2.5	1.2 ± 0.8	0.4 ± 0.6	2.34

Table 12—Continued

Row	Y-Offset (")	v_r (km s $^{-1}$)	σ_{gas} (km s $^{-1}$)	F(H α /10 $^{-16}$) (erg s $^{-1}$ cm $^{-2}$ Hz $^{-1}$)	$\frac{F(N\text{ II}_{6585})}{F(H\alpha)}$	$\frac{F(S\text{ II}_{total})}{F(H\alpha)}$	R^2
6	-0.5071	5877 ± 28	129 ± 28	11.8 ± 4.2	0.1 ± 0.3	1.9 ± 0.9	2.50
7	-0.4057	5943 ± 12	79 ± 11	11.8 ± 3.3	1.8 ± 0.7	1.1 ± 0.5	2.20
9	-0.2028	5819 ± 9	104 ± 9	20.5 ± 4.3	2.6 ± 0.6	1.7 ± 0.5	2.17
10	-0.1014	5795 ± 5	268 ± 5	96.0 ± 9.6	6.6 ± 0.7	2.2 ± 0.3	3.19
11	0.0000	5789 ± 4	301 ± 4	348.6 ± 13.8	3.0 ± 0.1	1.1 ± 0.1	3.82
12	0.1014	5735 ± 2	61 ± 2	30.4 ± 4.1	3.7 ± 0.6	0.1 ± 0.2	4.66
14	0.3043	5627 ± 16	76 ± 16	13.3 ± 4.5	0.7 ± 0.4	0.3 ± 0.4	2.64
20	0.9128	5782 ± 45	146 ± 43	12.2 ± 5.1	0.6 ± 0.4	0.2 ± 0.5	2.23
21	1.0142	5770 ± 38	111 ± 37	4.1 ± 3.0	2.5 ± 2.1	0.6 ± 1.4	2.25
Slit 2: X-Offset +0.2"							
1	-1.0142	5643 ± 37	154 ± 35	8.9 ± 3.4	1.4 ± 0.7	0.5 ± 0.6	2.15
2	-0.9128	5560 ± 7	32 ± 10	6.7 ± 2.9	0.4 ± 0.3	0.4 ± 0.4	2.48
8	-0.3043	5905 ± 5	53 ± 5	21.3 ± 3.3	0.5 ± 0.1	0.7 ± 0.2	2.64
9	-0.2028	5830 ± 21	195 ± 20	11.6 ± 3.8	3.9 ± 1.4	1.2 ± 0.7	2.69
10	-0.1014	5875 ± 9	119 ± 9	25.0 ± 3.8	1.9 ± 0.4	0.1 ± 0.2	2.94
11	0.0000	5844 ± 10	123 ± 10	24.2 ± 4.0	1.8 ± 0.4	1.0 ± 0.3	2.44
12	0.1014	5839 ± 6	82 ± 6	20.7 ± 3.3	1.8 ± 0.4	0.6 ± 0.2	2.66
13	0.2028	5742 ± 12	77 ± 12	12.5 ± 3.1	1.1 ± 0.4	0.5 ± 0.3	2.25
14	0.3043	5700 ± 8	45 ± 8	10.9 ± 2.9	0.7 ± 0.3	0.2 ± 0.3	2.58
15	0.4057	5631 ± 10	39 ± 9	6.5 ± 2.4	0.5 ± 0.3	0.3 ± 0.4	2.59

Table 12—Continued

Row	Y-Offset (")	v_r (km s $^{-1}$)	σ_{gas} (km s $^{-1}$)	F(H α /10 $^{-16}$) (erg s $^{-1}$ cm $^{-2}$ Hz $^{-1}$)	$\frac{F(N\text{ II}_{6585})}{F(H\alpha)}$	$\frac{F(S\text{ II}_{total})}{F(H\alpha)}$	R^2
17	0.6085	5774 ± 30	157 ± 29	4.8 ± 2.8	4.0 ± 2.5	0.5 ± 1.1	2.71
19	0.8114	5841 ± 20	60 ± 20	5.3 ± 2.7	0.6 ± 0.5	0.9 ± 0.8	2.43
20	0.9128	5742 ± 13	59 ± 13	5.4 ± 2.2	1.6 ± 0.8	0.5 ± 0.7	2.61

Table 13. NGC 2892: Measured Parameters.

Row	Y-Offset (")	v_r (km s $^{-1}$)	σ_{gas} (km s $^{-1}$)	F(H α /10 $^{-16}$) (erg s $^{-1}$ cm $^{-2}$ Hz $^{-1}$)	$\frac{F(N\text{ II}_{6585})}{F(H\alpha)}$	$\frac{F(S\text{ II}_{total})}{F(H\alpha)}$	R^2
Slit 1: X-Offset -0.2"							
1	-1.0142	6843 ± 8	25 ± 6	1.4 ± 0.9	1.1 ± 0.9	4.9 ± 3.6	3.48
3	-0.8114	6649 ± 13	76 ± 12	15.2 ± 3.6	0.1 ± 0.1	0.4 ± 0.2	3.31
4	-0.7099	6895 ± 22	143 ± 22	7.9 ± 2.5	1.8 ± 0.7	1.2 ± 0.7	3.43
6	-0.5071	6700 ± 20	71 ± 20	3.1 ± 1.9	2.0 ± 1.5	0.6 ± 1.0	3.25
8	-0.3043	6905 ± 14	81 ± 13	10.1 ± 2.7	0.9 ± 0.3	0.3 ± 0.3	3.19
9	-0.2028	6912 ± 23	71 ± 23	5.7 ± 2.7	0.5 ± 0.4	1.0 ± 0.7	3.18
11	0.0000	6844 ± 9	98 ± 9	10.4 ± 2.7	2.5 ± 0.7	0.5 ± 0.4	3.17
12	0.1014	6868 ± 12	99 ± 12	3.9 ± 2.9	5.8 ± 4.4	2.5 ± 2.1	2.98
13	0.2028	6935 ± 9	85 ± 10	3.6 ± 2.1	5.5 ± 3.4	3.6 ± 2.4	2.94
15	0.4057	6856 ± 8	35 ± 7	3.0 ± 1.4	1.8 ± 1.0	1.7 ± 1.3	2.95
16	0.5071	6891 ± 4	36 ± 3	8.0 ± 1.7	1.5 ± 0.4	0.3 ± 0.3	2.74
19	0.8114	6674 ± 22	71 ± 22	6.7 ± 2.8	0.0 ± 0.2	0.4 ± 0.4	3.38
21	1.0142	6931 ± 13	31 ± 13	3.4 ± 2.0	0.2 ± 0.3	0.1 ± 0.5	3.43
Slit 0: X-Offset 0.0"							
1	-1.0142	6734 ± 46	157 ± 44	5.8 ± 3.7	2.1 ± 1.6	1.2 ± 1.2	2.11
3	-0.8114	6665 ± 27	66 ± 26	7.1 ± 3.9	0.2 ± 0.3	0.5 ± 0.6	2.21
9	-0.2028	6962 ± 24	206 ± 21	26.6 ± 5.4	1.5 ± 0.4	0.1 ± 0.3	2.25

Table 13—Continued

Row	Y-Offset (")	v_r (km s $^{-1}$)	σ_{gas} (km s $^{-1}$)	F(H α /10 $^{-16}$) (erg s $^{-1}$ cm $^{-2}$ Hz $^{-1}$)	$\frac{F(N\text{ II}_{6585})}{F(H\alpha)}$	$\frac{F(S\text{ II}_{total})}{F(H\alpha)}$	R^2
10	-0.1014	6844 ± 19	354 ± 18	28.1 ± 7.8	5.9 ± 1.7	1.4 ± 0.5	2.24
11	0.0000	6938 ± 7	453 ± 6	240.9 ± 17.0	4.3 ± 0.3	1.1 ± 0.1	2.44
12	0.1014	6947 ± 10	452 ± 9	259.5 ± 17.3	2.8 ± 0.2	0.5 ± 0.1	2.96
21	1.0142	6956 ± 33	81 ± 34	4.1 ± 2.9	1.5 ± 1.6	0.3 ± 1.1	1.98
Slit 2: X-Offset +0.2"							
3	-0.8114	6894 ± 28	65 ± 26	4.3 ± 2.7	0.0 ± 0.4	1.7 ± 1.4	2.70
4	-0.7099	7218 ± 44	147 ± 43	3.8 ± 2.9	3.0 ± 2.6	0.1 ± 1.2	1.70
5	-0.6085	6902 ± 34	134 ± 31	15.9 ± 5.5	0.0 ± 0.1	0.2 ± 0.3	2.70
7	-0.4057	6801 ± 21	92 ± 21	7.4 ± 3.0	1.5 ± 0.8	0.3 ± 0.6	2.44
10	-0.1014	6963 ± 43	260 ± 37	11.0 ± 4.7	2.9 ± 1.4	1.2 ± 0.9	2.22
11	0.0000	6840 ± 13	169 ± 12	38.5 ± 5.1	1.1 ± 0.2	0.2 ± 0.2	2.62
12	0.1014	6890 ± 10	138 ± 9	16.2 ± 3.3	3.2 ± 0.7	0.7 ± 0.4	2.52
13	0.2028	6957 ± 17	183 ± 17	5.8 ± 3.3	7.7 ± 4.6	1.0 ± 1.3	2.55
14	0.3043	6938 ± 26	135 ± 26	5.8 ± 3.0	2.9 ± 1.7	0.4 ± 0.9	2.42
15	0.4057	6899 ± 26	54 ± 25	4.3 ± 2.9	0.5 ± 0.6	0.4 ± 0.8	2.46
16	0.5071	6980 ± 38	213 ± 32	9.4 ± 4.0	2.6 ± 1.3	0.8 ± 0.8	2.17
17	0.6085	7064 ± 8	42 ± 8	3.2 ± 1.7	3.4 ± 2.0	0.4 ± 0.9	2.46

Table 14. NGC 3801: Measured Parameters.

Row	Y-Offset (")	v_r (km s $^{-1}$)	σ_{gas} (km s $^{-1}$)	F(H α /10 $^{-16}$) (erg s $^{-1}$ cm $^{-2}$ Hz $^{-1}$)	$\frac{F(\text{N II}_{6585})}{F(\text{H}\alpha)}$	$\frac{F(\text{S II}_{total})}{F(\text{H}\alpha)}$	R^2
Slit 1: X-Offset -0.2"							
2	-0.9128	3372 ± 40	89 ± 40	3.7 ± 2.2	0.0 ± 0.3	0.2 ± 0.6	3.00
3	-0.8114	3436 ± 16	57 ± 16	4.3 ± 1.7	0.4 ± 0.3	0.4 ± 0.5	3.49
4	-0.7099	3468 ± 9	46 ± 9	3.4 ± 1.2	1.0 ± 0.5	1.7 ± 0.9	3.59
7	-0.4057	3476 ± 9	48 ± 9	1.5 ± 1.0	1.0 ± 0.9	7.5 ± 5.2	3.41
9	-0.2028	3325 ± 13	161 ± 12	25.4 ± 3.3	0.9 ± 0.2	0.8 ± 0.2	3.78
10	-0.1014	3383 ± 10	143 ± 9	20.8 ± 2.9	1.7 ± 0.3	0.8 ± 0.2	3.66
11	0.0000	3378 ± 12	142 ± 11	15.6 ± 2.8	1.9 ± 0.4	1.3 ± 0.3	3.01
12	0.1014	3345 ± 17	148 ± 17	14.5 ± 2.9	1.0 ± 0.3	1.1 ± 0.4	3.50
14	0.3043	3471 ± 16	74 ± 17	2.5 ± 1.5	3.1 ± 2.2	2.1 ± 1.7	3.23
17	0.6085	3317 ± 26	113 ± 24	8.0 ± 2.7	1.0 ± 0.5	0.3 ± 0.4	3.53
20	0.9128	3190 ± 19	56 ± 20	2.9 ± 1.6	0.9 ± 0.7	0.9 ± 0.9	3.17
Slit 0: X-Offset 0.0"							
2	-0.9128	3510 ± 26	124 ± 26	6.3 ± 2.5	1.7 ± 0.8	1.4 ± 0.8	2.76
3	-0.8114	3461 ± 17	57 ± 17	3.4 ± 1.8	1.2 ± 0.8	1.4 ± 1.2	2.43
6	-0.5071	3448 ± 18	157 ± 17	11.5 ± 2.8	2.5 ± 0.7	0.3 ± 0.4	2.51
8	-0.3043	3438 ± 12	75 ± 12	4.7 ± 2.0	2.6 ± 1.3	2.5 ± 1.3	2.02
9	-0.2028	3486 ± 12	146 ± 12	16.0 ± 3.0	2.1 ± 0.5	1.6 ± 0.4	2.55

Table 14—Continued

Row	Y-Offset (")	v_r (km s $^{-1}$)	σ_{gas} (km s $^{-1}$)	F(H α /10 $^{-16}$) (erg s $^{-1}$ cm $^{-2}$ Hz $^{-1}$)	$\frac{F(N\text{ II}_{6585})}{F(H\alpha)}$	$\frac{F(S\text{ II}_{total})}{F(H\alpha)}$	R^2
10	-0.1014	3510 ± 12	174 ± 11	25.0 ± 3.7	2.0 ± 0.4	1.1 ± 0.3	2.56
11	0.0000	3498 ± 12	163 ± 12	25.8 ± 4.1	1.8 ± 0.4	1.1 ± 0.3	2.32
12	0.1014	3451 ± 14	129 ± 14	9.9 ± 3.1	3.1 ± 1.1	2.3 ± 0.9	2.72
13	0.2028	3397 ± 20	125 ± 20	10.8 ± 3.3	1.5 ± 0.6	1.1 ± 0.6	2.27
14	0.3043	3425 ± 31	208 ± 26	22.9 ± 4.7	0.9 ± 0.3	0.2 ± 0.3	2.20
17	0.6085	2822 ± 37	205 ± 36	21.4 ± 5.4	0.1 ± 0.1	0.7 ± 0.3	2.57
19	0.8114	3194 ± 28	108 ± 28	9.7 ± 3.5	0.1 ± 0.2	0.7 ± 0.5	2.43
20	0.9128	3184 ± 38	164 ± 38	13.8 ± 4.3	0.1 ± 0.2	0.5 ± 0.4	2.71
21	1.0142	3263 ± 47	180 ± 44	11.2 ± 4.1	0.5 ± 0.3	0.8 ± 0.5	2.66
Slit 2: X-Offset +0.2"							
2	-0.9128	3405 ± 17	53 ± 17	3.5 ± 1.7	0.7 ± 0.5	0.8 ± 0.7	2.96
3	-0.8114	3455 ± 15	47 ± 15	3.7 ± 1.6	0.6 ± 0.4	0.1 ± 0.4	2.64
4	-0.7099	3506 ± 10	39 ± 10	1.3 ± 0.9	3.4 ± 2.7	1.9 ± 1.9	2.44
5	-0.6085	3388 ± 16	67 ± 16	3.5 ± 1.6	0.1 ± 0.3	2.5 ± 1.4	2.43
7	-0.4057	3447 ± 19	119 ± 19	8.6 ± 2.4	0.5 ± 0.2	2.4 ± 0.8	2.75
8	-0.3043	3456 ± 11	102 ± 10	15.3 ± 2.9	0.7 ± 0.2	1.3 ± 0.3	2.62
9	-0.2028	3522 ± 12	93 ± 12	6.4 ± 1.9	2.1 ± 0.7	2.1 ± 0.8	2.93
10	-0.1014	3640 ± 17	138 ± 17	11.2 ± 2.6	1.0 ± 0.3	2.1 ± 0.6	2.70
11	0.0000	3611 ± 18	140 ± 18	8.7 ± 2.4	1.4 ± 0.5	2.8 ± 0.9	2.98
12	0.1014	3518 ± 19	121 ± 19	7.2 ± 2.3	1.1 ± 0.5	2.9 ± 1.1	2.93

Table 14—Continued

Row	Y-Offset (")	v_r (km s $^{-1}$)	σ_{gas} (km s $^{-1}$)	F(H α /10 $^{-16}$) (erg s $^{-1}$ cm $^{-2}$ Hz $^{-1}$)	$\frac{F(N\text{ II}_{6585})}{F(H\alpha)}$	$\frac{F(S\text{ II}_{total})}{F(H\alpha)}$	R^2
13	0.2028	3441 ± 8	38 ± 8	5.9 ± 1.9	0.5 ± 0.3	0.6 ± 0.4	2.52
14	0.3043	3456 ± 9	63 ± 9	10.1 ± 2.2	0.5 ± 0.2	0.9 ± 0.4	2.43
15	0.4057	3451 ± 9	59 ± 9	7.8 ± 1.9	0.8 ± 0.3	1.5 ± 0.5	2.31
20	0.9128	3482 ± 18	99 ± 19	4.7 ± 1.8	1.8 ± 0.8	2.0 ± 1.0	2.90

Table 15. NGC 3862: Measured Parameters.

Table 15—Continued

Row	Y-Offset (")	v_r (km s $^{-1}$)	σ_{gas} (km s $^{-1}$)	F(H α /10 $^{-16}$) (erg s $^{-1}$ cm $^{-2}$ Hz $^{-1}$)	F(N II ₆₅₈₅) F(H α)	F(S II _{total}) F(H α)	R^2
4	-0.7099	6525 ± 19	50 ± 19	7.6 ± 4.7	1.0 ± 0.9	0.5 ± 0.9	1.75
5	-0.6085	6510 ± 7	38 ± 8	17.5 ± 5.4	0.4 ± 0.2	0.6 ± 0.4	1.70
6	-0.5071	6503 ± 7	43 ± 7	10.1 ± 3.7	2.1 ± 0.9	1.1 ± 0.7	1.82
7	-0.4057	6512 ± 7	52 ± 6	21.3 ± 5.0	1.3 ± 0.4	0.3 ± 0.3	1.81
8	-0.3043	6520 ± 7	52 ± 7	14.0 ± 4.3	1.9 ± 0.7	1.4 ± 0.7	1.88
9	-0.2028	6520 ± 10	116 ± 10	39.4 ± 7.4	1.8 ± 0.4	0.2 ± 0.2	2.34
10	-0.1014	6605 ± 6	267 ± 6	84.9 ± 13.8	9.4 ± 1.6	3.7 ± 0.7	3.40
11	0.0000	6441 ± 4	302 ± 3	854.0 ± 25.6	2.4 ± 0.1	1.0 ± 0.1	4.21
12	0.1014	6474 ± 6	197 ± 6	18.8 ± 8.2	17.9 ± 7.8	0.7 ± 0.8	4.59
13	0.2028	6487 ± 15	147 ± 15	11.5 ± 5.8	6.2 ± 3.3	0.1 ± 0.9	2.01
14	0.3043	6526 ± 6	49 ± 6	20.9 ± 4.8	1.1 ± 0.3	0.6 ± 0.3	1.90
16	0.5071	6603 ± 44	199 ± 37	20.5 ± 7.9	1.5 ± 0.7	0.0 ± 0.5	1.96
17	0.6085	6511 ± 28	95 ± 28	10.6 ± 5.8	1.4 ± 1.0	0.4 ± 0.7	1.76

Slit 2: X-Offset +0.2"

1	-1.0142	6364 ± 50	235 ± 40	14.1 ± 5.9	2.1 ± 1.0	0.4 ± 0.6	1.90
3	-0.8114	6480 ± 14	51 ± 13	5.6 ± 3.2	1.8 ± 1.2	0.9 ± 0.9	2.27
4	-0.7099	6526 ± 5	40 ± 5	5.6 ± 2.3	3.7 ± 1.7	1.8 ± 1.0	2.43
5	-0.6085	6536 ± 7	46 ± 7	12.8 ± 3.5	1.1 ± 0.4	0.1 ± 0.3	2.27
6	-0.5071	6541 ± 8	65 ± 8	18.3 ± 4.1	1.2 ± 0.3	0.3 ± 0.3	2.32
7	-0.4057	6527 ± 5	74 ± 5	12.7 ± 3.5	3.8 ± 1.1	0.8 ± 0.5	2.81

Table 15—Continued

Row	Y-Offset (")	v_r (km s $^{-1}$)	σ_{gas} (km s $^{-1}$)	F(H α /10 $^{-16}$) (erg s $^{-1}$ cm $^{-2}$ Hz $^{-1}$)	$\frac{F(N\text{ II}_{6585})}{F(H\alpha)}$	$\frac{F(S\text{ II}_{total})}{F(H\alpha)}$	R^2
8	-0.3043	6554 ± 7	77 ± 7	16.0 ± 3.6	2.2 ± 0.6	1.3 ± 0.5	2.32
9	-0.2028	6551 ± 14	149 ± 14	15.1 ± 4.7	3.6 ± 1.2	1.1 ± 0.6	2.33
10	-0.1014	6625 ± 9	102 ± 8	13.9 ± 3.8	3.5 ± 1.1	2.5 ± 0.9	2.61
11	0.0000	6603 ± 10	118 ± 9	28.3 ± 5.1	2.0 ± 0.4	0.5 ± 0.3	1.99
12	0.1014	6581 ± 20	214 ± 18	26.8 ± 5.8	2.5 ± 0.6	1.1 ± 0.5	2.45
13	0.2028	6435 ± 34	235 ± 29	23.6 ± 6.3	1.8 ± 0.6	0.7 ± 0.4	2.06
14	0.3043	6450 ± 64	263 ± 49	26.0 ± 7.9	0.9 ± 0.4	0.5 ± 0.4	2.12
15	0.4057	6568 ± 6	46 ± 5	23.8 ± 4.4	0.5 ± 0.1	0.2 ± 0.2	1.99
16	0.5071	6530 ± 7	55 ± 7	15.6 ± 3.5	1.0 ± 0.3	1.3 ± 0.5	2.44

Table 16. UGC 7115: Measured Parameters.

Row	Y-Offset (")	v_r (km s $^{-1}$)	σ_{gas} (km s $^{-1}$)	F(H α /10 $^{-16}$) (erg s $^{-1}$ cm $^{-2}$ Hz $^{-1}$)	$\frac{F(N\text{ II}_{6585})}{F(H\alpha)}$	$\frac{F(S\text{ II}_{total})}{F(H\alpha)}$	R^2
Slit 0: X-Offset 0.0"							
5	-0.6085	6792 ± 17	63 ± 18	5.7 ± 2.7	1.0 ± 0.7	0.6 ± 0.5	2.59
6	-0.5071	6886 ± 9	49 ± 8	8.4 ± 2.5	1.0 ± 0.4	0.5 ± 0.3	2.90
7	-0.4057	6863 ± 6	57 ± 6	15.8 ± 3.0	0.8 ± 0.2	0.7 ± 0.2	2.65
8	-0.3043	6897 ± 7	64 ± 7	15.1 ± 2.9	1.2 ± 0.3	0.6 ± 0.2	2.84
9	-0.2028	6914 ± 9	107 ± 9	17.1 ± 3.8	2.3 ± 0.6	0.9 ± 0.3	2.53
10	-0.1014	6963 ± 10	271 ± 9	74.7 ± 6.9	2.6 ± 0.3	1.1 ± 0.1	2.48
11	0.0000	6801 ± 9	496 ± 7	372.8 ± 19.3	2.4 ± 0.1	1.4 ± 0.1	2.79
12	0.1014	6625 ± 13	545 ± 10	138.7 ± 20.7	5.6 ± 0.8	2.3 ± 0.4	3.86
13	0.2028	6669 ± 8	224 ± 7	62.4 ± 5.0	2.3 ± 0.2	0.9 ± 0.1	2.92
15	0.4057	6639 ± 8	69 ± 8	3.1 ± 1.9	5.6 ± 3.7	4.7 ± 3.1	2.78
16	0.5071	6661 ± 5	40 ± 6	5.7 ± 1.8	1.9 ± 0.7	0.7 ± 0.4	2.42

Table 17. NGC 4261: Measured Parameters.

Table 17—Continued

Row	Y-Offset (")	v_r (km s $^{-1}$)	σ_{gas} (km s $^{-1}$)	F(H α /10 $^{-16}$) (erg s $^{-1}$ cm $^{-2}$ Hz $^{-1}$)	$\frac{F(N\text{ II}_{6585})}{F(H\alpha)}$	$\frac{F(S\text{ II}_{total})}{F(H\alpha)}$	R^2
1	-0.5071	2327 ± 27	112 ± 26	33.6 ± 17.5	2.3 ± 1.4	0.4 ± 0.5	1.93
2	-0.4564	2283 ± 22	155 ± 21	51.3 ± 18.9	3.0 ± 1.3	0.7 ± 0.5	1.89
3	-0.4057	2274 ± 20	152 ± 18	46.9 ± 18.1	3.1 ± 1.3	2.6 ± 1.1	1.33
4	-0.3550	2216 ± 13	141 ± 12	71.3 ± 18.5	3.2 ± 0.9	1.8 ± 0.6	1.64
5	-0.3043	2233 ± 14	164 ± 13	84.7 ± 19.9	2.7 ± 0.7	2.2 ± 0.6	1.77
6	-0.2535	2249 ± 18	191 ± 15	125.0 ± 23.4	2.2 ± 0.5	0.4 ± 0.2	2.05
7	-0.2028	2280 ± 12	139 ± 12	118.2 ± 20.7	1.8 ± 0.4	0.5 ± 0.2	1.71
8	-0.1521	2243 ± 13	189 ± 11	161.9 ± 23.5	2.1 ± 0.4	1.0 ± 0.2	1.77
9	-0.1014	2210 ± 11	182 ± 10	83.5 ± 19.1	5.0 ± 1.2	2.8 ± 0.7	1.72
10	-0.0507	2194 ± 11	205 ± 10	91.9 ± 21.1	5.6 ± 1.4	2.4 ± 0.6	1.98
11	0.0000	2140 ± 18	290 ± 17	70.1 ± 25.7	8.2 ± 3.1	4.3 ± 1.7	1.71
12	0.0507	2184 ± 14	194 ± 12	68.1 ± 20.3	4.9 ± 1.5	3.6 ± 1.1	1.67
13	0.1014	2189 ± 15	147 ± 16	40.8 ± 16.1	5.0 ± 2.1	1.8 ± 0.9	1.58
14	0.1521	2156 ± 11	79 ± 11	41.0 ± 13.1	2.6 ± 1.0	1.3 ± 0.6	1.79
15	0.2028	2212 ± 15	84 ± 15	33.1 ± 13.8	2.2 ± 1.1	1.7 ± 0.9	1.86
Slit 2: X-Offset +0.1"							
1	-0.5071	2341 ± 18	116 ± 17	73.2 ± 20.6	1.6 ± 0.6	0.3 ± 0.3	1.74
2	-0.4564	2300 ± 17	135 ± 17	76.0 ± 20.4	2.1 ± 0.7	0.4 ± 0.3	1.54
3	-0.4057	2261 ± 17	131 ± 16	79.8 ± 20.2	2.0 ± 0.6	0.5 ± 0.3	1.44

Table 17—Continued

Row	Y-Offset (")	v_r (km s $^{-1}$)	σ_{gas} (km s $^{-1}$)	F(H α /10 $^{-16}$) (erg s $^{-1}$ cm $^{-2}$ Hz $^{-1}$)	$\frac{F(N\text{ II}_{6585})}{F(H\alpha)}$	$\frac{F(S\text{ II}_{total})}{F(H\alpha)}$	R^2
4	-0.3550	2212 ± 22	214 ± 18	127.7 ± 25.1	2.1 ± 0.5	0.9 ± 0.3	1.61
5	-0.3043	2228 ± 20	163 ± 18	57.2 ± 19.1	3.1 ± 1.2	2.0 ± 0.8	1.83
6	-0.2535	2317 ± 15	110 ± 15	63.7 ± 18.3	1.7 ± 0.6	1.4 ± 0.5	1.52
7	-0.2028	2308 ± 15	83 ± 15	31.6 ± 14.8	2.7 ± 1.5	1.2 ± 0.8	1.54
8	-0.1521	2244 ± 22	167 ± 20	85.7 ± 21.9	1.9 ± 0.6	1.0 ± 0.4	1.52
9	-0.1014	2271 ± 12	144 ± 11	73.4 ± 17.9	3.3 ± 0.9	2.1 ± 0.6	1.59
10	-0.0507	2223 ± 9	125 ± 8	97.9 ± 18.0	2.8 ± 0.6	1.5 ± 0.4	1.33
11	0.0000	2243 ± 11	139 ± 11	93.6 ± 18.9	2.9 ± 0.7	1.3 ± 0.3	1.48
12	0.0507	2251 ± 9	103 ± 9	37.2 ± 16.5	6.0 ± 2.8	2.4 ± 1.2	1.94
13	0.1014	2199 ± 19	170 ± 18	26.7 ± 19.0	8.4 ± 6.1	3.6 ± 2.7	1.39
15	0.2028	1984 ± 49	251 ± 38	49.4 ± 21.9	3.1 ± 1.5	2.4 ± 1.2	1.63
16	0.2535	2091 ± 34	161 ± 31	66.0 ± 21.6	1.1 ± 0.5	1.0 ± 0.5	1.63
20	0.4564	2022 ± 24	90 ± 24	21.6 ± 14.0	2.3 ± 1.8	1.6 ± 1.3	1.60

Table 18. NGC 4335: Measured Parameters.

Row	Y-Offset (")	v_r (km s $^{-1}$)	σ_{gas} (km s $^{-1}$)	F(H α /10 $^{-16}$) (erg s $^{-1}$ cm $^{-2}$ Hz $^{-1}$)	$\frac{F(N\text{ II}_{6585})}{F(H\alpha)}$	$\frac{F(S\text{ II}_{total})}{F(H\alpha)}$	R^2
Slit 1: X-Offset -0.2"							
1	-1.0142	4955 ± 12	94 ± 12	5.4 ± 1.6	2.3 ± 0.8	0.8 ± 0.5	2.80
3	-0.8114	4943 ± 7	92 ± 7	13.0 ± 1.9	1.8 ± 0.3	0.8 ± 0.3	2.81
4	-0.7099	4915 ± 9	107 ± 9	14.3 ± 2.2	1.7 ± 0.3	1.0 ± 0.3	2.37
5	-0.6085	4928 ± 7	84 ± 7	8.5 ± 1.9	2.9 ± 0.7	1.3 ± 0.5	2.29
6	-0.5071	4967 ± 6	83 ± 6	13.7 ± 2.2	2.0 ± 0.4	0.3 ± 0.2	2.15
7	-0.4057	4947 ± 5	85 ± 5	20.8 ± 2.6	1.7 ± 0.3	0.8 ± 0.2	1.84
8	-0.3043	4904 ± 8	111 ± 8	19.2 ± 3.1	2.2 ± 0.4	1.0 ± 0.3	2.20
9	-0.2028	4807 ± 10	160 ± 9	29.5 ± 4.0	2.3 ± 0.4	1.0 ± 0.3	2.43
10	-0.1014	4711 ± 7	174 ± 6	41.4 ± 4.4	2.8 ± 0.3	0.5 ± 0.2	2.06
11	0.0000	4639 ± 5	163 ± 5	45.9 ± 4.2	3.1 ± 0.3	0.9 ± 0.2	2.34
12	0.1014	4606 ± 6	158 ± 6	36.3 ± 3.9	3.0 ± 0.4	0.6 ± 0.2	2.14
13	0.2028	4540 ± 6	109 ± 6	15.5 ± 3.0	3.4 ± 0.7	0.4 ± 0.3	2.50
14	0.3043	4507 ± 6	83 ± 6	6.1 ± 2.3	5.4 ± 2.1	1.0 ± 0.7	3.17
16	0.5071	4471 ± 10	100 ± 10	8.3 ± 2.0	2.4 ± 0.7	0.7 ± 0.4	2.72
17	0.6085	4416 ± 29	227 ± 25	9.4 ± 2.9	2.4 ± 0.8	0.7 ± 0.5	2.99
18	0.7099	4476 ± 18	129 ± 18	9.0 ± 2.3	1.3 ± 0.4	1.0 ± 0.4	3.24
20	0.9128	4526 ± 17	97 ± 18	7.0 ± 2.1	1.0 ± 0.4	0.5 ± 0.4	3.04
21	1.0142	4531 ± 21	138 ± 22	6.3 ± 2.0	1.2 ± 0.5	1.7 ± 0.7	3.68

Table 18—Continued

Row	Y-Offset (")	v_r (km s $^{-1}$)	σ_{gas} (km s $^{-1}$)	F(H α /10 $^{-16}$) (erg s $^{-1}$ cm $^{-2}$ Hz $^{-1}$)	$\frac{F(N\text{ II}_{6585})}{F(H\alpha)}$	$\frac{F(S\text{ II}_{total})}{F(H\alpha)}$	R^2
Slit 0: X-Offset 0.0"							
1	-1.0142	4940 ± 11	80 ± 11	9.7 ± 2.5	1.4 ± 0.5	0.8 ± 0.4	2.16
2	-0.9128	4928 ± 8	70 ± 8	7.0 ± 2.1	2.5 ± 0.9	1.5 ± 0.7	2.21
3	-0.8114	4912 ± 6	60 ± 6	15.7 ± 2.7	1.1 ± 0.2	1.0 ± 0.3	2.18
4	-0.7099	4910 ± 5	55 ± 5	17.8 ± 2.8	0.9 ± 0.2	0.8 ± 0.2	2.31
5	-0.6085	4906 ± 7	61 ± 7	17.0 ± 3.1	0.9 ± 0.2	0.9 ± 0.3	2.01
6	-0.5071	4890 ± 22	170 ± 21	12.9 ± 4.2	2.7 ± 1.0	1.7 ± 0.8	1.88
7	-0.4057	4865 ± 20	207 ± 19	12.8 ± 4.8	4.7 ± 1.9	1.7 ± 1.0	1.62
8	-0.3043	4800 ± 10	133 ± 10	27.1 ± 4.9	2.4 ± 0.5	1.1 ± 0.4	1.66
9	-0.2028	4749 ± 8	162 ± 7	42.6 ± 5.8	3.0 ± 0.5	1.7 ± 0.3	1.56
10	-0.1014	4683 ± 4	210 ± 3	155.9 ± 8.1	3.0 ± 0.2	1.3 ± 0.1	2.19
11	0.0000	4619 ± 3	248 ± 2	337.3 ± 10.3	2.6 ± 0.1	1.0 ± 0.1	3.21
12	0.1014	4568 ± 3	220 ± 3	206.9 ± 8.2	2.7 ± 0.1	1.0 ± 0.1	2.19
13	0.2028	4531 ± 5	134 ± 5	47.9 ± 5.2	3.3 ± 0.4	1.2 ± 0.2	1.72
14	0.3043	4493 ± 8	131 ± 8	28.0 ± 4.7	2.7 ± 0.5	1.1 ± 0.3	1.98
15	0.4057	4376 ± 17	168 ± 17	22.7 ± 5.1	2.0 ± 0.5	0.6 ± 0.3	2.11
16	0.5071	4372 ± 22	175 ± 21	18.7 ± 4.7	2.0 ± 0.6	0.8 ± 0.4	2.39
17	0.6085	4406 ± 17	148 ± 17	17.0 ± 4.0	1.9 ± 0.5	1.1 ± 0.4	2.28
18	0.7099	4383 ± 13	123 ± 14	12.2 ± 3.2	2.2 ± 0.7	1.6 ± 0.6	2.16
19	0.8114	4438 ± 23	159 ± 23	8.8 ± 3.2	2.5 ± 1.1	1.6 ± 0.8	2.54

Table 18—Continued

Row	Y-Offset (")	v_r (km s $^{-1}$)	σ_{gas} (km s $^{-1}$)	F(H α /10 $^{-16}$) (erg s $^{-1}$ cm $^{-2}$ Hz $^{-1}$)	$\frac{F(N\text{ II}_{6585})}{F(H\alpha)}$	$\frac{F(S\text{ II}_{total})}{F(H\alpha)}$	R^2
Slit 2: X-Offset +0.2"							
1	-1.0142	4683 ± 53	259 ± 49	5.1 ± 3.6	3.2 ± 2.4	3.5 ± 2.8	2.72
4	-0.7099	4883 ± 14	67 ± 14	6.0 ± 2.3	1.5 ± 0.7	0.3 ± 0.5	2.69
5	-0.6085	4767 ± 14	103 ± 15	9.7 ± 2.9	1.9 ± 0.7	1.1 ± 0.6	2.17
7	-0.4057	4725 ± 13	114 ± 12	16.2 ± 4.0	1.8 ± 0.5	0.7 ± 0.4	1.95
8	-0.3043	4713 ± 13	109 ± 12	13.5 ± 3.7	2.2 ± 0.7	1.1 ± 0.5	1.74
9	-0.2028	4673 ± 8	82 ± 8	8.4 ± 3.2	4.4 ± 1.8	1.5 ± 0.9	1.72
10	-0.1014	4654 ± 5	76 ± 5	11.8 ± 3.0	4.3 ± 1.2	1.9 ± 0.7	1.95
11	0.0000	4605 ± 5	83 ± 5	12.2 ± 3.2	4.8 ± 1.3	1.4 ± 0.6	1.74
12	0.1014	4550 ± 5	94 ± 6	13.7 ± 3.4	5.0 ± 1.3	1.4 ± 0.6	1.94
13	0.2028	4509 ± 6	115 ± 6	22.4 ± 3.7	3.7 ± 0.7	0.9 ± 0.3	1.70
14	0.3043	4504 ± 11	145 ± 10	12.6 ± 3.7	4.8 ± 1.5	1.6 ± 0.7	1.85
15	0.4057	4481 ± 19	158 ± 18	13.8 ± 3.9	2.4 ± 0.8	0.8 ± 0.5	1.75
16	0.5071	4329 ± 6	54 ± 6	14.9 ± 2.9	1.0 ± 0.3	0.4 ± 0.2	1.68
17	0.6085	4325 ± 7	58 ± 7	12.0 ± 3.1	1.2 ± 0.4	0.4 ± 0.3	2.24
18	0.7099	4352 ± 14	128 ± 14	5.8 ± 2.6	4.6 ± 2.2	3.4 ± 1.8	2.51
19	0.8114	4345 ± 10	78 ± 10	5.3 ± 2.1	2.9 ± 1.3	1.7 ± 1.0	2.20
21	1.0142	4476 ± 34	152 ± 34	4.3 ± 2.7	2.7 ± 1.9	0.9 ± 1.1	3.22

Table 19. M84 : Measured Parameters.

Row	Y-Offset (")	v_r (km s $^{-1}$)	σ_{gas} (km s $^{-1}$)	F(H α /10 $^{-16}$) (erg s $^{-1}$ cm $^{-2}$ Hz $^{-1}$)	$\frac{F(N\text{ II}_{6585})}{F(H\alpha)}$	$\frac{F(S\text{ II}_{total})}{F(H\alpha)}$	R^2
Slit 1: X-Offset -0.2"							
1	-0.5071	1088 ± 7	89 ± 8	19.3 ± 3.2	1.9 ± 0.4	0.9 ± 0.3	1.33
2	-0.4564	1071 ± 6	88 ± 6	14.4 ± 2.8	3.2 ± 0.7	1.6 ± 0.4	1.28
3	-0.4057	1064 ± 7	95 ± 7	21.7 ± 3.3	2.2 ± 0.4	1.0 ± 0.2	1.36
4	-0.3550	1061 ± 6	101 ± 6	31.6 ± 3.6	1.9 ± 0.3	1.1 ± 0.2	1.22
5	-0.3043	1068 ± 5	118 ± 5	45.4 ± 4.0	1.9 ± 0.2	0.9 ± 0.1	1.34
6	-0.2535	1106 ± 4	126 ± 4	53.1 ± 3.9	2.5 ± 0.2	1.2 ± 0.1	1.39
7	-0.2028	1102 ± 3	115 ± 3	67.7 ± 4.0	2.2 ± 0.2	1.1 ± 0.1	1.42
8	-0.1521	1102 ± 2	102 ± 2	65.0 ± 3.6	2.3 ± 0.2	1.5 ± 0.1	1.54
9	-0.1014	1099 ± 2	124 ± 2	79.8 ± 3.9	2.5 ± 0.1	1.6 ± 0.1	1.50
10	-0.0507	1076 ± 2	137 ± 2	104.9 ± 4.1	2.7 ± 0.1	1.8 ± 0.1	1.65
11	0.0000	1026 ± 2	178 ± 2	150.0 ± 4.9	2.5 ± 0.1	1.8 ± 0.1	1.58
12	0.0507	944 ± 2	197 ± 2	168.1 ± 5.2	2.5 ± 0.1	1.8 ± 0.1	1.61
13	0.1014	878 ± 2	190 ± 2	153.1 ± 5.1	2.7 ± 0.1	1.7 ± 0.1	1.33
14	0.1521	856 ± 3	200 ± 2	131.4 ± 5.0	2.8 ± 0.1	1.8 ± 0.1	1.24
15	0.2028	865 ± 3	184 ± 2	113.5 ± 4.9	2.8 ± 0.1	1.8 ± 0.1	1.23
16	0.2535	855 ± 4	175 ± 3	87.5 ± 4.7	2.5 ± 0.2	1.8 ± 0.1	1.31
17	0.3043	839 ± 5	158 ± 4	56.8 ± 4.3	2.6 ± 0.2	1.9 ± 0.2	1.42
18	0.3550	846 ± 5	141 ± 5	46.2 ± 4.0	2.4 ± 0.2	1.6 ± 0.2	1.33
19	0.4057	881 ± 6	160 ± 6	43.3 ± 4.1	2.5 ± 0.3	1.6 ± 0.2	1.24

Table 19—Continued

Row	Y-Offset (")	v_r (km s $^{-1}$)	σ_{gas} (km s $^{-1}$)	F(H α /10 $^{-16}$) (erg s $^{-1}$ cm $^{-2}$ Hz $^{-1}$)	$\frac{F(N\text{ II}_{6585})}{F(H\alpha)}$	$\frac{F(S\text{ II}_{total})}{F(H\alpha)}$	R^2
20	0.4564	900 ± 6	143 ± 6	33.0 ± 3.8	3.0 ± 0.4	2.0 ± 0.3	1.34
21	0.5071	913 ± 5	126 ± 5	27.0 ± 3.5	3.2 ± 0.5	2.3 ± 0.4	1.26
Slit 0: X-Offset 0.000"							
1	-0.5071	1148 ± 7	118 ± 7	31.6 ± 3.7	1.4 ± 0.2	1.2 ± 0.2	1.30
2	-0.4564	1156 ± 7	148 ± 7	28.0 ± 3.5	2.3 ± 0.3	1.9 ± 0.3	1.30
3	-0.4057	1202 ± 5	140 ± 5	32.9 ± 3.4	2.4 ± 0.3	1.6 ± 0.2	1.47
4	-0.3550	1224 ± 4	138 ± 4	46.1 ± 3.6	2.1 ± 0.2	1.4 ± 0.1	1.40
5	-0.3043	1238 ± 4	156 ± 3	60.6 ± 3.9	2.3 ± 0.2	1.6 ± 0.1	1.33
6	-0.2535	1269 ± 3	173 ± 3	86.3 ± 4.1	2.3 ± 0.1	1.5 ± 0.1	1.45
7	-0.2028	1322 ± 3	192 ± 2	115.7 ± 4.4	2.6 ± 0.1	1.8 ± 0.1	1.58
8	-0.1521	1376 ± 2	224 ± 2	190.2 ± 5.2	2.7 ± 0.1	1.9 ± 0.1	1.78
9	-0.1014	1420 ± 2	305 ± 2	380.0 ± 8.1	2.6 ± 0.1	1.6 ± 0.0	2.35
10	-0.0507	1383 ± 4	483 ± 3	633.2 ± 20.0	3.2 ± 0.1	1.7 ± 0.1	3.95
11	0.0000	1107 ± 11	883 ± 5	761.1 ± 81.3	4.8 ± 0.5	2.4 ± 0.3	5.07
12	0.0507	751 ± 10	779 ± 5	402.9 ± 60.4	7.3 ± 1.1	3.9 ± 0.6	4.03
13	0.1014	754 ± 4	415 ± 4	377.8 ± 14.0	3.0 ± 0.1	1.9 ± 0.1	2.33
14	0.1521	786 ± 5	319 ± 4	175.4 ± 7.8	2.9 ± 0.1	1.9 ± 0.1	2.12
15	0.2028	869 ± 6	258 ± 5	106.9 ± 6.0	2.4 ± 0.2	1.4 ± 0.1	1.67
16	0.2535	934 ± 5	188 ± 4	74.5 ± 4.9	2.1 ± 0.2	1.2 ± 0.1	1.30
17	0.3043	963 ± 4	141 ± 4	58.2 ± 4.3	1.9 ± 0.2	1.1 ± 0.1	1.36

Table 19—Continued

Row	Y-Offset (")	v_r (km s $^{-1}$)	σ_{gas} (km s $^{-1}$)	F(H α /10 $^{-16}$) (erg s $^{-1}$ cm $^{-2}$ Hz $^{-1}$)	$\frac{F(N\text{ II}_{6585})}{F(H\alpha)}$	$\frac{F(S\text{ II}_{total})}{F(H\alpha)}$	R^2
18	0.3550	979 ± 3	105 ± 3	37.1 ± 3.5	2.4 ± 0.3	1.3 ± 0.2	1.37
19	0.4057	975 ± 4	101 ± 3	40.0 ± 3.6	2.0 ± 0.2	1.0 ± 0.1	1.37
20	0.4564	960 ± 3	94 ± 3	36.8 ± 3.4	2.0 ± 0.2	1.2 ± 0.2	1.28
21	0.5071	958 ± 3	83 ± 3	33.6 ± 3.3	2.0 ± 0.2	1.2 ± 0.2	1.56
Slit 2: X-Offset +0.2"							
1	-0.5071	1266 ± 6	122 ± 5	38.3 ± 3.7	1.6 ± 0.2	1.2 ± 0.2	1.27
2	-0.4564	1261 ± 5	126 ± 5	34.4 ± 3.5	2.1 ± 0.3	1.4 ± 0.2	1.30
3	-0.4057	1249 ± 5	138 ± 5	34.1 ± 3.5	2.7 ± 0.3	1.3 ± 0.2	1.30
4	-0.3550	1256 ± 5	150 ± 4	34.5 ± 3.6	3.3 ± 0.4	2.2 ± 0.3	1.33
5	-0.3043	1251 ± 4	169 ± 4	49.4 ± 3.9	3.1 ± 0.3	2.0 ± 0.2	1.40
6	-0.2535	1276 ± 4	170 ± 4	61.0 ± 4.1	2.8 ± 0.2	1.6 ± 0.1	1.49
7	-0.2028	1266 ± 3	162 ± 3	71.6 ± 4.2	2.5 ± 0.2	1.4 ± 0.1	1.41
8	-0.1521	1239 ± 3	150 ± 3	79.4 ± 4.3	2.3 ± 0.1	1.3 ± 0.1	1.31
9	-0.1014	1208 ± 3	147 ± 3	71.4 ± 4.4	2.2 ± 0.2	1.4 ± 0.1	1.41
10	-0.0507	1159 ± 4	163 ± 3	59.6 ± 4.6	2.7 ± 0.2	1.7 ± 0.2	1.39
11	0.0000	1126 ± 3	140 ± 3	71.3 ± 4.3	2.1 ± 0.1	1.4 ± 0.1	1.42
12	0.0507	1105 ± 3	136 ± 3	63.5 ± 4.1	2.1 ± 0.2	1.5 ± 0.1	1.28
13	0.1014	1086 ± 4	140 ± 4	54.8 ± 4.1	2.2 ± 0.2	1.1 ± 0.1	1.27
14	0.1521	1060 ± 4	118 ± 4	46.0 ± 3.8	2.1 ± 0.2	1.2 ± 0.1	1.32
15	0.2028	1035 ± 4	111 ± 4	36.1 ± 3.7	2.2 ± 0.3	1.4 ± 0.2	1.22

Table 19—Continued

Row	Y-Offset ('')	v_r (km s $^{-1}$)	σ_{gas} (km s $^{-1}$)	F(H α /10 $^{-16}$) (erg s $^{-1}$ cm $^{-2}$ Hz $^{-1}$)	$\frac{F(N\text{ II}_{6585})}{F(H\alpha)}$	$\frac{F(S\text{ II}_{total})}{F(H\alpha)}$	R^2
16	0.2535	1039 ± 4	102 ± 4	41.1 ± 3.7	1.8 ± 0.2	1.1 ± 0.2	1.40
17	0.3043	1006 ± 4	97 ± 4	45.0 ± 4.1	1.5 ± 0.2	0.7 ± 0.1	1.55
18	0.3550	986 ± 4	96 ± 4	34.2 ± 3.9	1.9 ± 0.3	0.9 ± 0.2	1.36
19	0.4057	980 ± 4	90 ± 4	36.8 ± 4.0	1.4 ± 0.2	0.7 ± 0.1	1.27
20	0.4564	983 ± 4	74 ± 3	36.5 ± 3.7	1.2 ± 0.2	0.7 ± 0.1	1.28
21	0.5071	998 ± 5	90 ± 5	30.3 ± 3.7	1.5 ± 0.2	0.8 ± 0.2	1.28

Table 20. NGC 4486: Measured Parameters.

Row	Y-Offset (")	v_r (km s $^{-1}$)	σ_{gas} (km s $^{-1}$)	F(H α /10 $^{-16}$) (erg s $^{-1}$ cm $^{-2}$ Hz $^{-1}$)	$\frac{F(N\text{ II}_{6585})}{F(H\alpha)}$	$\frac{F(S\text{ II}_{total})}{F(H\alpha)}$	R^2
Slit 1: X-Offset -0.2"							
1	-0.5071	1535 ± 14	374 ± 12	113.0 ± 17.5	3.9 ± 0.6	2.4 ± 0.4	1.93
2	-0.4564	1634 ± 12	376 ± 10	252.0 ± 19.7	2.0 ± 0.2	1.4 ± 0.1	2.10
3	-0.4057	1775 ± 5	266 ± 4	353.6 ± 14.4	1.7 ± 0.1	1.3 ± 0.1	2.18
4	-0.3550	1765 ± 4	256 ± 3	352.3 ± 14.1	2.0 ± 0.1	1.4 ± 0.1	1.89
5	-0.3043	1755 ± 5	274 ± 4	332.3 ± 14.4	2.2 ± 0.1	1.5 ± 0.1	1.90
6	-0.2535	1788 ± 3	274 ± 2	477.4 ± 15.6	2.5 ± 0.1	1.6 ± 0.1	2.33
7	-0.2028	1850 ± 2	235 ± 1	794.4 ± 16.2	2.4 ± 0.1	1.5 ± 0.0	2.68
8	-0.1521	1842 ± 1	206 ± 1	1109.7 ± 17.9	2.4 ± 0.0	1.5 ± 0.0	2.81
9	-0.1014	1814 ± 1	191 ± 0	1301.5 ± 18.2	2.3 ± 0.0	1.3 ± 0.0	3.34
10	-0.0507	1789 ± 1	191 ± 1	1101.6 ± 17.5	2.2 ± 0.0	1.2 ± 0.0	3.37
11	0.0000	1720 ± 1	211 ± 1	894.9 ± 17.9	2.0 ± 0.0	1.1 ± 0.0	2.53
12	0.0507	1587 ± 2	251 ± 2	744.3 ± 19.3	1.9 ± 0.1	1.0 ± 0.0	2.89
13	0.1014	1411 ± 3	304 ± 3	611.7 ± 19.7	2.4 ± 0.1	1.3 ± 0.1	2.98
14	0.1521	1287 ± 4	308 ± 3	536.7 ± 18.8	2.6 ± 0.1	1.6 ± 0.1	2.42
15	0.2028	1195 ± 3	259 ± 2	450.5 ± 15.5	2.6 ± 0.1	1.7 ± 0.1	1.83
16	0.2535	1115 ± 2	197 ± 2	423.7 ± 12.7	2.4 ± 0.1	1.6 ± 0.1	2.20
17	0.3043	1106 ± 2	180 ± 2	311.2 ± 11.1	2.7 ± 0.1	1.8 ± 0.1	1.84
18	0.3550	1120 ± 2	171 ± 2	257.4 ± 10.6	2.5 ± 0.1	1.6 ± 0.1	1.69
19	0.4057	1115 ± 3	149 ± 2	193.4 ± 9.6	2.3 ± 0.1	1.6 ± 0.1	1.87

Table 20—Continued

Row	Y-Offset (")	v_r (km s $^{-1}$)	σ_{gas} (km s $^{-1}$)	F(H α /10 $^{-16}$) (erg s $^{-1}$ cm $^{-2}$ Hz $^{-1}$)	$\frac{F(N\text{ II}_{6585})}{F(H\alpha)}$	$\frac{F(S\text{ II}_{total})}{F(H\alpha)}$	R^2
20	0.4564	1115 ± 3	145 ± 3	139.1 ± 8.8	2.4 ± 0.2	1.8 ± 0.1	1.81
21	0.5071	1112 ± 5	166 ± 5	93.9 ± 8.8	3.2 ± 0.3	1.9 ± 0.2	1.84
Slit 0: X-Offset 0.0"							
1	-0.5071	1451 ± 7	212 ± 6	189.2 ± 14.2	1.8 ± 0.2	1.3 ± 0.1	1.64
2	-0.4564	1469 ± 4	191 ± 4	200.7 ± 13.1	2.4 ± 0.2	1.8 ± 0.1	1.72
3	-0.4057	1497 ± 3	197 ± 2	406.8 ± 15.6	2.1 ± 0.1	1.5 ± 0.1	2.01
4	-0.3550	1521 ± 2	201 ± 2	582.5 ± 17.4	1.9 ± 0.1	1.3 ± 0.0	1.97
5	-0.3043	1532 ± 2	205 ± 2	655.5 ± 17.7	2.1 ± 0.1	1.3 ± 0.0	2.11
6	-0.2535	1526 ± 2	217 ± 1	802.6 ± 19.7	2.1 ± 0.1	1.2 ± 0.0	2.53
7	-0.2028	1548 ± 2	253 ± 2	883.2 ± 22.4	2.2 ± 0.1	1.2 ± 0.0	2.63
8	-0.1521	1525 ± 3	301 ± 2	1378.4 ± 30.7	2.1 ± 0.1	1.0 ± 0.0	3.91
9	-0.1014	1378 ± 3	422 ± 3	2160.2 ± 48.2	2.2 ± 0.1	1.1 ± 0.0	3.38
10	-0.0507	1128 ± 7	681 ± 5	1781.4 ± 108.3	4.3 ± 0.3	1.5 ± 0.1	3.29
11	0.0000	1109 ± 6	612 ± 6	3500.2 ± 102.1	1.8 ± 0.1	0.8 ± 0.0	7.08
12	0.0507	1142 ± 18	920 ± 10	4026.6 ± 258.4	1.2 ± 0.1	0.4 ± 0.0	7.24
13	0.1014	940 ± 8	628 ± 7	1372.2 ± 58.2	2.3 ± 0.1	0.7 ± 0.0	3.91
14	0.1521	948 ± 6	395 ± 5	697.2 ± 26.5	2.5 ± 0.1	1.2 ± 0.1	1.98
15	0.2028	1003 ± 4	277 ± 3	558.2 ± 17.6	2.6 ± 0.1	1.6 ± 0.1	2.13
16	0.2535	1020 ± 2	218 ± 2	622.5 ± 15.2	2.3 ± 0.1	1.5 ± 0.0	2.13
17	0.3043	1007 ± 2	206 ± 2	536.8 ± 13.7	2.3 ± 0.1	1.5 ± 0.0	2.07

Table 20—Continued

Row	Y-Offset (")	v_r (km s $^{-1}$)	σ_{gas} (km s $^{-1}$)	F(H α /10 $^{-16}$) (erg s $^{-1}$ cm $^{-2}$ Hz $^{-1}$)	$\frac{F(N\text{ II}_{6585})}{F(H\alpha)}$	$\frac{F(S\text{ II}_{total})}{F(H\alpha)}$	R^2
18	0.3550	1000 ± 3	193 ± 2	364.7 ± 11.9	2.3 ± 0.1	1.5 ± 0.1	1.95
19	0.4057	1018 ± 4	190 ± 3	266.5 ± 11.5	2.3 ± 0.1	1.4 ± 0.1	1.70
20	0.4564	1047 ± 3	183 ± 3	258.4 ± 11.1	2.2 ± 0.1	1.3 ± 0.1	1.66
21	0.5071	1073 ± 3	156 ± 3	207.0 ± 10.4	2.4 ± 0.1	1.5 ± 0.1	1.47
Slit 2: X-Offset +0.2"							
1	-0.5071	1083 ± 10	225 ± 8	143.0 ± 12.0	1.7 ± 0.2	1.2 ± 0.1	1.84
2	-0.4564	1088 ± 9	236 ± 7	132.8 ± 12.0	2.3 ± 0.2	1.4 ± 0.2	1.90
3	-0.4057	1089 ± 8	234 ± 6	158.2 ± 12.2	2.1 ± 0.2	1.5 ± 0.1	1.75
4	-0.3550	1053 ± 8	254 ± 7	152.5 ± 12.1	2.4 ± 0.2	1.7 ± 0.2	1.82
5	-0.3043	1019 ± 9	275 ± 8	165.4 ± 12.9	2.5 ± 0.2	1.6 ± 0.2	2.15
6	-0.2535	1008 ± 11	309 ± 9	197.4 ± 15.1	2.4 ± 0.2	1.5 ± 0.2	2.03
7	-0.2028	1026 ± 12	350 ± 10	209.9 ± 17.3	2.5 ± 0.2	1.7 ± 0.2	1.85
8	-0.1521	1029 ± 12	367 ± 10	216.5 ± 18.4	2.8 ± 0.3	1.7 ± 0.2	2.05
9	-0.1014	1038 ± 11	368 ± 9	261.9 ± 19.6	2.5 ± 0.2	1.7 ± 0.2	2.39
10	-0.0507	1038 ± 10	380 ± 8	344.8 ± 21.0	2.3 ± 0.2	1.5 ± 0.1	2.10
11	0.0000	992 ± 10	407 ± 8	364.2 ± 22.6	2.5 ± 0.2	1.6 ± 0.1	2.25
12	0.0507	922 ± 9	395 ± 8	404.9 ± 21.9	2.5 ± 0.2	1.6 ± 0.1	2.23
13	0.1014	869 ± 5	329 ± 5	434.7 ± 18.0	2.8 ± 0.1	1.6 ± 0.1	2.39
14	0.1521	852 ± 4	286 ± 3	499.4 ± 16.4	2.6 ± 0.1	1.4 ± 0.1	2.26
15	0.2028	843 ± 3	239 ± 2	555.4 ± 14.7	2.3 ± 0.1	1.3 ± 0.0	2.16

Table 20—Continued

Row	Y-Offset (")	v_r (km s $^{-1}$)	σ_{gas} (km s $^{-1}$)	F(H α /10 $^{-16}$) (erg s $^{-1}$ cm $^{-2}$ Hz $^{-1}$)	$\frac{F(N\text{ II}_{6585})}{F(H\alpha)}$	$\frac{F(S\text{ II}_{total})}{F(H\alpha)}$	R^2
16	0.2535	864 ± 3	239 ± 2	520.7 ± 14.1	2.1 ± 0.1	1.3 ± 0.0	2.23
17	0.3043	890 ± 3	231 ± 2	483.9 ± 13.5	2.1 ± 0.1	1.4 ± 0.1	2.22
18	0.3550	893 ± 3	213 ± 2	440.6 ± 12.6	2.1 ± 0.1	1.3 ± 0.1	1.87
19	0.4057	880 ± 3	199 ± 2	364.4 ± 11.5	2.3 ± 0.1	1.4 ± 0.1	1.97
20	0.4564	907 ± 3	199 ± 2	322.5 ± 11.1	2.1 ± 0.1	1.4 ± 0.1	1.79
21	0.5071	940 ± 4	203 ± 3	296.1 ± 11.0	2.2 ± 0.1	1.5 ± 0.1	1.79

Table 21. NGC 5127: Measured Parameters.

Row	Y-Offset (")	v_r (km s $^{-1}$)	σ_{gas} (km s $^{-1}$)	F(H α /10 $^{-16}$) (erg s $^{-1}$ cm $^{-2}$ Hz $^{-1}$)	$\frac{F(N\text{ II}_{6585})}{F(H\alpha)}$	$\frac{F(S\text{ II}_{total})}{F(H\alpha)}$	R^2
Slit 1: X-Offset -0.2"							
5	-0.6085	4931 ± 17	52 ± 17	4.4 ± 2.3	0.4 ± 0.5	1.3 ± 0.9	3.61
8	-0.3043	4851 ± 10	125 ± 10	11.4 ± 2.8	2.5 ± 0.7	2.7 ± 0.7	3.72
9	-0.2028	4873 ± 9	91 ± 9	5.4 ± 2.2	4.3 ± 1.9	3.5 ± 1.5	3.01
10	-0.1014	4799 ± 8	61 ± 8	6.7 ± 2.1	1.5 ± 0.6	1.8 ± 0.7	3.31
11	0.0000	4919 ± 22	125 ± 22	7.6 ± 2.9	1.8 ± 0.8	1.2 ± 0.6	2.99
12	0.1014	4711 ± 27	161 ± 26	11.1 ± 3.5	1.4 ± 0.6	1.0 ± 0.4	3.59
13	0.2028	4705 ± 10	68 ± 10	9.6 ± 2.5	0.6 ± 0.3	1.4 ± 0.5	3.65
14	0.3043	4663 ± 36	219 ± 31	14.0 ± 4.1	1.0 ± 0.4	1.3 ± 0.5	3.24
17	0.6085	4685 ± 12	75 ± 13	5.9 ± 2.3	2.2 ± 1.0	1.2 ± 0.6	3.17
20	0.9128	4305 ± 12	61 ± 11	8.0 ± 2.4	0.7 ± 0.3	0.7 ± 0.3	3.25
21	1.0142	4360 ± 9	67 ± 9	18.7 ± 4.2	0.0 ± 0.1	0.4 ± 0.1	3.50
Slit 0: X-Offset 0.0"							
4	-0.7099	5010 ± 29	97 ± 29	9.7 ± 4.8	1.3 ± 0.8	0.4 ± 0.4	2.02
7	-0.4057	4879 ± 13	174 ± 12	24.8 ± 5.3	2.9 ± 0.7	2.1 ± 0.5	2.07
8	-0.3043	4902 ± 5	157 ± 5	46.6 ± 5.7	4.3 ± 0.6	2.2 ± 0.3	2.01
9	-0.2028	4861 ± 10	173 ± 8	33.1 ± 5.7	3.5 ± 0.7	2.3 ± 0.5	2.15
10	-0.1014	4810 ± 9	95 ± 9	14.4 ± 4.2	3.0 ± 1.0	2.1 ± 0.7	1.96

Table 21—Continued

Row	Y-Offset ('')	v_r (km s $^{-1}$)	σ_{gas} (km s $^{-1}$)	F(H α /10 $^{-16}$) (erg s $^{-1}$ cm $^{-2}$ Hz $^{-1}$)	$\frac{F(\text{N II}_{6585})}{F(\text{H}\alpha)}$	$\frac{F(\text{S II}_{total})}{F(\text{H}\alpha)}$	R^2
11	0.0000	4769 ± 8	52 ± 8	10.7 ± 3.5	1.9 ± 0.8	1.1 ± 0.5	1.97
12	0.1014	4747 ± 6	36 ± 7	13.2 ± 4.0	1.0 ± 0.4	0.5 ± 0.3	1.99
13	0.2028	4799 ± 17	83 ± 16	11.6 ± 4.5	0.2 ± 0.3	1.4 ± 0.7	1.92
18	0.7099	4606 ± 34	162 ± 33	8.5 ± 4.6	2.9 ± 1.8	1.1 ± 0.9	1.94
21	1.0142	4422 ± 45	166 ± 41	8.0 ± 4.8	1.8 ± 1.3	1.7 ± 1.2	2.29
Slit 2: X-Offset +0.2''							
1	-1.0142	4826 ± 20	19 ± 9	5.3 ± 2.8	0.0 ± 0.2	0.2 ± 0.2	2.64
4	-0.7099	4984 ± 9	56 ± 9	4.9 ± 2.1	2.6 ± 1.3	1.7 ± 0.9	2.37
6	-0.5071	4983 ± 9	72 ± 9	6.9 ± 2.5	3.3 ± 1.4	1.0 ± 0.6	2.41
7	-0.4057	4978 ± 10	86 ± 10	12.1 ± 3.1	2.2 ± 0.7	1.0 ± 0.4	2.36
8	-0.3043	4929 ± 10	90 ± 9	15.9 ± 3.5	1.9 ± 0.5	0.7 ± 0.3	2.24
9	-0.2028	4899 ± 10	76 ± 9	10.1 ± 2.9	2.2 ± 0.8	1.5 ± 0.6	1.91
10	-0.1014	4865 ± 11	77 ± 11	7.5 ± 2.6	1.6 ± 0.8	2.9 ± 1.1	2.53
11	0.0000	4924 ± 32	143 ± 30	10.0 ± 4.1	1.7 ± 0.9	0.7 ± 0.5	2.49
12	0.1014	4918 ± 19	119 ± 19	5.3 ± 3.2	4.8 ± 3.1	0.4 ± 0.6	2.52
13	0.2028	4882 ± 15	88 ± 14	4.6 ± 2.8	4.2 ± 2.7	1.9 ± 1.3	2.50
14	0.3043	4861 ± 14	70 ± 13	4.1 ± 2.5	2.2 ± 1.5	2.4 ± 1.6	2.43
18	0.7099	5121 ± 41	132 ± 39	13.3 ± 5.4	0.1 ± 0.2	0.0 ± 0.2	2.47
19	0.8114	4800 ± 14	68 ± 14	3.0 ± 2.2	1.7 ± 1.4	3.6 ± 2.9	2.91

Table 22. NGC 5141: Measured Parameters.

Table 22—Continued

Row	Y-Offset ('')	v_r (km s $^{-1}$)	σ_{gas} (km s $^{-1}$)	F(H α /10 $^{-16}$) (erg s $^{-1}$ cm $^{-2}$ Hz $^{-1}$)	$\frac{F(\text{N II}_{6585})}{F(\text{H}\alpha)}$	$\frac{F(\text{S II}_{total})}{F(\text{H}\alpha)}$	R^2
1	-1.0142	5440 \pm 26	103 \pm 27	6.4 \pm 3.2	2.1 \pm 1.3	0.8 \pm 0.9	2.24
3	-0.8114	5401 \pm 15	94 \pm 15	8.9 \pm 3.1	2.4 \pm 1.0	0.5 \pm 0.6	2.03
5	-0.6085	5408 \pm 14	117 \pm 14	6.6 \pm 3.0	5.5 \pm 2.7	0.6 \pm 0.8	2.20
6	-0.5071	5486 \pm 20	107 \pm 19	12.5 \pm 3.8	1.6 \pm 0.6	0.4 \pm 0.4	2.05
7	-0.4057	5435 \pm 17	148 \pm 16	20.1 \pm 4.3	1.9 \pm 0.5	1.3 \pm 0.4	1.77
8	-0.3043	5384 \pm 13	183 \pm 12	22.8 \pm 4.6	3.4 \pm 0.8	1.6 \pm 0.5	1.80
9	-0.2028	5330 \pm 5	165 \pm 5	73.6 \pm 5.2	2.4 \pm 0.2	1.2 \pm 0.1	1.99
10	-0.1014	5296 \pm 3	186 \pm 2	191.1 \pm 6.8	2.6 \pm 0.1	1.1 \pm 0.1	2.53
11	0.0000	5228 \pm 3	148 \pm 3	140.1 \pm 6.4	2.4 \pm 0.1	0.9 \pm 0.1	2.39
12	0.1014	5189 \pm 3	106 \pm 3	56.4 \pm 4.8	3.3 \pm 0.3	0.8 \pm 0.1	1.71
13	0.2028	5134 \pm 7	121 \pm 7	30.9 \pm 4.3	2.9 \pm 0.5	0.6 \pm 0.2	1.65
14	0.3043	5088 \pm 17	132 \pm 16	28.2 \pm 5.5	1.0 \pm 0.3	0.7 \pm 0.3	1.84
15	0.4057	5103 \pm 13	112 \pm 13	23.5 \pm 4.5	1.2 \pm 0.3	0.5 \pm 0.3	1.81
16	0.5071	4978 \pm 50	263 \pm 39	22.4 \pm 6.3	1.4 \pm 0.5	1.0 \pm 0.5	2.19
17	0.6085	5344 \pm 51	256 \pm 41	14.0 \pm 5.6	2.3 \pm 1.0	1.2 \pm 0.8	1.84
18	0.7099	5336 \pm 36	213 \pm 32	9.4 \pm 4.8	3.6 \pm 2.0	0.4 \pm 0.7	2.21

Slit 2: X-Offset +0.2''

3	-0.8114	5462 \pm 15	62 \pm 15	6.3 \pm 2.6	1.6 \pm 0.8	0.3 \pm 0.6	2.46
4	-0.7099	5523 \pm 17	95 \pm 17	15.0 \pm 4.0	0.8 \pm 0.3	0.2 \pm 0.3	2.44
6	-0.5071	5326 \pm 22	136 \pm 21	4.5 \pm 3.1	6.8 \pm 4.9	1.1 \pm 1.4	1.85

Table 22—Continued

Row	Y-Offset (")	v_r (km s $^{-1}$)	σ_{gas} (km s $^{-1}$)	F(H α /10 $^{-16}$) (erg s $^{-1}$ cm $^{-2}$ Hz $^{-1}$)	$\frac{F(N\text{ II}_{6585})}{F(H\alpha)}$	$\frac{F(S\text{ II}_{total})}{F(H\alpha)}$	R^2
7	-0.4057	5389 ± 16	112 ± 16	9.2 ± 3.2	3.0 ± 1.2	1.7 ± 0.9	2.04
8	-0.3043	5334 ± 15	100 ± 16	16.0 ± 4.0	1.1 ± 0.4	0.7 ± 0.4	2.22
9	-0.2028	5312 ± 7	115 ± 7	35.9 ± 4.1	1.8 ± 0.3	0.7 ± 0.2	1.81
10	-0.1014	5252 ± 4	122 ± 4	52.1 ± 4.1	2.5 ± 0.2	1.2 ± 0.2	2.06
11	0.0000	5215 ± 5	128 ± 5	53.9 ± 4.6	2.0 ± 0.2	0.8 ± 0.1	2.07
12	0.1014	5162 ± 6	112 ± 6	29.2 ± 3.8	2.5 ± 0.4	0.8 ± 0.2	1.98
13	0.2028	5110 ± 9	95 ± 9	14.2 ± 3.0	2.3 ± 0.6	0.8 ± 0.4	1.72
14	0.3043	5032 ± 14	141 ± 13	22.5 ± 4.0	1.6 ± 0.4	0.7 ± 0.3	2.47
15	0.4057	5062 ± 9	89 ± 8	18.1 ± 3.2	1.6 ± 0.4	0.6 ± 0.2	2.36
16	0.5071	5023 ± 19	113 ± 19	13.7 ± 3.7	1.0 ± 0.4	1.0 ± 0.5	2.15
19	0.8114	4973 ± 8	45 ± 8	9.2 ± 2.5	0.8 ± 0.3	0.1 ± 0.3	2.24
21	1.0142	5510 ± 15	42 ± 15	5.5 ± 2.8	0.1 ± 0.3	0.3 ± 0.4	2.74

Table 23. NGC 5490: Measured Parameters.

Row	Y-Offset (")	v_r (km s $^{-1}$)	σ_{gas} (km s $^{-1}$)	F(H α /10 $^{-16}$) (erg s $^{-1}$ cm $^{-2}$ Hz $^{-1}$)	$\frac{F(\text{N II}_{6585})}{F(\text{H}\alpha)}$	$\frac{F(\text{S II}_{total})}{F(\text{H}\alpha)}$	R^2
Slit 1: X-Offset -0.2"							
3	-0.8114	5164 ± 33	76 ± 33	5.8 ± 3.5	0.5 ± 0.5	0.3 ± 0.6	2.42
5	-0.6085	5104 ± 7	33 ± 10	9.8 ± 4.1	0.1 ± 0.2	0.6 ± 0.4	2.05
10	-0.1014	5008 ± 16	162 ± 15	16.1 ± 4.4	3.4 ± 1.0	0.8 ± 0.5	2.02
11	0.0000	4999 ± 10	205 ± 9	41.3 ± 5.4	3.3 ± 0.5	0.8 ± 0.2	2.29
12	0.1014	5154 ± 11	261 ± 9	79.9 ± 7.0	2.6 ± 0.3	1.0 ± 0.2	2.29
13	0.2028	5220 ± 9	160 ± 8	29.9 ± 4.4	3.6 ± 0.6	1.5 ± 0.3	1.94
14	0.3043	5204 ± 18	145 ± 18	24.3 ± 5.3	1.3 ± 0.4	0.8 ± 0.3	2.00
16	0.5071	5213 ± 17	63 ± 17	7.9 ± 3.3	1.0 ± 0.6	0.5 ± 0.5	2.07
19	0.8114	5154 ± 17	77 ± 16	11.0 ± 3.4	0.9 ± 0.4	0.2 ± 0.3	2.45
20	0.9128	5002 ± 48	192 ± 39	7.4 ± 3.6	2.4 ± 1.4	1.0 ± 0.9	2.51
Slit 0: X-Offset 0.0"							
2	-0.9128	5214 ± 10	34 ± 9	7.0 ± 3.6	0.0 ± 0.2	1.0 ± 0.7	2.21
3	-0.8114	5073 ± 8	39 ± 8	11.4 ± 3.4	0.1 ± 0.2	0.2 ± 0.2	2.37
6	-0.5071	5317 ± 9	38 ± 9	10.6 ± 3.6	0.2 ± 0.2	0.5 ± 0.4	2.20
7	-0.4057	5537 ± 28	115 ± 28	22.9 ± 8.2	0.3 ± 0.2	0.2 ± 0.3	1.79
10	-0.1014	4701 ± 11	280 ± 9	74.4 ± 7.4	3.4 ± 0.4	1.3 ± 0.2	2.24
13	0.2028	5058 ± 16	199 ± 14	40.2 ± 6.6	2.3 ± 0.5	0.7 ± 0.3	2.18

Table 23—Continued

Row	Y-Offset (")	v_r (km s $^{-1}$)	σ_{gas} (km s $^{-1}$)	F(H α /10 $^{-16}$) (erg s $^{-1}$ cm $^{-2}$ Hz $^{-1}$)	$\frac{F(N\text{ II}_{6585})}{F(H\alpha)}$	$\frac{F(S\text{ II}_{total})}{F(H\alpha)}$	R^2
18	0.7099	5491 ± 26	60 ± 25	7.4 ± 4.3	0.2 ± 0.4	0.2 ± 0.5	1.93
21	1.0142	5350 ± 37	131 ± 36	7.7 ± 3.7	1.7 ± 1.1	0.3 ± 0.7	2.43
Slit 2: X-Offset +0.2"							
1	-1.0142	5222 ± 13	41 ± 13	6.1 ± 2.7	0.1 ± 0.2	0.1 ± 0.4	2.81
4	-0.7099	5506 ± 8	30 ± 7	-3.1 ± 1.7	1.1 ± 0.8	3.0 ± 2.0	2.38
13	0.2028	5083 ± 6	77 ± 6	15.3 ± 3.0	3.0 ± 0.7	0.4 ± 0.3	1.67
16	0.5071	5228 ± 36	131 ± 36	8.8 ± 4.0	1.5 ± 0.9	0.2 ± 0.6	1.91

Table 24. NGC 7052: Measured Parameters.

Row	Y-Offset (")	v_r (km s $^{-1}$)	σ_{gas} (km s $^{-1}$)	F(H α /10 $^{-16}$) (erg s $^{-1}$ cm $^{-2}$ Hz $^{-1}$)	$\frac{F(N\text{ II}_{6585})}{F(H\alpha)}$	$\frac{F(S\text{ II}_{total})}{F(H\alpha)}$	R^2
Slit 1: X-Offset -0.1"							
2	-0.4564	4310 ± 26	153 ± 23	35.8 ± 10.0	1.9 ± 0.7	0.3 ± 0.3	2.33
5	-0.3043	4466 ± 26	186 ± 24	28.5 ± 9.9	3.3 ± 1.3	0.6 ± 0.5	1.94
6	-0.2535	4527 ± 24	179 ± 22	25.7 ± 9.8	4.0 ± 1.7	0.7 ± 0.5	2.75
7	-0.2028	4461 ± 26	241 ± 22	50.7 ± 12.0	2.9 ± 0.8	1.0 ± 0.4	2.97
8	-0.1521	4481 ± 27	281 ± 21	86.0 ± 15.0	2.3 ± 0.5	1.6 ± 0.4	2.15
9	-0.1014	4487 ± 15	285 ± 12	167.2 ± 17.1	2.4 ± 0.3	1.1 ± 0.2	2.62
10	-0.0507	4463 ± 15	413 ± 14	289.4 ± 29.2	3.0 ± 0.3	1.1 ± 0.2	2.31
11	0.0000	4541 ± 17	456 ± 16	354.7 ± 35.1	2.7 ± 0.3	0.8 ± 0.1	2.94
12	0.0507	4722 ± 24	387 ± 22	148.1 ± 24.7	2.8 ± 0.5	0.9 ± 0.2	2.95
16	0.2535	4173 ± 7	37 ± 6	29.4 ± 7.9	0.4 ± 0.2	0.1 ± 0.2	2.29
18	0.3550	4130 ± 14	59 ± 13	20.7 ± 8.5	0.1 ± 0.3	1.2 ± 0.6	3.04
19	0.4057	4210 ± 15	54 ± 15	20.2 ± 7.7	0.0 ± 0.2	0.5 ± 0.5	2.56
Slit 0: X-Offset 0.0"							
1	-0.5071	4434 ± 8	66 ± 7	87.2 ± 15.5	0.5 ± 0.1	0.4 ± 0.2	1.76
4	-0.3550	4606 ± 21	130 ± 20	37.3 ± 13.6	1.6 ± 0.7	1.8 ± 0.8	1.65
7	-0.2028	4511 ± 22	175 ± 19	59.6 ± 15.7	2.0 ± 0.6	1.6 ± 0.5	2.02
8	-0.1521	4558 ± 19	232 ± 18	48.1 ± 17.2	5.6 ± 2.1	1.5 ± 0.7	1.46

Table 24—Continued

Row	Y-Offset (")	v_r (km s $^{-1}$)	σ_{gas} (km s $^{-1}$)	F(H α /10 $^{-16}$) (erg s $^{-1}$ cm $^{-2}$ Hz $^{-1}$)	$\frac{F(N\text{ II}_{6585})}{F(H\alpha)}$	$\frac{F(S\text{ II}_{total})}{F(H\alpha)}$	R^2
9	-0.1014	4665 ± 14	265 ± 13	110.1 ± 20.7	4.1 ± 0.8	2.3 ± 0.5	1.54
10	-0.0507	4677 ± 10	268 ± 8	244.8 ± 24.5	3.1 ± 0.3	1.3 ± 0.2	2.09
11	0.0000	4772 ± 11	303 ± 9	285.5 ± 29.5	3.1 ± 0.4	0.5 ± 0.1	1.97
12	0.0507	4832 ± 17	346 ± 16	153.1 ± 28.8	4.1 ± 0.8	1.6 ± 0.4	1.91
14	0.1521	3887 ± 25	65 ± 24	21.6 ± 11.3	0.4 ± 0.4	0.4 ± 0.5	1.64
Slit 2: X-Offset +0.1"							
1	-0.5071	4468 ± 9	84 ± 9	87.2 ± 14.6	0.5 ± 0.1	0.0 ± 0.1	1.91
2	-0.4564	4479 ± 15	99 ± 15	62.3 ± 13.8	0.4 ± 0.2	0.5 ± 0.2	1.73
3	-0.4057	4561 ± 13	75 ± 13	47.9 ± 12.4	0.7 ± 0.3	0.3 ± 0.2	1.82
4	-0.3550	4572 ± 18	114 ± 17	51.7 ± 13.3	1.3 ± 0.4	0.3 ± 0.2	2.24
5	-0.3043	4576 ± 20	105 ± 19	53.3 ± 14.5	0.6 ± 0.3	0.4 ± 0.2	1.99
6	-0.2535	4582 ± 13	79 ± 13	41.2 ± 10.9	0.9 ± 0.4	0.7 ± 0.3	1.82
7	-0.2028	4536 ± 21	127 ± 21	71.6 ± 16.4	0.2 ± 0.2	0.1 ± 0.2	1.87
8	-0.1521	4641 ± 9	69 ± 9	55.7 ± 11.1	1.0 ± 0.3	0.2 ± 0.2	2.06
9	-0.1014	4667 ± 11	126 ± 11	73.4 ± 12.1	1.8 ± 0.4	0.8 ± 0.2	1.91
10	-0.0507	4670 ± 7	109 ± 7	68.4 ± 10.4	2.3 ± 0.4	1.6 ± 0.3	1.73
11	0.0000	4678 ± 9	137 ± 9	65.2 ± 11.1	2.6 ± 0.5	2.1 ± 0.4	2.11
13	0.1014	4726 ± 13	87 ± 12	14.5 ± 7.5	5.8 ± 3.2	0.9 ± 0.8	1.62
14	0.1521	4759 ± 33	125 ± 33	32.5 ± 13.3	1.1 ± 0.6	0.2 ± 0.3	1.50
16	0.2535	4738 ± 32	132 ± 32	20.8 ± 10.5	1.7 ± 1.1	1.8 ± 1.2	2.30

Table 24—Continued

Row	Y-Offset (")	v_r (km s $^{-1}$)	σ_{gas} (km s $^{-1}$)	F(H α /10 $^{-16}$) (erg s $^{-1}$ cm $^{-2}$ Hz $^{-1}$)	$\frac{F(\text{N II}_{6585})}{F(\text{H}\alpha)}$	$\frac{F(\text{S II}_{total})}{F(\text{H}\alpha)}$	R^2
20	0.4564	3941 ± 15	73 ± 15	11.0 ± 5.9	2.9 ± 1.8	2.6 ± 1.6	1.96

Table 25. UGC 12064: Measured Parameters.

Row	Y-Offset (")	v_r (km s $^{-1}$)	σ_{gas} (km s $^{-1}$)	F(H α /10 $^{-16}$) (erg s $^{-1}$ cm $^{-2}$ Hz $^{-1}$)	$\frac{F(N\text{ II}_{6585})}{F(H\alpha)}$	$\frac{F(S\text{ II}_{total})}{F(H\alpha)}$	R^2
Slit 1: X-Offset -0.1"							
2	-0.4564	4876 ± 17	136 ± 17	39.5 ± 10.9	1.8 ± 0.6	1.3 ± 0.5	2.29
3	-0.4057	4971 ± 18	107 ± 18	47.6 ± 11.6	0.4 ± 0.2	0.7 ± 0.3	1.88
4	-0.3550	4962 ± 19	73 ± 19	29.8 ± 10.6	0.1 ± 0.2	0.2 ± 0.3	2.06
5	-0.3043	4880 ± 25	127 ± 25	37.2 ± 11.3	1.0 ± 0.4	0.1 ± 0.3	2.24
6	-0.2535	4868 ± 18	134 ± 16	44.1 ± 10.1	1.7 ± 0.5	0.0 ± 0.3	2.11
7	-0.2028	4940 ± 13	47 ± 12	17.8 ± 7.1	0.5 ± 0.4	0.9 ± 0.6	1.77
8	-0.1521	4957 ± 8	46 ± 8	32.3 ± 8.5	0.4 ± 0.2	0.7 ± 0.3	2.44
9	-0.1014	5015 ± 21	191 ± 18	69.0 ± 13.2	1.6 ± 0.4	0.7 ± 0.3	2.36
10	-0.0507	5085 ± 22	259 ± 20	37.9 ± 13.4	5.4 ± 2.0	2.4 ± 1.0	2.13
11	0.0000	5141 ± 21	248 ± 15	87.6 ± 14.6	2.6 ± 0.5	0.9 ± 0.3	1.81
12	0.0507	5231 ± 26	305 ± 21	93.0 ± 17.7	3.1 ± 0.7	1.2 ± 0.3	1.97
18	0.3550	5121 ± 13	40 ± 12	10.7 ± 5.9	1.4 ± 1.0	0.5 ± 0.7	2.26
Slit 0: X-Offset 0.0"							
2	-0.4564	4783 ± 36	174 ± 34	87.6 ± 24.2	0.3 ± 0.2	0.4 ± 0.3	1.63
3	-0.4057	4795 ± 43	157 ± 41	44.9 ± 18.3	1.1 ± 0.6	0.3 ± 0.4	1.63
5	-0.3043	4963 ± 28	82 ± 29	23.2 ± 14.3	1.2 ± 1.0	0.5 ± 0.7	1.56
6	-0.2535	4951 ± 49	189 ± 44	35.9 ± 17.5	1.8 ± 1.1	1.0 ± 0.8	1.41

Table 25—Continued

Row	Y-Offset (")	v_r (km s $^{-1}$)	σ_{gas} (km s $^{-1}$)	F(H α /10 $^{-16}$) (erg s $^{-1}$ cm $^{-2}$ Hz $^{-1}$)	$\frac{F(N\text{ II}_{6585})}{F(H\alpha)}$	$\frac{F(S\text{ II}_{total})}{F(H\alpha)}$	R^2
8	-0.1521	4846 ± 42	245 ± 36	35.5 ± 17.8	3.8 ± 2.1	2.8 ± 1.6	1.63
10	-0.0507	5070 ± 15	341 ± 14	265.0 ± 31.6	3.3 ± 0.4	1.1 ± 0.2	1.25
11	0.0000	5186 ± 15	496 ± 13	304.5 ± 62.6	7.1 ± 1.5	1.7 ± 0.4	1.67
12	0.0507	5207 ± 14	444 ± 13	446.8 ± 53.5	4.3 ± 0.5	1.0 ± 0.2	2.28
13	0.1014	5187 ± 32	320 ± 27	132.7 ± 28.3	2.7 ± 0.7	0.8 ± 0.3	1.73
19	0.4057	5128 ± 30	97 ± 30	43.7 ± 18.4	0.2 ± 0.2	0.2 ± 0.3	1.68
20	0.4564	5170 ± 35	121 ± 34	36.4 ± 16.2	0.3 ± 0.4	1.3 ± 0.9	1.86
21	0.5071	5086 ± 32	79 ± 32	22.2 ± 15.6	1.1 ± 1.1	0.2 ± 0.6	1.71
Slit 2: X-Offset +0.1"							
1	-0.5071	5016 ± 38	199 ± 34	23.1 ± 10.8	3.0 ± 1.6	0.9 ± 0.8	1.65
2	-0.4564	4863 ± 8	38 ± 7	29.0 ± 8.2	0.6 ± 0.3	0.0 ± 0.2	1.81
3	-0.4057	4881 ± 41	134 ± 42	14.8 ± 9.4	2.1 ± 1.6	0.2 ± 0.8	1.72
8	-0.1521	4884 ± 18	160 ± 17	21.5 ± 9.0	4.7 ± 2.1	3.2 ± 1.5	1.73
9	-0.1014	4914 ± 19	237 ± 17	47.7 ± 12.1	4.1 ± 1.1	1.8 ± 0.6	1.89
10	-0.0507	4926 ± 15	257 ± 12	96.8 ± 14.1	3.3 ± 0.5	1.1 ± 0.3	1.88
11	0.0000	4939 ± 16	304 ± 14	127.4 ± 17.4	3.3 ± 0.5	1.1 ± 0.2	1.72
14	0.1521	5081 ± 45	199 ± 38	38.5 ± 13.1	1.3 ± 0.6	0.6 ± 0.4	2.36
15	0.2028	5088 ± 23	101 ± 22	41.0 ± 12.5	0.1 ± 0.2	0.5 ± 0.3	2.03
16	0.2535	5197 ± 33	97 ± 33	11.2 ± 7.7	2.1 ± 1.8	1.2 ± 1.3	1.69
18	0.3550	4867 ± 38	143 ± 37	43.4 ± 15.4	0.1 ± 0.2	0.3 ± 0.3	1.75

Table 25—Continued

Row	Y-Offset ('')	v_r (km s $^{-1}$)	σ_{gas} (km s $^{-1}$)	F(H α /10 $^{-16}$) (erg s $^{-1}$ cm $^{-2}$ Hz $^{-1}$)	$\frac{F(N\text{ II}_{6585})}{F(H\alpha)}$	$\frac{F(S\text{ II}_{total})}{F(H\alpha)}$	R^2

Table 26. NGC 7626: Measured Parameters.

Row	Y-Offset (")	v_r (km s $^{-1}$)	σ_{gas} (km s $^{-1}$)	F(H α /10 $^{-16}$) (erg s $^{-1}$ cm $^{-2}$ Hz $^{-1}$)	$\frac{F(N\text{ II}_{6585})}{F(H\alpha)}$	$\frac{F(S\text{ II}_{total})}{F(H\alpha)}$	R^2
Slit 1: X-Offset -0.2"							
8	-0.3043	3554 ± 30	210 ± 25	17.5 ± 4.1	1.6 ± 0.5	0.5 ± 0.3	2.25
9	-0.2028	3583 ± 22	230 ± 18	22.5 ± 4.2	2.3 ± 0.5	0.4 ± 0.3	2.17
10	-0.1014	3457 ± 13	200 ± 12	34.4 ± 4.1	1.9 ± 0.3	0.9 ± 0.2	2.46
11	0.0000	3378 ± 8	152 ± 8	14.0 ± 3.1	5.1 ± 1.2	1.4 ± 0.5	2.32
12	0.1014	3332 ± 15	185 ± 14	8.6 ± 3.4	6.5 ± 2.6	1.3 ± 0.8	2.51
13	0.2028	3331 ± 18	163 ± 17	20.5 ± 4.0	1.5 ± 0.4	0.4 ± 0.3	2.14
14	0.3043	3295 ± 27	155 ± 27	13.4 ± 4.1	1.3 ± 0.5	0.4 ± 0.4	2.25
16	0.5071	3289 ± 16	63 ± 16	7.9 ± 2.8	0.0 ± 0.2	0.2 ± 0.3	2.89
17	0.6085	3412 ± 36	147 ± 35	9.7 ± 3.5	0.8 ± 0.4	0.1 ± 0.4	2.61
18	0.7099	3572 ± 23	93 ± 23	10.2 ± 3.3	0.1 ± 0.2	0.1 ± 0.3	3.05
19	0.8114	4142 ± 23	170 ± 21	16.7 ± 3.4	1.0 ± 0.3	0.4 ± 0.2	3.42
Slit 0: X-Offset 0.0"							
1	-1.0142	3116 ± 34	156 ± 33	4.8 ± 3.0	3.9 ± 2.7	0.5 ± 1.0	2.74
2	-0.9128	3191 ± 43	197 ± 38	8.1 ± 3.8	2.6 ± 1.4	0.5 ± 0.7	2.33
6	-0.5071	3630 ± 39	184 ± 36	6.2 ± 3.9	4.2 ± 2.9	0.3 ± 1.0	2.16
7	-0.4057	3568 ± 10	104 ± 10	7.1 ± 2.9	5.6 ± 2.4	2.0 ± 1.0	1.83
8	-0.3043	3605 ± 9	153 ± 8	34.7 ± 4.3	2.5 ± 0.4	1.3 ± 0.2	1.96

Table 26—Continued

Row	Y-Offset ('')	v_r (km s $^{-1}$)	σ_{gas} (km s $^{-1}$)	F(H α /10 $^{-16}$) (erg s $^{-1}$ cm $^{-2}$ Hz $^{-1}$)	$\frac{F(\text{N II}_{6585})}{F(\text{H}\alpha)}$	$\frac{F(\text{S II}_{total})}{F(\text{H}\alpha)}$	R^2
9	-0.2028	3607 ± 5	171 ± 5	65.4 ± 4.8	2.9 ± 0.3	1.2 ± 0.1	1.97
10	-0.1014	3552 ± 4	260 ± 3	217.8 ± 7.7	2.3 ± 0.1	1.0 ± 0.1	2.43
11	0.0000	3446 ± 5	349 ± 5	261.0 ± 11.3	3.2 ± 0.2	1.1 ± 0.1	2.64
12	0.1014	3227 ± 4	223 ± 3	136.0 ± 6.2	2.6 ± 0.1	1.0 ± 0.1	2.58
13	0.2028	3216 ± 6	151 ± 6	44.4 ± 4.3	2.7 ± 0.3	0.9 ± 0.2	2.08
14	0.3043	3235 ± 13	157 ± 13	21.7 ± 4.1	2.5 ± 0.6	0.5 ± 0.3	2.23
16	0.5071	3417 ± 24	95 ± 24	12.4 ± 4.4	0.5 ± 0.3	0.4 ± 0.4	2.32
17	0.6085	3470 ± 16	84 ± 16	7.9 ± 2.9	1.8 ± 0.8	0.3 ± 0.5	2.21
21	1.0142	3136 ± 27	118 ± 28	8.9 ± 3.5	1.1 ± 0.6	1.0 ± 0.7	2.29
Slit 2: X-Offset +0.2''							
5	-0.6085	3780 ± 5	29 ± 5	7.0 ± 2.1	0.1 ± 0.2	1.1 ± 0.5	2.06
6	-0.5071	3849 ± 18	69 ± 18	5.6 ± 2.5	0.6 ± 0.5	2.3 ± 1.3	2.84
10	-0.1014	3479 ± 14	181 ± 14	12.0 ± 3.7	5.5 ± 1.8	1.6 ± 0.7	1.97
11	0.0000	3433 ± 6	135 ± 6	33.9 ± 3.7	2.9 ± 0.4	0.8 ± 0.2	2.36
12	0.1014	3405 ± 7	119 ± 7	27.1 ± 3.5	2.4 ± 0.4	0.1 ± 0.2	1.90
15	0.4057	3442 ± 27	185 ± 25	10.7 ± 3.5	2.6 ± 1.0	0.2 ± 0.5	2.42
16	0.5071	3377 ± 10	51 ± 10	6.0 ± 2.1	1.5 ± 0.7	0.3 ± 0.4	2.29
17	0.6085	3391 ± 10	34 ± 11	2.9 ± 1.7	1.3 ± 1.0	1.2 ± 1.1	2.33
18	0.7099	3275 ± 42	163 ± 41	6.9 ± 3.3	1.5 ± 1.0	1.5 ± 1.0	2.19
19	0.8114	3579 ± 15	56 ± 15	3.8 ± 1.9	1.2 ± 0.8	2.2 ± 1.3	2.65

Table 26—Continued

Row	Y-Offset (")	v_r (km s $^{-1}$)	σ_{gas} (km s $^{-1}$)	F(H α /10 $^{-16}$) (erg s $^{-1}$ cm $^{-2}$ Hz $^{-1}$)	$\frac{F(\text{N II}_{6585})}{F(\text{H}\alpha)}$	$\frac{F(\text{S II}_{total})}{F(\text{H}\alpha)}$	R^2
20	0.9128	3518 ± 10	31 ± 10	4.0 ± 1.9	0.3 ± 0.3	1.0 ± 0.7	2.37

Table 27. Effect of making various fit parameters free.

Fit description	$v_{H\alpha}$ (km s $^{-1}$)	$v_{[NII]}$ (km s $^{-1}$)	$\sigma_{H\alpha}$ (km s $^{-1}$)	$\sigma_{[NII]}$ (km s $^{-1}$)	$\frac{F([N II]_{6585})}{F([N II]_{6549})}$	R^2
(1)	(2)	(3)	(4)	(5)	(6)	(7)
initial parameters	4620 ± 4		249 ± 3		3.0	3.21
$v_{H\alpha}$ free	4616 ± 9	4620 ± 3		249 ± 3	3.0	3.22
$\sigma_{H\alpha}$ free		4619 ± 3	228 ± 9	256 ± 4	3.0	3.21
$v_{H\alpha} + \sigma_{H\alpha}$ free	4618 ± 9	4619 ± 4	228 ± 9	256 ± 4	3.0	3.22
[N II] ratio free		4622 ± 3		248 ± 3	2.32 ± 0.09	3.04

Note. — The measurements shown were made using the central spectral row in the central slit observed for NGC 4335. Col. (1): Parameters made free, Initially a set of lines with one velocity and one velocity dispersion was used, with the ratio of the two [N II] lines fixed to 3.0. The two [S II] lines are fixed in velocity and width to the [N II] lines in every case; Col. (2-3): The radial velocities of the H α and [N II] lines; Col. (3-4): The velocity dispersions of the H α and [N II] lines; Col. (5): The ratio of the [N II]₆₅₈₅ and [N II]₆₅₄₉ lines; Col. (6): The reduced χ^2 value of the resulting fit.

Table 28. Presence of a Nuclear Broad Line.

Galaxy (1)	$\Delta \overline{residual} $ (%) (2)	$\frac{R_N^2 - R_A^2}{R_N^2}$ (3)	By eye (4)	Score (5)	Broad Cpt. (6)
NGC 193	9.6	0.19	✓	3	Yes
NGC 315	25.0	0.46	✓	3	Yes
NGC 383	8.7	0.16	○	2	Yes
NGC 541	4.6	0.12	✓	1	No
NGC 741	1.9	0.01	○	0	No
UGC 1841	14.7	0.35	✓	3	Yes
NGC 2329	9.4	0.32	○	2	*
NGC 2892	2.8	0.09	○	0	No
NGC 3801	0.1	0.01	○	0	No
NGC 3862	8.0	0.22	○	2	*
UGC 7115	2.6	0.09	○	0	No
NGC 4261	7.8	0.22	✓	3	Yes
NGC 4335	8.0	0.40	✓	3	Yes
NGC 4374	2.4	0.12	○	0	No
NGC 4486	3.4	0.15	✓	2	Yes
NGC 5127	-1.5	-0.01	○	0	No
NGC 5141	3.7	0.16	✓	2	Yes
NGC 5490	5.2	0.23	✓	3	Yes
NGC 7052	4.9	0.04	✓	1	No
UGC 12064	6.7	0.11	✓	2	Yes
NGC 7626	2.5	0.13	✓	2	Yes

Note. — Col. (1): NGC/UGC Identification; Col. (2): Difference in the mean of the absolute values of the residuals from the fits including and excluding the additional component; Col. (3): Relative change in reduced χ^2 value between fits with the narrow lines alone (N) and with the additional component (A); Col. (4): Could an improvement in the fit be judged by eye?; Col. (5): Additional component ‘score’, one point available from each of columns 2 to 6, see text for criteria; Col. (6) Is an additional broad component useful in the fit based on these results? An asterisk (*) indicates the component appears to represent a non-flat continuum.

Table 29. Fits to the central pixel for each galaxy, including broad lines. Kinematics.

Galaxy	Row	v_r (NL) (km s $^{-1}$)	v_r (BL) (km s $^{-1}$)	σ_{gas} (NL) (km s $^{-1}$)	σ_{gas} (BL) (km s $^{-1}$)	R^2
(1)	(2)	(3)	(4)	(5)	(6)	(7)
NGC 193	11	4417 ± 7	5128 ± 36	277 ± 6	967 ± 21	3.15
NGC 315	11	4830 ± 9	5738 ± 55	406 ± 9	1790 ± 67	2.06
NGC 383	11	5278 ± 54	5568 ± 29	669 ± 39	1367 ± 79	2.25
UGC 1841	11	6409 ± 8	6585 ± 20	436 ± 7	1254 ± 35	3.11
NGC 4261 [†]	11	2056 ± 9	2703 ± 68	366 ± 12	1079 ± 55	1.69
NGC 4335	11	4618 ± 3	4893 ± 37	188 ± 4	1299 ± 51	1.93
NGC 4486	11	1417 ± 14	1408 ± 28	534 ± 12	1479 ± 42	6.01
NGC 5141	11	5229 ± 3	5356 ± 86	121 ± 4	1223 ± 96	2.01
NGC 5490	11	4733 ± 16	5621 ± 61	377 ± 22	1336 ± 56	1.94
UGC 12064	11	5195 ± 16	5417 ± 90	423 ± 19	1321 ± 168	1.49
NGC 7626	11	3432 ± 7	4083 ± 76	287 ± 10	1126 ± 73	2.29

Note. — [†]For NGC 4261 slit 1 (offset -0.1 arcsec) was used; Col. (1): NGC/UGC Number; Col. (2): Central pixel row number referenced from the earlier data tables for each galaxy; Col. (3): The line of sight velocities of the narrow line components; Col. (4): The line of sight velocities of the broad components (where present); Col. (5): The line of sight velocity dispersions of the narrow line components; Col. (6): The line of sight velocity dispersions of the broad components (where present); Col. (7): The reduced χ^2 value of the fit. The parameters were measured by fitting a models with 5 narrow lines, fixed to each other in velocity and velocity dispersion and one free broad component, except as noted above. Errors quoted are the formal errors on the various parameters from the fit.

Table 30. Fits to the central pixel for each galaxy, including broad lines. Fluxes.

Galaxy (1)	$F(H\alpha_{Narrow})$ ($\text{ergs}^{-1}\text{cm}^{-2}\text{Hz}^{-1}$) (2)	$\frac{F([N\text{ II}]_{6585})}{F(H\alpha_{Narrow})}$ (3)	$\frac{F([S\text{ II}]_{total})}{F(H\alpha_{Narrow})}$ (4)	$\frac{F(\text{Broad Line})}{F(H\alpha_{Narrow})}$ (5)	$\frac{F([S\text{ II}]_{6733})}{F([S\text{ II}]_{6718})}$ (6)
NGC 193	1.33 ± 0.23	4.21 ± 0.77	3.86 ± 0.71	7.60 ± 1.46	1.18 ± 0.07
NGC 315	9.28 ± 0.77	4.72 ± 0.42	1.81 ± 0.21	4.40 ± 0.51	1.80 ± 0.14
NGC 383	27.72 ± 3.65	0.33 ± 0.18	0.56 ± 0.63	2.14 ± 0.50	0.11 ± 0.12
UGC 1841	7.71 ± 0.46	2.41 ± 0.16	1.39 ± 0.11	2.57 ± 0.28	1.09 ± 0.06
NGC 4261	4.36 ± 1.53	6.76 ± 2.42	3.37 ± 1.23	7.22 ± 2.93	1.55 ± 0.15
NGC 4335	1.33 ± 0.13	4.46 ± 0.44	2.63 ± 0.32	7.54 ± 0.87	1.04 ± 0.08
NGC 4486	44.96 ± 1.53	0.43 ± 0.04	0.59 ± 0.60	1.37 ± 0.11	0.03 ± 0.03
NGC 5141	0.91 ± 0.07	2.95 ± 0.25	1.38 ± 0.22	3.11 ± 0.45	0.97 ± 0.14
NGC 5490	0.25 ± 0.20	14.34 ± 11.64	9.12 ± 7.56	40.54 ± 32.95	1.94 ± 0.38
UGC 12064	0.48 ± 1.14	30.72 ± 72.97	11.16 ± 26.60	32.31 ± 77.41	0.58 ± 0.12
NGC 7626	1.48 ± 0.24	3.80 ± 0.66	1.98 ± 0.38	4.00 ± 1.01	0.95 ± 0.09

Note. — Col. (1): NGC/UGC Number; Col. (2): $H\alpha$ narrow line flux; Col. (3): Ratio of the broad line flux to the $H\alpha$ narrow line flux; Col. (4) Ratio of the $[N\text{ II}]_{6585}$ narrow line flux to the $H\alpha$ Narrow line flux; Col. (5) Ratio of the total $[S\text{ II}]$ flux to the $H\alpha$ Narrow line flux; Col. (6) Ratio of the $[S\text{ II}]_{6733}$ narrow line to the $[S\text{ II}]_{6718}$ narrow line. The parameters were measured by fitting a models with 5 narrow lines, fixed to each other in velocity and velocity dispersion and one free broad component, except as noted above. Errors quoted are the formal errors on the various parameters from the fit.

Table 31. Kinematic estimators within 100 pc of the nucleus.

Galaxy	$r_{\text{max.}}$ (pc)	$\sigma_{\text{nuc.}}$ (km s $^{-1}$)	$\bar{\sigma}_{100\text{pc}}$ (km s $^{-1}$)	$\Delta_{100\text{pc}}$ (km s $^{-1}$)
	(1)	(2)	(3)	(4)
Rotators				
NGC 315	...	528	290	353
NGC 383	...	924	342	434
NGC 2329	...	302	145	84
UGC 7115	...	497	287	337
NGC 4261	78	459	238	319
NGC 4335	...	249	166	307
M 84	41	883	229	669
NGC 4486	41	612	313	607
NGC 5127	...	157	148	69
NGC 5141	...	149	146	196
NGC 7052	...	303	226	945
UGC 12064	...	497	308	361
NGC 7626	...	350	175	391
Mean		463 ± 254	236 ± 72	390 ± 250
Non-Rotators				
NGC 193	...	437	228	253
NGC 541	...	336	182	266
UGC 1841	...	593	378	16
NGC 2892	...	453	338	118
NGC 3801	...	163	143	113
NGC 3862	...	303	182	130
NGC 5490	...	680	240	358
Mean		381 ± 147	242 ± 95	149 ± 95

Note. — Col. (1): Galaxy ID; Col. (2): Where the radius away from the central pixel used was less than 100 pc the radius is indicated here; Col. (3): The velocity dispersion of the very central spectrum; Col. (4): The mean velocity dispersion within 100 pc of the central position; Col. (5): The difference in mean velocities within 100 pc to either side of the central spectrum. The galaxies are grouped into two classes ‘rotators’ and ‘non-rotators’ judged by eye as discussed in the text, mean values of each parameter are given for each class.

Table 32. Comparison of broad line statistics

Parameter (1)	UGC FR-I sample (2)	Sy/LINERs (3)	Radio Loud (4)
$\langle \sigma_{BL} \rangle$ (km s $^{-1}$)	1295 ± 218	2400 ± 1100	5900 ± 3700
$\langle \sigma_{NL} \rangle$ (km s $^{-1}$)	371 ± 153
$\langle v_{NL} - v_{BL} \rangle$ (km s $^{-1}$)	-435 ± 335	...	-500 ± 1200

Note. — The mean velocity dispersions of broad and narrow lines and offsets of broad and narrow lines for three different galaxy samples: Col.(2) the data presented in this work; Col. (3) A sample of Seyferts and LINERs; Col. (4) A summary of properties of several sample of radio galaxies.

References. — (3) Ho, et al. (1997); (4) Sulentic, et al. (2000)

Table 33. Kinematic parameters measured using various free-parameter sets.

Model ID (1)	Description (2)	v_r (NL)	v_r (BB)	v_r (BC)	σ_{gas} (NL)	σ_{gas} (BB)	σ_{gas} (BC)	R^2 (9)
		(km s ⁻¹) (3)	(km s ⁻¹) (4)	(km s ⁻¹) (5)	(km s ⁻¹) (6)	(km s ⁻¹) (7)	(km s ⁻¹) (8)	
1	Narrow lines only	4620	249	3.21
2	Model 1 + Extra Broad Component	4618	...	4893	188	...	1299	1.93
3	Model 2 + Constrained Broad Bases (i)	4616	= 4616	4767	139	354	1565	1.73
4	Model 2 + Constrained Broad Bases (ii)	4595	4724	4680	139	319	1417	1.60
5	Model 2 + Unconstrained Broad Bases	4616	= 4616	4764	128	319	1389	1.68

Note. — Col. (1) Model ID (see text); Col. (2): Brief description of the fit; Cols. (3-5): The radial velocities of the narrow line (NL), broad base (BB) and broad components (BC) respectively; Cols. (6-8): The velocity dispersions of the narrow line (NL), broad base (BB) and broad components (BC) respectively. Fits were performed on the central row of the central slit of the observations of NGC 4335; Col. (9): The reduced χ^2 value of the fit.